DEVELOPMENT OF TEST STRUCTURES AND METHODS FOR CHARACTERIZATION OF MEMS MATERIALS

A THESIS SUBMITTED TO
THE GRADUATE SCHOOL OF NATURAL AND APPLIED SCIENCES
OF
MIDDLE EAST TECHNICAL UNIVERSITY

BY

ENDER YILDIRIM

IN PARTIAL FULFILLMENT OF THE REQUIREMENTS
FOR
THE DEGREE OF MASTER OF SCIENCE
IN
MECHANICAL ENGINEERING

SEPTEMBER 2005

Approval of the Graduate School of Natural and Applied Sciences

_____

Prof. Dr. Canan Özgen
Director

I certify that this thesis satisfies all the requirements as a thesis for the degree of Master of Science.

_____

Prof. Dr. Kemal İder
Head of Department

This is to certify that we have read this thesis and that in our opinion it is fully adequate, in scope and quality, as a thesis for the degree of Master of Science.

Prof. Dr. Tayfun Akın Co-Supervisor	Prof. Dr. M. A. Sahir Arıkan Supervisor

Examining Committee Members

Prof. Dr. Tuna Balkan	(METU,ME)	_____
Prof. Dr. M. A. Sahir Arıkan	(METU,ME)	_____
Prof. Dr. Tayfun Akın	(METU,EE)	_____
Asst. Prof. Dr. İlhan E. Konukseven	(METU,ME)	_____
Asst. Prof. Dr. Haluk Külah	(METU,EE)	_____

I hereby declare that all information in this document has been obtained and presented in accordance with academic rules and ethical conduct. I also declare that, as required by these rules and conduct, I have fully cited and referenced all material and results that are not original to this work.

Name, Last name: Ender Yıldırım

Signature :

ABSTRACT

DEVELOPMENT OF TEST STRUCTURES AND METHODS FOR CHARACTERIZATION OF MEMS MATERIALS

Yıldırım, Ender
M.Sc., Department of Mechanical Engineering
Supervisor: Prof. Dr. M. A. Sahir Arıkan
Co-Supervisor: Prof. Dr. Tayfun Akın

September 2005, 150 pages

This study concerns with the testing methods for mechanical characterization at micron scale. The need for the study arises from the fact that the mechanical properties of materials at micron scale differ compared to their bulk counterparts, depending on the microfabrication method involved. Various test structures are designed according to the criteria specified in this thesis, and tested for this purpose in micron scale. Static and fatigue properties of the materials are aimed to be extracted through the tests. Static test structures are analyzed using finite elements method in order to verify the results.

Test structures were fabricated by deep reactive ion etching of 100 μm thick (111) silicon and electroplating 18 μm nickel layer. Performance of the test structures are evaluated based on the results of tests conducted on the devices made of (111)

silicon. According to the results of the tests conducted on (111) silicon structures, elastic modulus is found to be 141 GPa on average. The elastic modulus of electroplated nickel is found to be 155 GPa on average, using the same test structures. It is observed that while the averages of the test results are acceptable, the deviations are very high. This case is related to fabrication faults in general.

In addition to the tests, a novel computer script utilizing image processing is also developed and used for determination of the deflections in the test structures.

Keywords: Micro Electro Mechanical Systems, Mechanical Characterization, Test Structure

ÖZ

MEMS MALZEMELERİNİN KARAKTERİZASYONU İÇİN TEST YAPILARI VE YÖNTEMLERİNİN GELİŞTİRİLMESİ

Yıldırım, Ender
Yüksek Lisans, Makina Mühendisliği Bölümü
Tez Yönetisi: Prof. Dr. M. A. Sahir Arıkan
Ortak Tez Yöneticisi: Prof. Dr. Tayfun Akın

Eylül 2005, 150 sayfa

Bu çalışma, mikron seviyesindeki mekanik nitelendirme için olan test yöntemleriyle ilgilidir. Bu çalışmaya gereksinim, mikron ölçekli malzemelerin mekanik özelliklerinin büyük boyutlu eşleriyle karşılaştırıldığında, kullanılan mikrofabrikasyon yöntemine göre farklılık göstermesinden kaynaklanmaktadır. Bu amaçla, tezde belirtilen ölçütlere dayanarak mikron seviyesinde çeşitli test yapıları tasarlanmış ve test edilmiştir. Malzemelerin statik ve yorulma özelliklerinin testler yoluyla belirlenmesi amaçlanmıştır. Sonuçları doğrulamak için, statik test yapılarının sonlu eleman yöntemi kullanılarak analizleri yapılmıştır.

Test yapıları, 100 μm kalınlığındaki (111) silisyumun derin reaktif iyon aşındırılması ile ve 18 μm nikel elektrokaplama ile üretilmişlerdir. Test

yapılarının başarımı, (111) silisyumdan yapılan cihazların üzerinde yapılan testlerin sonuçlarına dayanılarak değerlendirilmiştir. (111) silisyum yapıların üzerinde yapılan test sonuçlarına göre, elastik modül ortalama olarak 141 GPa olarak bulunmuştur. Aynı yapılar kullanılarak, elektrokaplanmış nikelin elastik modülü ortalama olarak 155 GPa olarak bulunmuştur. Test sonuçlarının ortalamalarının kabul edilebilir olmasına rağmen, sapmaların çok yüksek olduğu gözlenmiştir. Bu durum, genel olarak fabrikasyon hatalarıyla ilişkilendirilmiştir.

Testlere ek olarak, mikron seviyesinde ölçümleme için görüntü işleme kullanılarak yeni bir bilgisayar betiği geliştirilmiş ve test yapılarındaki eğilmeleri belirlemek için kullanılmıştır.

Anahtar Kelimeler: Mikro Elektro Mekanik Sistemler, Mekanik Karakterizasyon, Test Yapısı

To Ozan and Deniz

ACKNOWLEDGEMENTS

I would like to thank to my thesis supervisors Prof. Dr. M. A. Sahir Arıkan and Prof. Dr. Tayfun Akın, for their patience and sincere attitude throughout the study. I would also thank to Mr. Said Emre Alper for his continuous support on theory and help in fabrication. I have learned a great deal about MEMS from him. I would also thank to Asst. Prof. Dr. Haluk Külah for his advices on thesis organization. I am also thankful to Mr. Kıvanç Azgın for his help on fabrication and post-processing of the devices, also for valuable discussions on mechanical topics. I would also thank to Mr. Yusuf Tanrıkulu for his help in taking the SEM pictures of the devices. I am also thankful to Mr. Orhan Akar for his help in fabrication and measurements on optical profiler. I would also thank to Mr. İlter Önder for his help in statistical evaluation of the test results. I am also thankful to Mr. Cevdet Can Uzer for his support in writing phase of my thesis. Finally I would like to express my respect and affection to my family for their invaluable support throughout my life.

TABLE OF CONTENTS

LIST OF FIGURES

LIST OF TABLES

CHAPTER 1

INTRODUCTION

Growing microsystems technology led to improvement of fabrication techniques and enforced search on materials and their mechanical properties. As required for the design of bulk mechanical structures, the design of micro structures and micro-electro-mechanical devices also requires the knowledge of mechanical properties such as elastic modulus and fatigue characteristics of the materials used. As a result testing techniques are started to be developed for characterization of Micro Electro Mechanical Systems (MEMS) materials.

However testing of micro specimens in order to extract mechanical properties is not as straightforward as the testing of bulk specimens. The reason for that is mainly the difficulty in measurement of both forces and displacements. Since it is hard to measure these quantities, they are related to quantities, such as voltage, that are easier to measure. These relations generally involve complicated mathematical models. As a result, these complicated models make the testing of micro specimen a challenging work.

Moreover there are not standard ways of testing in micron scale, due to wide variety of fabrication methods. Various test devices are fabricated using different methods up to now. The results of tests conducted on these devices are reported. However comparison of these individual test devices is not available. It is aimed to evaluate the performances of various existing and novel test devices by

comparing the results of the tests conducted on them. By this way, it may also be possible to standardize the mechanical testing in micro scale.

Before going further into the study, a rough background is aimed to be provided for the reader. This chapter includes brief information about MEMS, fabrication of MEMS, and mechanical characterization. Section 1.1 explains brief history of MEMS and the application areas of MEMS. Section 1.2 includes the basic fabrication methods for manufacturing MEMS. Section 1.3 overviews the mechanical characterization approaches both in bulk and micro scale. Also, possible error sources in testing of micro specimen are introduced in this section. Additionally, some criteria for qualitatively evaluating different testing methods are set in this section. Finally, Section 1.4 describes the thesis organization.

1.1 History and Application of MEMS

Invention of the transistor in 1948 led to the birth of a new subject, which would grow since early 50's with the invention of junction field-effect transistor (JFET) and the development of integrated circuits (ICs) in late 50's. After then in 1970, the microprocessor is invented. Rapidly growing microelectronics technology necessitated the development of micro sensors and micro actuators. Ongoing development of technology introduced first micromachined accelerometer in Stanford University in 1979. The polysilicon surface micromachining process developed in University of California, Berkeley in 1984, resulted in integrated chips encapsulating sensing, processing and actuation which can be so called a microsystem in the late 80's.

Inevitable development of miniaturization lead to an interdisciplinary field of microelectromechanical systems (MEMS) also called microsystems. While the name MEMS emphasizes the miniaturization, MEMS is also a name for a toolbox, a physical product, and a methodology for production of micro systems [2]. Actually in 1959, when Richard P. Feynman made his famous speech of "There is

plenty of room at the bottom", it was probably the first time that miniaturization is defined as a methodology.

MEMS is utilized in both civil and military applications. As the subject become more common, variations in application increases. Recent civil applications include microfabricated accelerometers for safety means (air bag etc.) in vehicles, micro-pumps in inkjet printers or medicine (drug delivery) (Figure 1.1) and micro pressure sensors in automotive for fuel control. Some of the military applications of MEMS include microfabricated accelerometers and gyroscopes for guidance of munitions and control of navigation, micro flaps for control of turbulence in again munitions guidance, and infrared (IR) detection for night vision. Considering the above mentioned applications of MEMS, it can be concluded that they generally provide smaller functions integrated to a larger scale utility [2]. That is for instance, while a micropump itself affects the turbulence (small function); it is used for guidance of a missile (large utility).

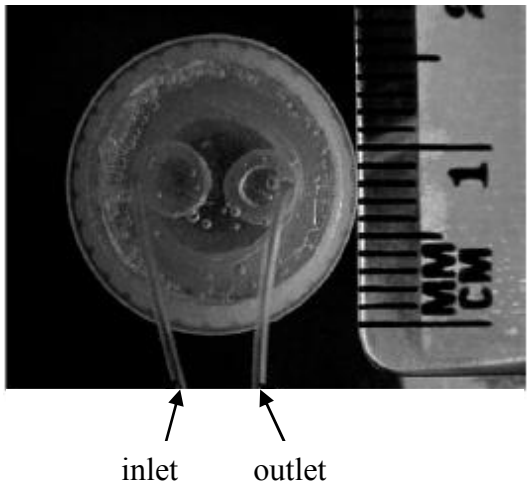

Figure 1. 1: Magnetically actuated micropump [3]

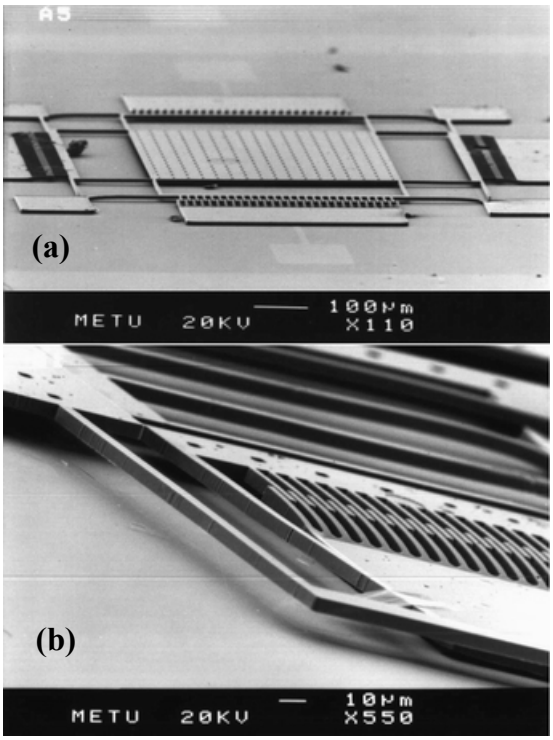

Figure 1. 2: Gyroscope, fabricated in METU

The structures in MEMS generally include overhanging components such as the one shown on Figure 1.2. Production of such structures requires specialized non-traditional techniques. Some of the basic techniques utilized for fabrication of MEMS are explained in the following section.

1.2 Fabrication of MEMS

While fabrication of MEMS is a very detailed subject, this section only gives brief information about basic processes involved. Basic processes utilized in micro fabrication can be grouped under three main titles; deposition, patterning, and etching [2].

1.2.1 Deposition

Deposition includes all techniques of material deposition on substrate, where the structure is built on or which is used for the fabrication of structure itself. The substrate is generally a silicon wafer. Some deposition techniques include

physical vapor deposition, chemical vapor deposition, and epitaxy. In physical vapor deposition, the material to be deposited, basically leaves the source in gas phase and is piled up on target substrate. Transferring the source material into gas phase can be achieved by using mainly two techniques: sputtering and evaporation. In sputtering, the source material is bombarded by a flux of inert gases in a vacuum chamber [2] to generate the source gas. Evaporation requires heating of the source material in order to generate the source gas to be deposited.

Chemical vapor deposition techniques are usually high temperature processes. Principle of chemical vapor deposition is that a chemical reaction between the source atoms to be deposited and the heated substrate is favored in a vacuum chamber. The ambience can be at low pressure or the reaction can be plasma enhanced in chemical vapor deposition. In low pressure chemical vapor deposition (LPCVD), the conformity of deposition is quite satisfactory, since the source material can reach even small gaps in low pressure environment.

Another deposition technique is epitaxy. Epitaxy is used for growing silicon layers on the silicon substrate. In a high temperature environment, silicon atoms are introduced on a silicon wafer. Silicon atoms that land on the substrate form an epitaxial silicon layer that has the same crystalline structure with the substrate.

1.2.2 Patterning

Being another class of microfabrication processes, patterning means the replication of two dimensional patterns on deposited materials. The process used for patterning is essentially photolithography. The pattern is actually the layout of the structures to be fabricated on the wafer. The draft of this layout is prepared using a CAD software and printed on a mask of opaque chromium layer on a glass substrate [2]. Photolithography utilizes an optical sensitive material, namely photoresist, on which the pattern is replicated. This photoresist is spun over the wafer, forming a layer. This layer of photoresist is partially hardened through a heat treatment. After than, the photoresist layer is exposed to UV light through the

mask. Exposed regions are either hardened or remain soluble according to the type of photoresist (negative or positive). Exposed wafer is than developed for removing the soluble regions of photoresist. Remaining photoresist on the substrate wafer is the replica of the pattern. Photolithography, using negative or positive photoresist is illustrated on Figure 1.3.

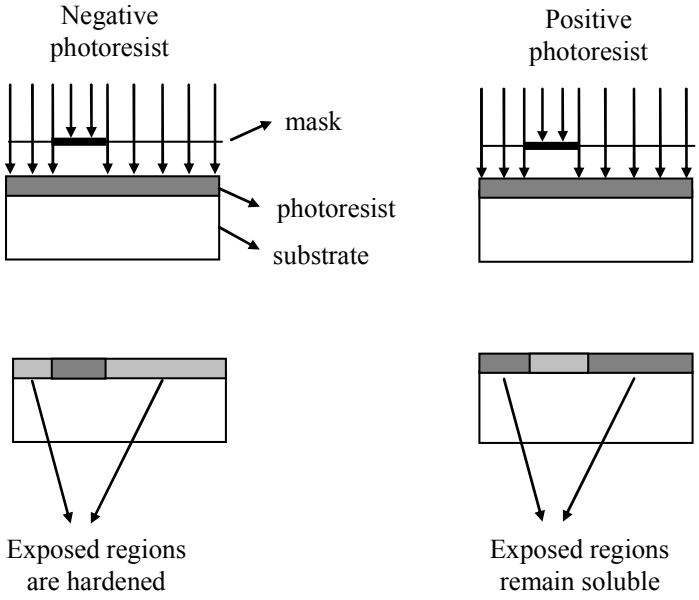

Figure 1. 3: Photolithography using negative or positive photoresist

1.2.3 Etching

As the third class of micro fabrication processes, etching is removal of material through chemical reactions, while generating three dimensional structures. The etchants used may be wet (in form of solutions) or dry (gases in plasma phase). Also etching can be classified according to directional properties. If the etch rate is the same in all crystallographic directions through the substrate, then the process is named to be isotropic etching. However, if the etch rates are different for each crystallographic directions, than the process is called anisotropic etching. Isotropic and anisotropic etching is illustrated in Figure 1.4 below.

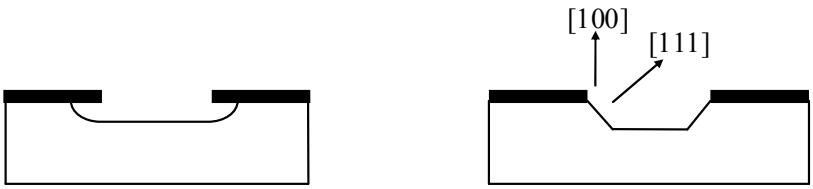

Figure 1. 4: Isotropic and anisotropic etching, [100] and [111] designates different crystallographic directions

Etching is done through a masking layer which should not be affected by the etchant. Therefore the selectivity of the etchant becomes an important property as well as the directional characteristic of the etching. Using proper combination of a masking layer and an anisotropic etchant, the pattern on the masking layer is transferred to the underlying layer. Using an isotropic etchant will result in formation of an undercut in the underlying layer. However this can be made use of in order to form overhanging structures. That is, undercutting the layer or completely removing the layer beneath the mask, leaves an overhanging structure above.

Most of the wet etchants are known to be isotropic [4]. Although isotropic, they are widely used, since they provide fairly good selectivity during etching. That is they preferably etch the structural material. Different from wet etching, dry etching utilizes ionized reactive gases. If more energy is supplied to the source gas, the ions become more energetic, resulting in physical etching in addition to chemical etching. The process is called the reactive ion etching. If the ions are collimated through a vacuum, the etching becomes highly physical. This type of dry etching is named as ion beam etching. While these processes result in quite anisotropic etches, they generally suffer selectivity.

These basic processes are combined to derive methods for fabrication of MEMS products, such as the test devices used in this study. Fabrication details of the test devices are given in Section 3.4.

After giving an overview about the MEMS and their fabrication, an introduction should be provided to the reader about basics of mechanical characterization in detail.

1.3 Mechanical Characterization of MEMS Materials

In general, mechanical testing methods can be classified as direct methods and inverse methods [5]. Direct methods imply direct measurement of forces and strains, thus direct extraction of mechanical properties. Tensile testing of bulk specimens can be given as an example of direct methods. Application of direct methods requires uniform gage sections for precise measurement of dimensions, which can be relatively easy for bulk parts. However this may not be possible for micron scaled structures.

In micron scale it is hard to obtain uniform gage sections and handle the specimen for direct measurements of forces and displacements. In order to account for this, directly measured quantities, such as voltage (depending on the type of actuation), are related to forces through mathematical models. These models are derived specifically for the test device. Mechanical tests that involve this kind of mathematical models are called inverse tests. Hence, mechanical testing in micron scale generally involves inverse methods.

Independent of the type of method employed, metrology errors occur both in inverse methods and direct methods. In addition to metrology errors, insufficiently precise mathematical models used in inverse methods may lead to significant errors. Therefore utilizing inverse methods may result in widely varying results for the same material tested at same conditions. Moreover measurement of

dimensions potentially yields relatively higher errors in micro scale. Testing in micron scale usually involve on-chip test devices, where the specimen and the actuation mechanism are fabricated as a whole. However this hinders the direct measurement of properties such as displacements and forces with reasonable accuracy, since the specimen is at the same order of size with the device. That is the specimen generally does not allow a gripping space or gage sections for direct measurements. Measurement of displacements can be achieved by capacitive reading or by optical means using proper vernier gages. Direct measurement of strain is preferable; however this can not be always available. It is possible to observe the straining, real-time using the infringement of the laser reflected from two reflective lines on the gage section of the specimen [5]. However it is more applicable, in most of the cases, to relate the strain to displacement, since it is easier to read the displacement.

Measurement of the specimen dimensions is another problem in micro scale. Generally, the length of the specimen (or any part of the structure) is relatively large to be measured visually by using optical means. Also the thickness of the structure is usually well defined by the fabrication process. It is the width of the specimen that is difficult to measure. However, it may still be possible to measure the width of the specimen after fracture using scanning electromicroscopy [5]. While it is possible to measure the dimensions of the structure, this may not lead a desirable accuracy in the mathematical model since the cross section of the specimen may even not be rectangle. Side wall angles, and unsharp corners due to fabrication may need to be corrected in the geometrical parameters involved in the mathematical model.

It was mentioned that the forces are related to other quantities, which are easier to measure, in inverse tests. These quantities differ according to the type of actuation used for straining the specimen. Different techniques such as electrostatic actuation, piezoelectric actuation or nanoindentation can be used for actuation of the specimen. Despite the latter one, it is not possible to directly measure the

force. Either electrostatic or piezoelectric coupling equations should be solved in order to relate the input voltage to force. In some cases nanoindenters may be available for such applications. This renders the test method direct. However using nanoindenters may limit the design of the test device as it introduces alignment problems.

Not only the measurement errors but also the residual stresses that originate from fabrication may lead to considerable errors in testing. One of the aims in producing MEMS mechanical test devices should be to achieve stress free structures. The microfabrication techniques usually utilize high temperature changes and chemical reactions (consider etching). The difference in the thermal expansion coefficient of the different materials used in production will result in thermal stresses at the final structure. Moreover thermal stresses are not the only source for residual stresses in the MEMS devices. Intrinsic stresses arising from chemical reactions, high rate depositions, epitaxial growth, which lead to disturbance in lattice structure of the material [4], are other sources of residual stresses.

Testing methods are classified as direct and inverse methods and possible sources of errors in testing are described above. Independent of being direct or inverse methods, mechanical characterization tests can also be classified as static and dynamic testing. Static testing methods utilize static or quasi-static loading of the specimen and yield the information of static properties of the material, such as elastic modulus and yield strength. Extraction of residual strain and stress gradient information is possible without actuation of the device, which can also be called as static testing. Techniques used for extraction of the residual stress information are called as passive methods throughout this test. On the other hand dynamic testing utilizes cyclic or sudden loading of the specimen. In case of application of cyclic loading to the specimen, fatigue properties such as endurance time can be obtained.

As there are no standard testing methods in micro scale, some criteria should be defined for evaluating the existing techniques and designing new test structures. In evaluating the MEMS test devices three main items should be considered. These items are structure, actuation and measurement, where structure includes geometric and fabrication considerations. According to the above classification, considerations that should be taken into account for each item are listed in Table 1.1. Sample evaluation table prepared in accordance with these considerations is given in Appendix A.

Table 1. 1: Evaluation of mechanical testing methods in micro scale

Structure	1. Structure should be simple. That is in stiffness model, there should be small number of dimension parameters in order to decrease error due to dimension measurement. 2. Structure should be kept on-chip where available to get rid of alignment problems 3. Fabrication should introduce low or no residual stress for proper working of active (static and dynamic testing) devices.
Actuation	1. Loading state should be close to ideal, to minimize loading assumptions. 2. It should be possible to obtain enough deflection for the range of interest. 3. Especially devices for dynamic testing should be designed such that they can be used for static testing. 4. It should be kept in mind that nano-indenters introduce alignment problems.
Measurement	1. Vernier scales should be utilized when visual reading is utilized. 2. Capacitive reading introduces high accuracy and provides electronic reading. 3. Interferometry introduces alignment problems but results in real-time and accurate reading.

1.4 Thesis Organization

While the items set in Section 1.3 constitute the basis for evaluation of the methods for mechanical characterization of MEMS materials, more systematic approach is required for comparing different techniques. Some existing MEMS mechanical characterization devices and some novel test devices are fabricated for this purpose. In order to compare the performances of these devices, they should be fabricated using a repeatable microfabrication process on a material whose

mechanical properties are well defined even for micron scale. Thus it is the device characteristics that remain the only variable to be checked. Deep reactive ion etching (DRIE) of (111) oriented silicon is selected for this purpose. While fabrication on silicon on insulator (SOI) wafers is at least as repeatable as DRIE, DRIE is selected since it is the readily available resource for the study. Details of the fabrication are given in Section 3.4.

It is aimed to compare the mechanical testing devices using the data obtained from testing of the devices fabricated using DRIE, and then to conduct the tests on the devices fabricated using nickel electroplating. Additionally, devices fabricated on SOI are tested in order to obtain data for further study.

In the next chapter, theoretical background for the actuation and the elastic stiffness is presented. Also, the literature survey on the subject, existing testing methods and evaluation of these methods are given in Chapter 2.

Chapter 3 explains devices tested in this study. Development of the devices and derivation of the mathematical models of the devices are presented in this chapter.

Chapter 4 describes the passive tests and the results of the passive tests.

Chapter 5 presents the dynamic testing of the devices explained in Chapter 3. Unfortunately dynamic tests could not be conducted. The reasons are also presented in this chapter.

Chapter 6 explains static tests conducted on the devices explained in Chapter 3. Also results of the tests are tabulated in this chapter. Additionally finite element analyses (FEA) of the devices are given for verification of the results. Moreover a novel method for measurement of micro scale dimensions and deflections is presented in this chapter.

Finally, Chapter 7 includes the conclusion of the study and comments on the test results. Some suggestions for further study are also stated in Chapter 7.

CHAPTER 2

THEORETICAL BACKGROUND AND LITERATURE SURVEY

This chapter includes general background on electrostatic actuation, capacitance, and basic stiffness calculations of some mechanical components. Literature survey on the subject and brief information on the devices tested in this study are also presented in this chapter. Section 2.1 explains principles of electrostatic actuation and basics of capacitance. Section 2.2 describes stiffness calculation of some basic mechanical elements involved in construction of the test structures. Finally, Section 2.3 briefly overviews the existing test structures based on the classification of static testing, dynamic testing, and passive testing.

2.1 Electrostatic Actuation

The devices tested in this study are all actuated electrostatically. Thus the physics of electrostatic actuation should be discussed before going further.

Electrostatic actuation makes use of principle Coulomb's law, which relates the electrostatic force occurring between charged particles to charge magnitudes and the distance between the particles [6]. The force can also be related to electric field, which is the field of vectors that are perpendicular to the equipotential surfaces around the charged body. Figure 2.1 shows the electric field lines around a charged particle.

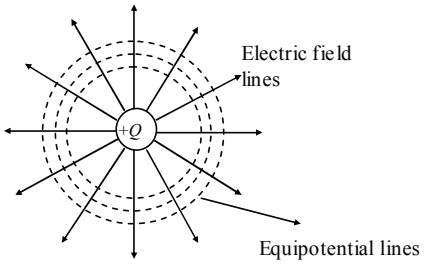

Figure 2. 1: Electric field lines around a charged particle

Keeping the principle of existence of electrostatic force between charged particles in mind, capacitance and capacitors should be comprehended in order to clearly understand electrostatic actuation. Capacitors are devices to store energy analogous to a mechanical spring. In Figure 2.2a, a parallel plate capacitor is shown with one plate $+Q$ and the other plate $-Q$ charged. According to the Coulomb's law, two plates exert attractive forces to each other. If one of these plates is free to move and supported by a mechanical spring, due to the electrostatic force, spring suspended plate will obviously move (Figure 2.2b).

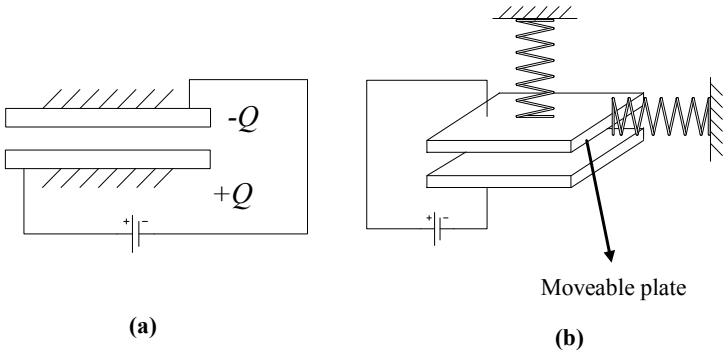

Figure 2. 2: Parallel plate capacitor

In order to calculate the electrostatic force generated between charged plates, stored energy in the capacitor should be computed. In general, the energy stored is computed by integration of effort over the displacement [4]. Since voltage and charge are analogous to effort and displacement respectively in an electrical capacitive system, the equation for the stored energy becomes

$$U = \int_0^Q V dQ \tag{2.1}$$

where V is the voltage and Q is the charge. Electrical potential and the charge in equation (2.1) are related as given in equation (2.2).

$$Q = CV \tag{2.2}$$

where C is the capacitance. The capacitance of parallel plates, ignoring the effect of fringing fields (Figure 2.3), is given by equation (2.3) [4].

$$C = \frac{\varepsilon A}{g} \tag{2.3}$$

where ε is the permittivity of the dielectric media, A is the overlap area and g is the gap between the plates. Combining equations (2.2), (2.3) and (2.1) results in equation (2.4), where the stored energy between parallel plates is related to voltage, gap and overlap area.

$$U(V, g, A) = \frac{\varepsilon A V^2}{2g} \tag{2.4}$$

In application, the moveable plate of Figure 2.2 is allowed to move either in vertical or in horizontal direction. If one of the plates of the capacitor is suspended by a mechanical spring in the manner shown in Figure 2.3, then the moveable plate is free to move in vertical direction, thus the gap varies with displacing plate.

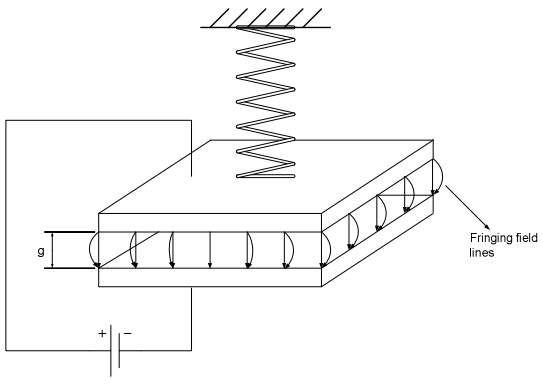

Figure 2. 3: Varying gap capacitive actuator

Electrostatic force that generates this motion can be calculated by taking the partial derivative of the stored energy expression with respect to gap, since the gap varies as the plate moves.

$$F_e = \frac{\partial Q(V, g, A)}{\partial g} = \frac{\varepsilon A V^2}{2g^2} \tag{2.5}$$

Equation 2.5 gives the electrostatic force generated in a varying gap parallel plate capacitor. It can be observed that the force changes with the square of the inverse of the gap, meaning that the force further increases with the decreasing gap. This situation leads to a stability problem called pull-in, which can be stated briefly as collapse of moving plate (electrode) on the fixed electrode after a certain limit of gap. Pull-in phenomenon is explained in details in Section 4.1.

Foregoing situation states the case, where the gap varies as the plate moves. Similarly, plate can be actuated in lateral direction with varying overlap area (Figure 2.4). In this case one of the plates is suspended and free to move in lateral direction. It should be noted that it is assumed that the motion is restrained in vertical direction; where electrostatic force is also generated.

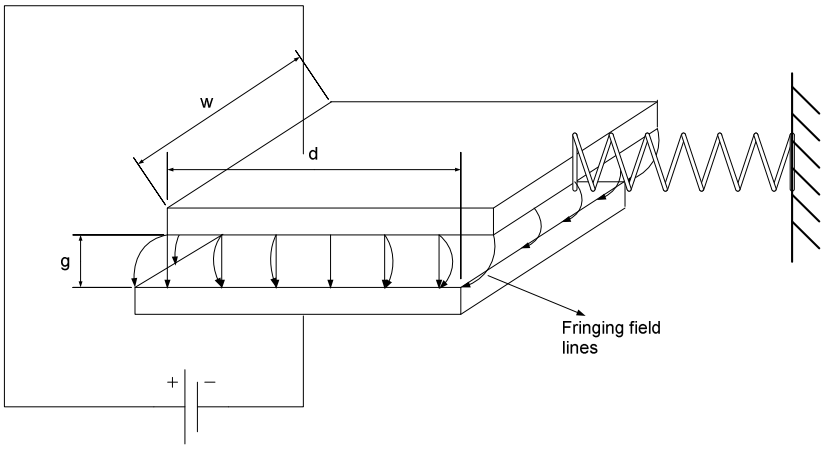

Figure 2. 4: Varying overlap area capacitive actuator

The expression for the electrostatic force quite differs from that for the previous case. Writing the equation (2.4) by expressing the overlap area in terms of width and overlap distance of the plates yields,

$$U(V,g,w,d)=\frac{\varepsilon w d V^2}{2g} \tag{2.6}$$

In the case of varying overlap capacitive actuator, it is the overlap distance that varies, not the gap. Therefore partial derivative of the above expression with respect to overlap distance gives the electrostatic force for the varying overlap capacitive actuator (Equation (2.7)).

$$F_e=\frac{\partial U(V,g,w,d)}{\partial d}=\frac{\varepsilon w V^2}{2g} \tag{2.7}$$

On the contrary to the varying gap case, electrostatic force generated does not change with the displacement, which is this time *d*. This situation automatically solves the stability problem, which exists for varying gap actuator. Since this arrangement of parallel plate capacitor solves the pull-in problem in the direction of motion, this type of actuation can be utilized in order to obtain high displacements. The actuator making use of varying overlap capacitive actuation is called lateral comb drive (Figure 2.5), which is also used for actuation of some of the test devices in this study.

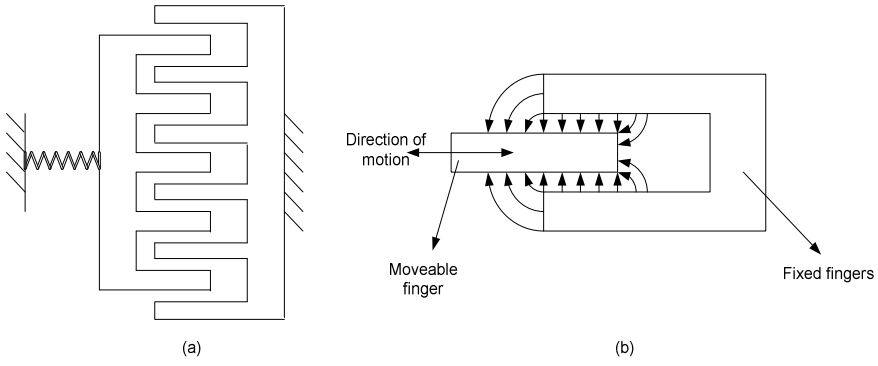

Figure 2. 5: (a) Lateral comb drive (b) One finger of the drive and the electric field lines

In this arrangement, due to symmetry of the structure, in plane forces normal to the direction of motion are cancelled out, remaining only the forces resulting from fringing electric field lines. However this equilibrium case is unstable, meaning that pull-in in transverse direction is possible for side-unstable structures, which has low stiffness in orthogonal directions to the direction of motion. This should be kept in mind especially in designing high displacement lateral comb drives, since it is actually the side pull-in that limits the motion.

For a lateral comb actuator with n inner fingers and (n+1) outer fingers, electrostatic force generated is given by the equation (2.8):

$$F_e = \frac{nb\varepsilon V^2}{g} \tag{2.8}$$

where b is the finger height and g is the gap between adjacent coupling fingers [7]. After deriving the general equations for actuation of the test specimens, the spring constants of these specimens should be calculated. Stiffness of the basic mechanical components and methods for calculation of stiffness are given in the following section.

2.2 Stiffness Calculation

Every device tested in this study contains beams in bending, as the specimen itself or as mechanical spring. The spring constants for the beams are calculated assuming deflections are in elastic limits of the materials used. Considering the loading conditions, the beams used are either two ends fixed type and point force acting at the midpoint (Figure 2.6a), or cantilever with a point force acting at the tip point (Figure 2.6b).

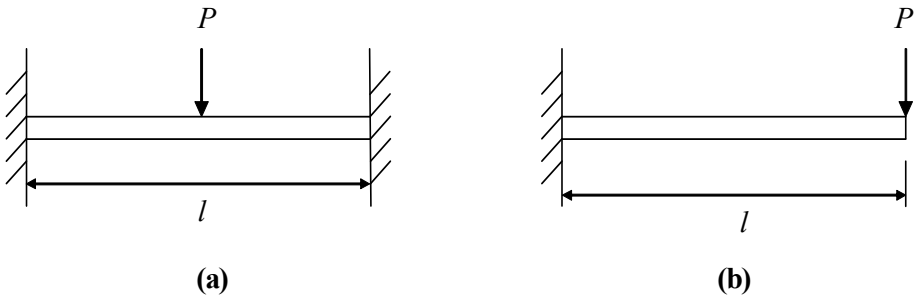

Figure 2. 6: (a) Two ends fixed beam with a point force acting at the midpoint (b) Cantilever beam with point force acting at the tip point

Assuming small deflections in elastic limit, and assuming that the material obeys Hooke's law (equation (2.9)), which states that the stress and the strain are proportional with the modulus of elasticity in elastic limit, deflections can be computed by various methods, some of which are mentioned throughout this section.

$$\sigma = E\varepsilon \tag{2.9}$$

where σ is stress, E is elastic modulus of the material and ε is the strain.

Derived formulas are readily provided for the above two cases of beams. Tip deflection for the cantilever beam loaded with concentrated force at the tip point is defined by the equation (2.10) [14].

$$\delta = \frac{Pl^3}{3EI} \tag{2.10}$$

where I is the area moment of inertia about the axis of bending, E is the elastic modulus, P is the applied load and l is the length of the beam. Since linear spring constant for a mechanical spring is defined as the ratio of the applied force to the deflection, spring constant for the cantilever beam is found to be as in equation (2.11).

$$k_c = \frac{3EI}{l^3} \tag{2.11}$$

Similarly the mid point deflection for the two ends fixed beam loaded at the mid point with a point force is given in equation (2.12) [14].

$$\delta = \frac{Pl^3}{192EI} \tag{2.12}$$

Therefore the spring constant for the two ends fixed beam is

$$k_f = \frac{192EI}{l^3} \tag{2.13}$$

Deflections and spring constants of the beams in the devices, which are loaded in different manners than the above-mentioned cases, are computed by using moment-area method [14]. The derivations for these cases are given in Appendix B.

2.3 Previous Designs for Mechanical Characterization

As stated above in section 1.3, mechanical testing can be classified as static and dynamic testing, and passive testing which do not require actuation. Ongoing studies on mechanical characterization of MEMS materials lead to development of different test structures. Existing test devices are explained in details in following sections.

2.3.1 Passive Testing

As stated at the beginning of the Section 1.3, passive tests, which do not involve any type of actuation, are used for determining residual stresses and stress gradients, which possibly originate during fabrication.

One of the structures for determination of the residual strain involves the use of two different length beams and a vernier gage for measuring the deflection [12]. The structure shown in Figure 2.7 consists of two different length beams paired at one end by a tip beam and a vernier scale attached to an extension lever connected to the tip beam. The residual stress formed in the structure results in the

differential deflection of two test beams. The difference in deflection is transmitted to the extension lever as rotation, since the beams are coupled by the tip beam. The rotation of the extension lever, which is related to the residual strain, can readily be measured visually using the vernier scale.

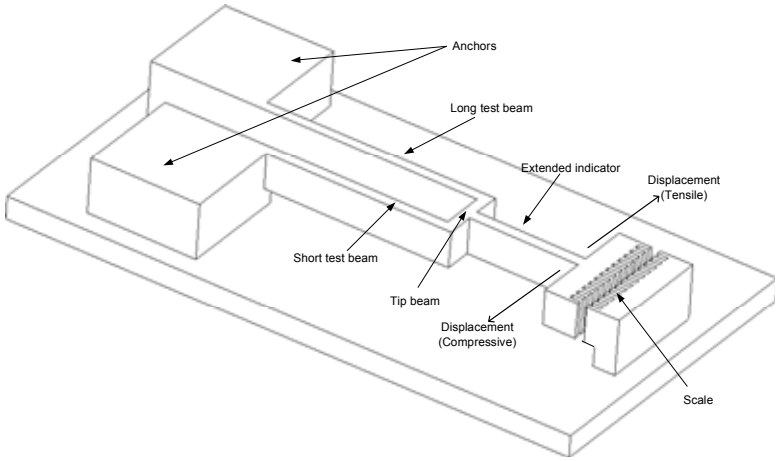

Figure 2. 7: Device for determination of residual strain [12]

Utilizing the extension beam magnifies the rotation due to straining and possibly leads to easy measurement of the residual strain. However, this requires the in plane deflection of both of the beams which may not be the case. The beams possibly deflect out of plane and this completely hinders the functioning of the device.

2.3.2 Dynamic Testing

One electrostatically actuated device is given as an example for fatigue characterization of MEMS in this section. The device is designed for investigating the fatigue and creep of MEMS [11]. The structure, shown in Figure 2.8, consists of a 10 μm long electroplated Ni beam connected to a relatively thick lever which is deflected through a thin lever connected to an electrostatic actuator. Voltage is applied to the actuator in order to pull-in the electrode. The electrode is then released back by cutting off the voltage (Figure 2.9). This cyclic motion is repeated to obtain fatigue data for the test beam. The test beam is designed to be

considerably shorter than the actuating lever in order to concentrate the stress at the test beam. As the length and the width of the test beam vary, maximum stress at the test beam varies. Consequently endurance time for different stress levels, thus the stress versus number of cycles (SN) curve for the test material can be obtained. It should be noted that there are bumpers placed at the end and the mid of the electrodes in order to prevent stiction of the electrodes during pull-in.

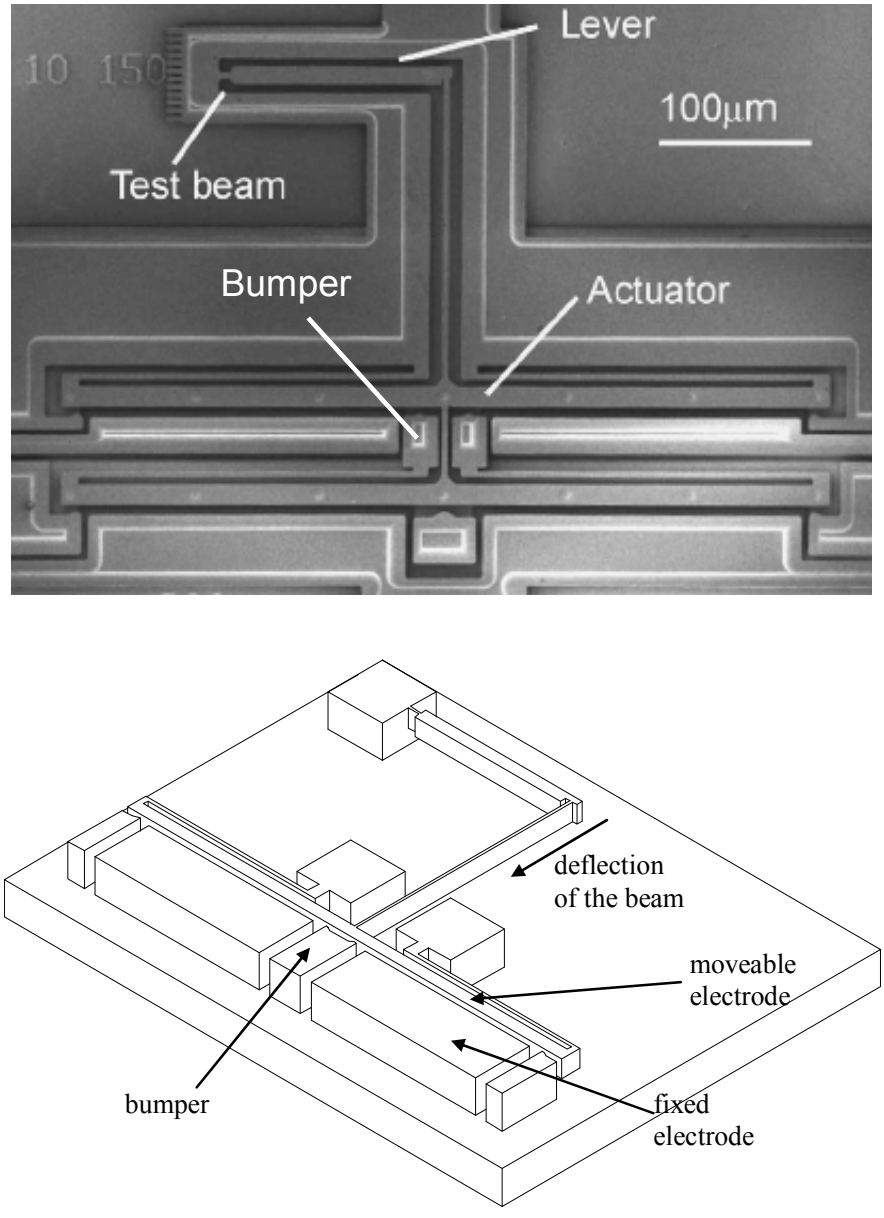

Figure 2. 8: Electrostatically actuated device for fatigue testing of electroplated Ni [11]

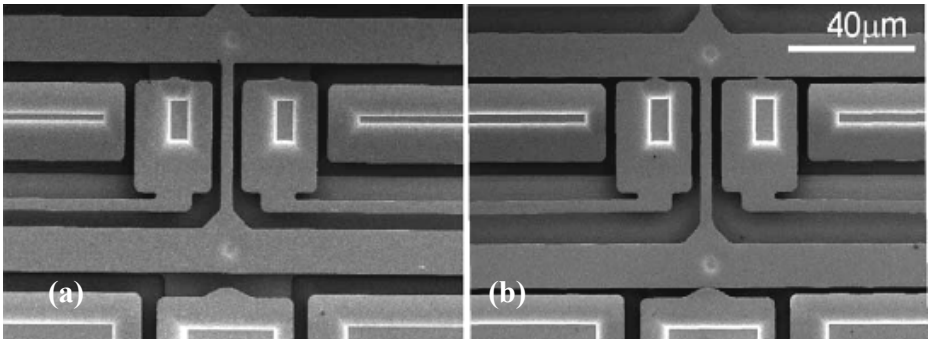

Figure 2. 9: (a) Released state of the moveable electrode (b) Pull-in state of the moveable electrode. Note that the bumpers prevent stiction. [11]

In order to observe fatigue failure in a dynamic test, either number of cycles should be increased or the difference between the maximum and the minimum stress levels should be kept high. In the above case two stress states are the pull-in and zero stress cases, and it is reported that no fatigue failure observed after a reasonable number of cycles [11]. Therefore it may be possible to observe fatigue failure by applying two pull-in states in opposite directions, which will increase the difference between the maximum and minimum stress levels.

2.3.3 Static Tests

In this section four static testing methods with different actuation mechanisms are examined. Advantages and shortcomings of each test structure are determined and presented throughout the section.

It is stated in previous sections that the actuation can be achieved electrostatically, piezoelectrically, directly using nanoindenters, or by other possible means such as thermal. Below in Figure 2.10, a piezoelectrically actuated tensile test device is shown [8]. One end of the structure is composed of 50 nm thick sputtered aluminum specimen on force sensor beam of single crystal silicon, while the other end of the device is composed of elastic supporting beams where the specimen is pulled through a piezo-actuator (Figure 2.10a). As the specimen is strained, marker A and marker B are displaced. Displacement of marker A and marker B

are used to measure the displacement of the specimen. Difference between the displacements at marker locations A and B gives the elongation of the tensile specimen. Product of displacement at marker A and the stiffness of the force sensor beam gives the force transmitted through the specimen.

The device involves multiple supporting beams. These beams prevent the bending and torsion of the specimen during loading, which results in pure tension of the beam.

The structure is in general well-designed. Also utilization of piezo-actuator is good for generation of enough force to actuate such a stiff structure (Note that the stiffness of a tensile specimen is very high compared to any other configuration, such as bending.). However visual reading of the displacements at marker locations may not be accurate enough. Utilizing vernier scales at marker positions may lead to higher accuracy in measurement.

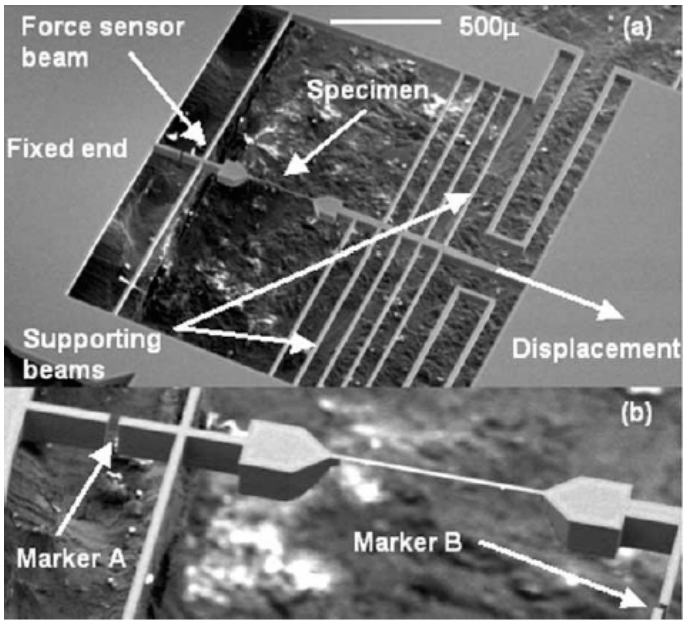

Figure 2. 10: (a) Components of the tensile test device (b) Markers for measuring the displacements at the two ends [8]

Another static testing technique is so called membrane deflection experiment (MDE) [9], which utilizes nanoindenter with a line edge (Figure 2.11). The structure is composed of 1 μm thick; both ends fixed gold membrane (Figure 2.11a). The span of the membrane is not uniform but the middle of the span has additional width for the contact area, where the line load is applied through the nanoindenters. This additional contact area minimizes the stress concentration at gage sections. The device works such that as the indenter engages the membrane, the gage sections are simply exposed to tension since the moment of inertia of the membrane is so small due to its thin cross-section (Figure 2.11b). The deflection data is extracted through a microscope interferometer placed under the specimen. The fringes allow the real time measurement of the membrane deflection.

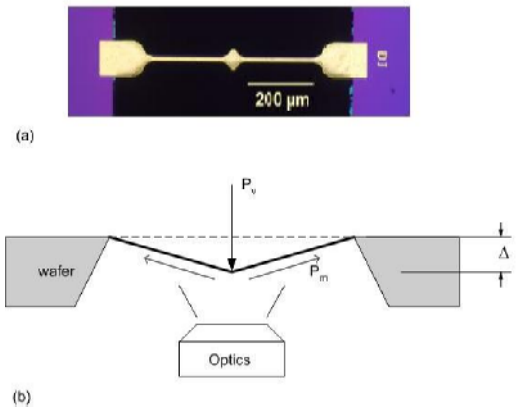

Figure 2. 11: (a) Membrane deflection test structure (b) Deflection model [9]

Although interferometer is utilized for measurement purposes, which in turn possibly improves the accuracy, using nanoindenter introduces alignment problems in case of membrane deflection test.

Third static test device is the electrostatically actuated cantilever bending test [7]. In this method, a cantilever beam is electrostatically actuated through a lateral comb drive (Figure 2.12). The device is composed of 2 μm thick cantilever beam made of sputtered aluminum, and a lateral comb drive for electrostatic actuation of the beam.

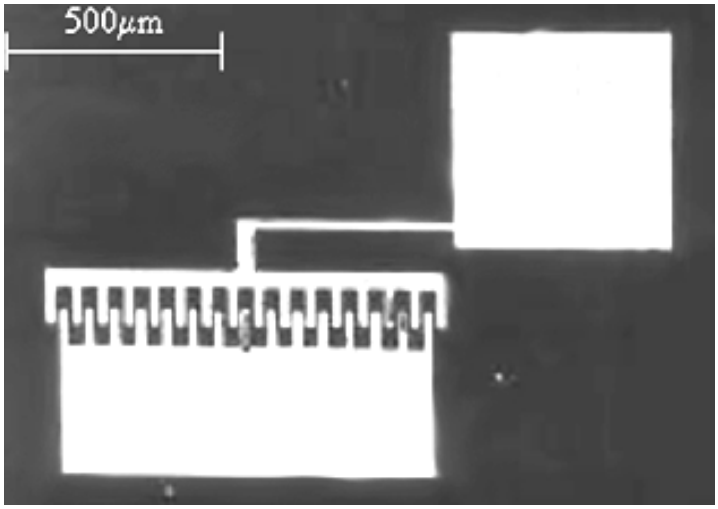

Figure 2. 12: Electrostatically actuated cantilever beam [7]

Since the structure is very simple, it is very easy to develop and implement the mathematical model. However, due to asymmetry of the structure, there is nonlinearity during loading. As the beam is deflected, due to the tip deflection angle, moveable comb rotates. Thus an asymmetric electric field forms between the fingers of the comb drive, which in turn leads nonlinear loading of the beam.

The fourth device shown in Figure 2.13 involves bent beams as structural element [10]. A bent beam pair is connected to each other through a beam with tines on it. Beam pairs, which are bent in opposite directions are placed successively forming the differential capacitive strain sensor [10]. Bent beams response to the voltage biased across the bent beams by transition of the apex. Apexes of the beams bent in opposite directions move in relatively opposite directions, which increases or decreases the capacitance between the tines of the neighboring bent beam sets. However tines are placed such that, capacitance increases (or decreases) between the tines of A and C in the figure, while the capacitance decreases (or increases) between the tines of A and B. The difference between C_{AC} namely the capacitance between A and C, and C_{AB} is hereby related to the voltage.

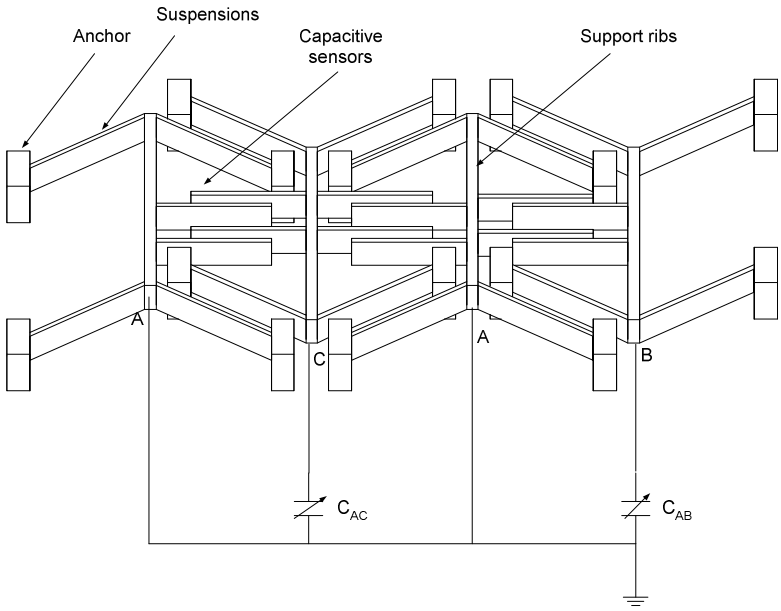

Figure 2. 13: Differential capacitive strain sensor [10]

Most important superiority of the method is that the capacitive measuring definitely increases the precision.

This section overviews the existing test devices used for mechanical characterization of MEMS materials. Some of these devices and some novel test devices are fabricated in this study for testing purposes. The devices tested are explained in details in the following chapter.

CHAPTER 3

DEVICES TESTED IN THIS STUDY

After over viewing some of the existing micro test structures, the devices tested in this study are explained in details in this chapter. The devices tested are described under the classification of passive tests, dynamic tests, and static tests, as it is in the previous chapter. Section 3.1 explains passive test devices. There are two passive test devices fabricated. One is the bent beam strain sensor [13] and the other is the cantilever beam for stress gradient measurement. The models governing the functioning of the devices are given in Section 3.1. Section 3.2 describes the dynamic testing devices. There are two devices fabricated for dynamic testing. One is the cantilever beam bending device of Larsen [11] explained in Section 2.3.2. Other one is the improved version of this device. Testing procedure and the analysis of the device structure is given in Section 3.2. Section 3.3 describes three different static test devices. First one is the improved version of the cantilever beam bending device [7] explained in Section 2.3.3. Second device utilizes double clamped beam instead of cantilever for bending. Third static test device is the cantilever beam pull-in test device. There are two versions of this device. Both are explained in Section 3.3. Mathematical models of the devices and device dimensions are also given in this section.

The devices are fabricated by deep reactive ion etching of (111) oriented silicon and electroplating nickel. Only primitive version of the cantilever pull-in device is fabricated on (100) oriented silicon on insulator wafer. The fabrication details of the devices are presented in Section 3.4.

3.1 Passive Test Devices

Passive tests are actually the prerequisite for static testing. Static testing models assume no or negligible residual stresses. In order to verify this, passive tests should be conducted beforehand. As mentioned above two different passive test devices are fabricated for this study as mentioned above. Actually the devices are used to inspect two different characteristics of the fabricated structure. Bent beam strain sensor is used to detect any residual straining due to uniform residual stress across the structure. However, there may be a stress gradient accompanying the uniform residual stress or only residual stress gradient across the structure may exist. Cantilever beams for stress gradient measurement are used to detect the stress gradient in this case. In the following subsections both devices are explained in details.

3.1.1 Bent Beam Strain Sensor

Strain sensor of Que [13] utilizes bent-beams, which are composed of two freestanding beams bent at an angle and connected to each other forming an apex (Figure 3.1). As the beams are released at the end of fabrication, the residual stresses formed in the structure cause the beams to deform. Due to the bent angle, the beams tend to buckle in the manner shown in Figure 3.2. The buckling of the beam results in the linear motion of the apex. The linear motion of the apex is visually read out using a scale attached at the apex. In order to amplify the output, two symmetric bent-beams are used. This doubles the displacement, facilitating the measurement.

However device dimensions should ensure buckling in the desired manner. If the area moment of inertia of the cross section of the beam about the buckling axis is very high then the beams may buckle in orthogonal direction. This means the beams may buckle out of plane, hindering the motion of the apexes. This may also hold true if the bend angles are very low. In the limit, the bent beams approximate to straight beams in this case.

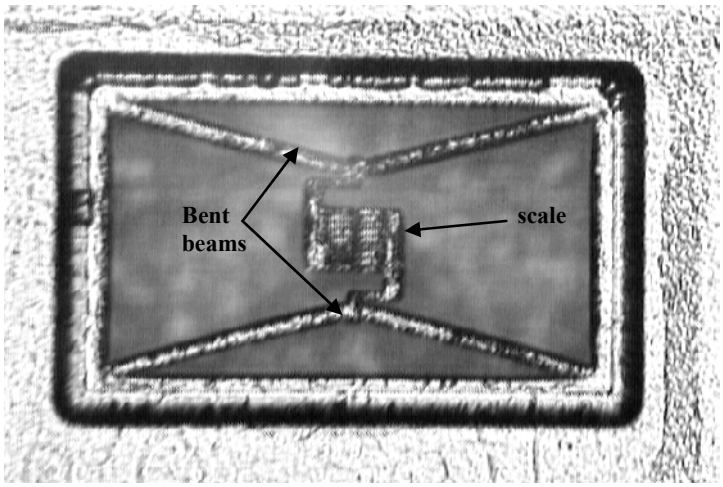

Figure 3. 1: Bent beam strain sensor on electroplated nickel

Consequently the bend angle ∅ on Figure 3.2 determines the behavior of the device and the displacement of the apex. The bending angle forces the beams to buckle at the apex under compressive stress. It also provides displacement of apex under tensile stress. Varying bend angle alters the sensitivity of the device. However, keeping the bend angle very small may result in out-of plane buckling of the beams, as mentioned above. Also in case of a residual stress gradient, the structure becomes totally useless, since this certainly results in out-of plane buckling.

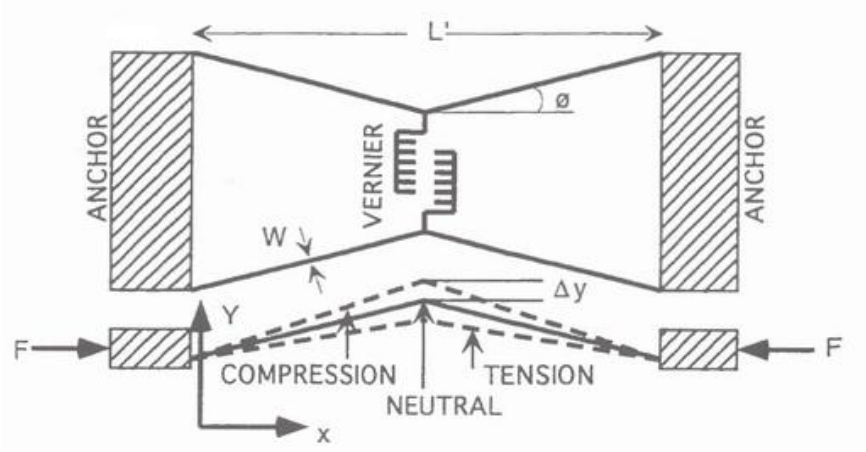

Figure 3. 2: Displacement of the apex in the bent beam strain sensor [13]

Mathematical model of the device is derived by physically modeling the structure as shown in Figure 3.3. In this model compressive or tensile forces cause the apex to move. Also the boundary conditions are set through this physical model.

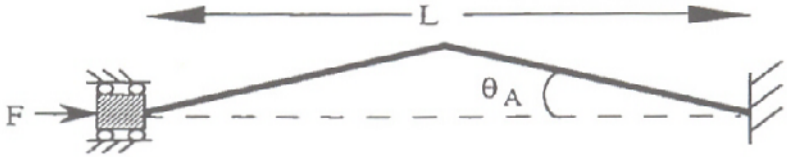

Figure 3. 3: Physical model for the bent beam strain sensor [13]

For the beam material with elastic modulus E, and beam with moment of inertia I, displacement of the apex is found to be

$$y = \frac{\tan\theta_A}{k} \cdot \left[\tanh\frac{kL}{4} \cdot (1 - \cosh kx) + \sinh kx \right] \tag{3.1a}$$

for tensile F, and

$$y = \frac{\tan\theta_A}{k} \cdot \left[\tan\frac{kL}{4} \cdot (1 - \cos kx) + \sin kx \right] \tag{3.1b}$$

for compressive F, where $k = \sqrt{\frac{F}{EI}}$ and $x = \frac{L}{2}$ [13].

The residual stress in the structure is given by [13]

$$\sigma = E\varepsilon = \frac{E}{L}\left(\Delta L' + \frac{FL}{Ewh} \right) \tag{3.2}$$

where w is the width, h is the thickness of the beam, $\Delta L'$ is the change in L', which is the difference between the actual length of the beam and its projected length along x axis [13]. L' is found to be

$$L' = \frac{(\tan\theta_A)}{4k} \cdot \left[2H + kL - kLH^2 + \sinh kL - 2H\cosh kL + H^2\cosh kL \right] \tag{3.3a}$$

for tensile F, and

$$L' = \frac{(\tan\theta_A)}{4k} \cdot \left[2G + kL + kLG^2 + \sin kL - 2G\cos kL - G^2 \sin kL \right] \qquad (3.3b)$$

for compressive F, where $G = \tan\frac{kL}{4}$ and $H = \tanh\frac{kL}{4}$ [13].

Assuming an elastic modulus for the structure material, residual stress level can be related to the displacement of the apex of the bent-beams.

Design dimensions of the device are shown in Figure 3.4. The same dimensions used by Que [13] are assigned to the devices. It should be noted that the width of the beams and the bend angles vary. Using different dimension structures, it may be possible to conclude on the sensitivity of the structures.

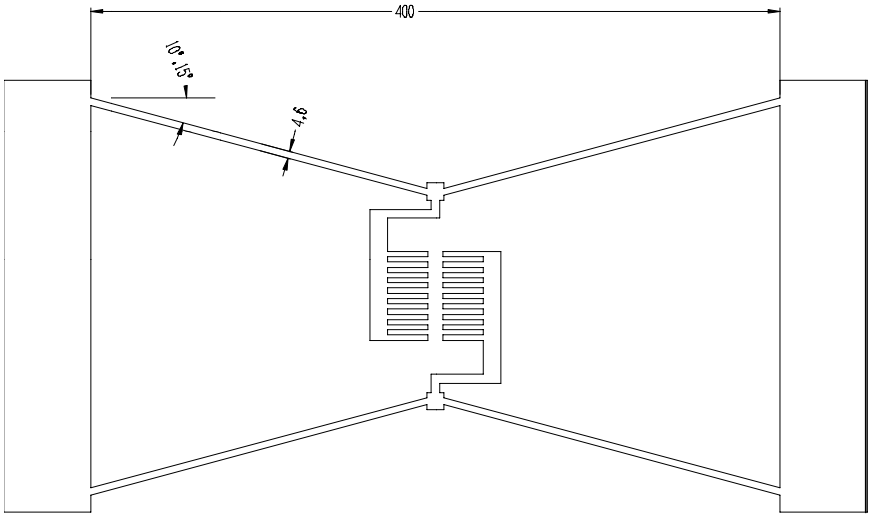

Figure 3. 4: Bent beam strain sensor, design dimensions (Note that the dimensions are in microns.)

3.1.2 Cantilevers for Stress Gradient Measurement

In case of a stress gradient bent beam strain sensor may not function properly. Due to the stress gradient, the beam would tend to bend out of plane. Actually stress gradient is a more common case in deposited thin film structures, and

should be evaluated. In order to detect the stress gradient effects, cantilever beams of varying lengths (Figure 3.5) are commonly used.

Tips of the cantilevers at different lengths deflect upward or downward. depending on whether the stress at the top surface is tensile or compressive. It is possible to relate the tip deflection to maximum residual stress [4]. Then it is the problem of measuring the tip deflection. Tip deflection in that case, is the difference between the focal distance of the tip and the anchor, which can be measured by using an optical profiler. The profiler detects the focal planes by scanning the structure from top to bottom. Thus deflection curves of the beams can be obtained.

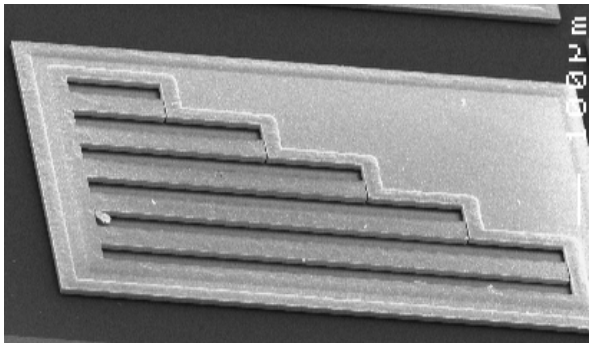

Figure 3. 5: Cantilevers for residual stress gradient measurement

For a cantilever beam, assuming a uniform stress gradient in the structure, the stress distribution across the beam before release will be as shown in Figure 3.6a. Note that after release, beam deflects and stress relaxation is observed. It should be stated that Figure 3.6b illustrates the case, where the stress at the top is tensile. If the stress at the top is compressive, the beam would bend upwards. Also it should be noted that the stress gradient is assumed to be uniform, which is a common application in stress gradient measurements.

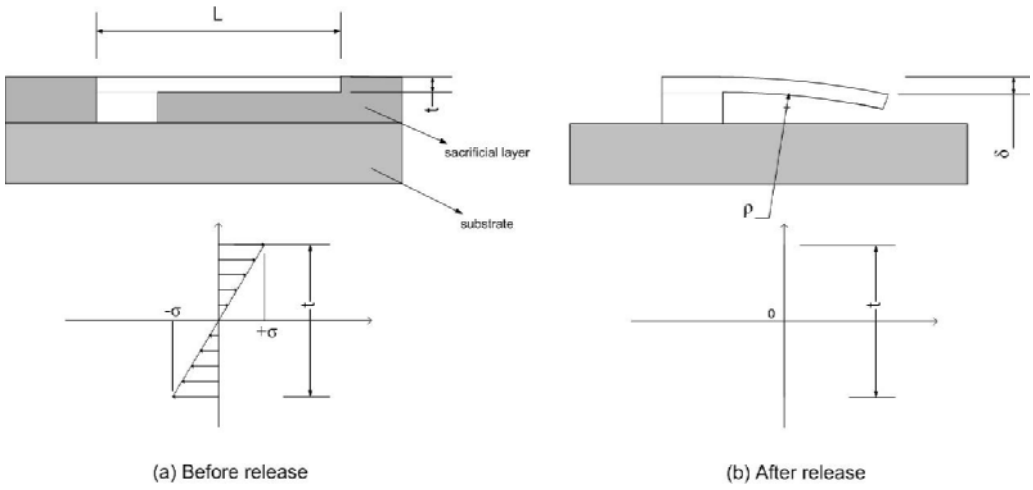

Figure 3. 6: Deflection of the cantilever beam due to residual stress

After analyzing the device structure, the model relating the tip deflection to the maximum stress is derived below.

The cantilever beam should be treated as plate considering the anticlastic curve [4]. This approach yields the equation relating the radius of curvature of deflection to maximum residual stress (equation (3.4)).

$$\sigma = \frac{1}{2}\left(\frac{E}{1-\nu}\right)\frac{t}{\rho} \tag{3.4}$$

where E is the elastic modulus and ν is the Poisson's ratio. Radius of curvature can be related to tip deflection as [4]

$$\delta = \rho\left(1-\cos\frac{L}{\rho}\right) \tag{3.5}$$

Simultaneously solving two equations gives the maximum residual stress for a specified cantilever, whose tip deflection is known.

Actually the design dimensions of the device are not so critical, since the device is not active. However the beams are commonly fabricated in lengths varying from 200 μm to 1000 μm.

3.2 Dynamic Test Devices

Most of the MEMS devices are exposed to cyclic loadings during its lifetime. These cyclic loadings result in different levels of stresses at critical locations of the device of subject, which affects the endurance time of the device. Therefore the fatigue behavior of the materials, used in the fabrication of the MEMS structures, should be extracted in order to verify the designs. Various test devices can be designed for extraction of fatigue properties of the MEMS materials. In this study, fatigue testing device of Larsen [19], which involves cantilever beam bending is fabricated for testing. It should be recalled that the device is explained in Section 2.3.2. Possible improvements on the device are proposed and the improved version of the device is also fabricated for testing. The device structure is explained in details in the following sub-section. Different from the passive tests and the static tests conducted in this study, finite element analysis is used to determine the stress levels for different dimensions of structures. The analysis results are also given in this section.

3.2.1 Cantilever Beam Bending

Fatigue testing device of Larsen is mainly a cantilever specimen exposed to pure bending (Figure 2.8). It should be recalled that the bending of the beam is achieved by pulling in the moveable electrode connected to the actuation lever. Figure 3.7 illustrates the pull-in state of the structure. Note that the bottom section of the actuation lever is thinned in order to provide stress concentration. This section is the test beam. Thus maximum stress level occurs at the test beam during cyclic loading (Figure 3.7). It should also be recalled that in order to prevent stiction of electrodes in pull-in, which is the local welding of the electrodes due to short circuit; bumpers are located in front of the moveable electrode. These bumpers stop the moveable electrode and leave a secure gap between electrodes (Figure 2.8).

Fatigue testing requires cyclic loading of the structure. Load states in one cycle involve the pull-in state of the structure and the released state in the design of Larsen. That is pull-in voltage and zero voltage is applied successively in one cycle, yielding maximum and zero stress in the test beam (Figure 3.8a).

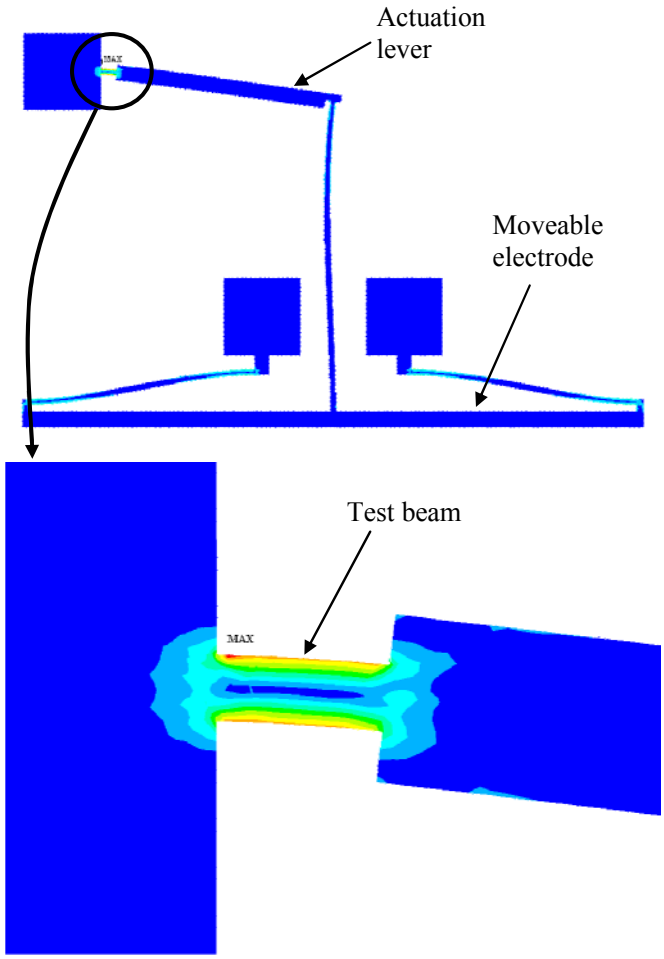

Figure 3. 7: Concentrated stress at the test beam

Although the device is designed for fatigue testing of the material, it is reported for the structure that no failure is observed up to approximately 10^8 cycles for any of the tested samples of electroplated nickel [11]. While this result verifies that the material has superior fatigue properties, the structure should be improved in order to observe failure and determine the fatigue life for different stress levels. In order

to achieve this, stress states in the load cycle should be changed. The test beam in the fatigue testing device of Larsen is pulled-in in one direction and released. This means the maximum stress occurs in pull-in state and minimum stress is zero, which is the case of fluctuating stress [20]. That is the ratio of the minimum stress level in the cycle to maximum stress level is zero (Figure 3.8a). However if the beam is pulled-in with identical actuation in both directions, the load cycle will be composed of an alternating stress, which is equal to the maximum stress in magnitude (Figure 3.8b).

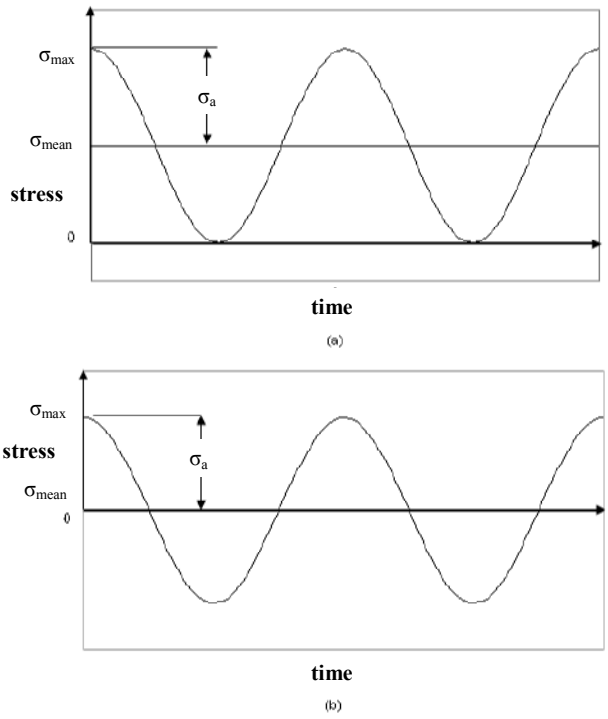

Figure 3. 8: Stresses in load cycle for the previous design of fatigue testing device (a), and the improved design (b). Note that σ_{max} occurs at pull-in.

Increasing the alternating component of the stresses in the load cycle obviously increases the possibility to observe fatigue failure. By this way it may be possible to define the endurance times for different stress levels. The resulting improved fatigue testing structure is shown in Figure 3.9.

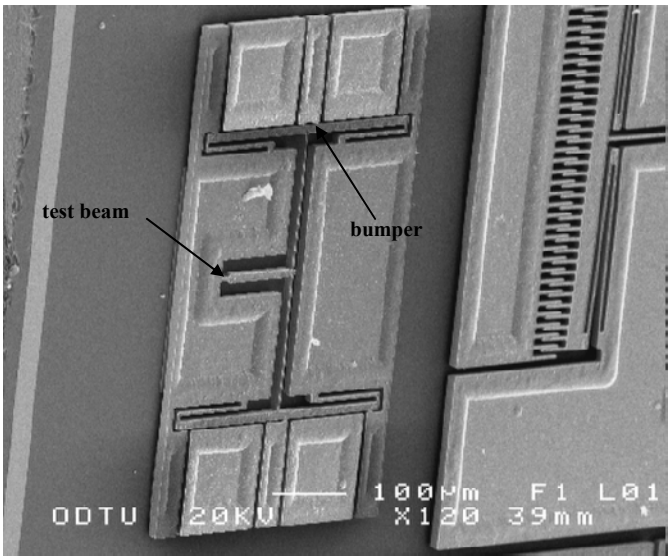

Figure 3. 9: Improved fatigue testing device on electroplated nickel

Both cantilever beam bending device of Larsen and the improved version of the device are fabricated in order to extract fatigue properties of the structural material. In order to establish the fatigue properties of the structural material, tests should be conducted at different stress levels for a number of samples. In order to provide different stresses at the test beam, length of the test beam is altered. The design dimensions are the same with those of the devices tested previously [11]. The design dimensions are given in Figure 3.10. The gap spacing is set to 6 µm for each sample, providing a safety gap of 2 µm at bumper location in order to avoid stiction.

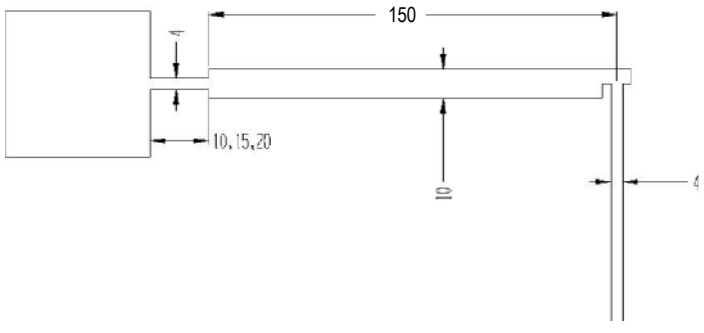

Figure 3. 10: Fatigue testing device design dimensions (in µm)

Maximum equivalent stress is computed for each of the device using finite element analysis. Both 2D and 3D models are analyzed in order to compute the maximum von Mises equivalent stress on ANSYS 7.0. Elastic modulus of 200 GPa [22] is assumed for electroplated Ni samples and 169 GPa, which is actually a well defined value for (111) oriented silicon wafers [21], is assumed for DRIE Si samples. The elements used for analyzing the 2D models are 8 node quadrilateral PLANE82 elements PLANE82 elements are used in plane stress with thickness mode [17] in order to define the structure thickness in the finite element model. The elements used in modeling the 3D structure are 10 nodes SOLID187 elements. The element is tetrahedral with quadratic shape function, and suits meshing irregular structures [17]. The analyses are carried on for each set of structures and it is observed that both 2D and 3D analyses yield similar results (Figure 3.11).

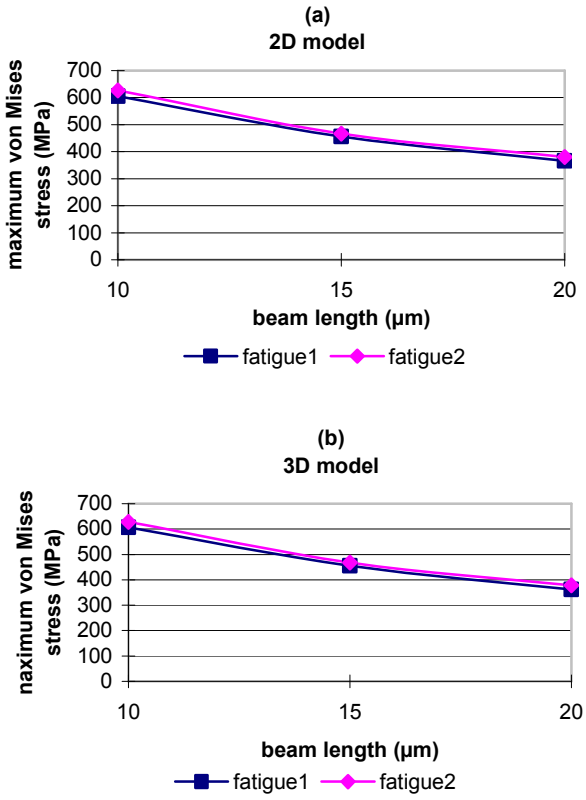

Figure 3. 11: FEA results for test structures of electroplated nickel with (a) 2D models (b) 3D models (fatigue1 denotes previous design, fatigue2 denotes the improved design)

Figure 3.11 also shows that analysis of the improved design yields slightly greater results, which is actually not foreseen, since the strain should be the same for both of the structures.

Apart from the model dimensionality, convergence should also be considered in evaluating the analysis. It is observed that 2D models converge faster than 3D models. Figure 3.12 shows the convergence behavior of the analysis of the former design for both 2D and 3D models. Thus it is concluded that it is feasible to conduct the analyses using only 2D models.

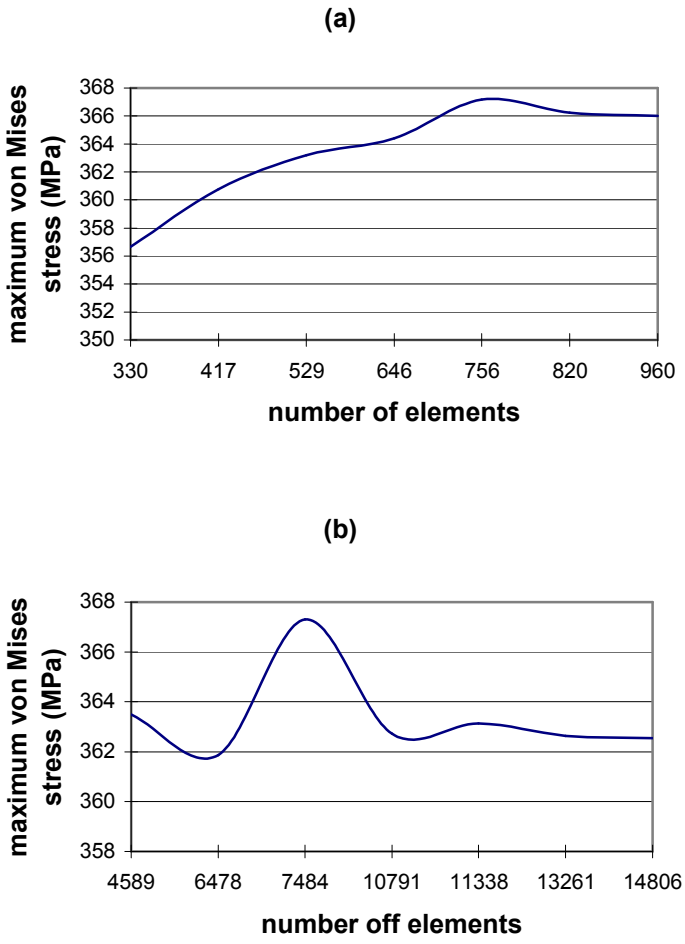

Figure 3. 12: Convergence for the (a) 2D model of the previous design (b) 3D model of the previous design (Only results for the structure with 20 µm test long beam of electroplated nickel is shown)

Resulting maximum stresses at the test beams of different lengths for both electroplated Ni and (111) oriented DRIE Si samples are tabulated in Table 3.1.

Table 3. 1: Maximum equivalent von Misses stresses (MPa) at the test beams of different lengths (fatigue 1 denotes the previous design, fatigue 2 denotes the improved design)

	Electroplated Ni samples		DRIE (111) Si samples	
	Fatigue 1	Fatigue 2	Fatigue 1	Fatigue 2
10μm test beam	605	627	510	535
15μm test beam	457	467	385	401
20μm test beam	366	380	309	322

3.3 Static Test Devices

Static test devices in this study can be classified according to the type of actuation as lateral comb actuated devices and pull-in actuated devices. Lateral comb actuated devices are the bending tests. While two types of bending tests utilize cantilevers and double clamped beams as specimen, pull-in actuated test device uses cantilever beams as test specimen. In the following subsections design and modeling of each device are given in details.

3.3.1 Cantilever Beam Bending Test

Cantilever beam bending test device is basically the improved version of the electrostatically actuated cantilever bending test [7] explained in Section 2.3.3 (Figure 2.12). It should be recalled that the device simply composes of a lateral comb drive attached at the tip of a cantilever beam anchored at one end. It should also be recalled that the moveable electrode of the lateral comb actuator tends to bent as the cantilever deflects in this design. This improved version mainly solves the problem of non linear loading due to the rotation of the electrode.

First measure to solve this problem is thinning of the lever connecting the cantilever to the moveable comb. Thin lever at the connection sites behave as a hinge. Hinges at the connection sites hinders the transmission of moment to the comb. Preventing the transmission of the moment also prevents the moveable comb from rotating at the tip angle of the cantilever (Figure 3.13). While this is an important measure, it does not fully satisfy the task. In order to better improve the structure of the actuation mechanism, suspensions are attached at the two ends of the moveable comb. These suspensions increase the stiffness of the comb at the two ends in the direction of the motion, preventing the comb from rotating with the tip of the cantilever beam. One disadvantage of this measure is that, some of the energy is wasted for bending the suspensions. Thus the stiffness of the suspensions should be kept as small as possible in order to minimize the waste of energy.

Another improvement on the previous design is to attach an extension lever at the tip of the test beam in order to magnify the deflection. Also scale is placed opposite to this extension. Thus the tip of the extension lever behaves like a pointer enabling a better visual read-out. Figure 3.13 shows the improved cantilever beam bending test.

The structure of the device (Figure 3.13) allows us to make some assumptions. First assumption arises from the thin lever connecting the moveable comb and the test beam. The thin lever behaves like a hinge at the connection point with the test beam. Normally, connecting the beam to a guided comb through a lever results in the case of one end guided, one end free beam, whose deflection curve is completely different from the cantilever case. However using thin connection lever makes the beam converge to a cantilever. As a result, stiffness of the beam is calculated as if it is a cantilever, loaded with a point force.

Second assumption is due to thick moveable comb. The thickness causes the comb to obtain rigidity in the direction of motion. Also identical suspension

spring at two ends of the moveable comb prevents the in-plane rotation of the comb. As a result, displacements at three points namely the connection points of the moveable comb with the lever, with the left suspension and with the right suspension, are assumed to be the same.

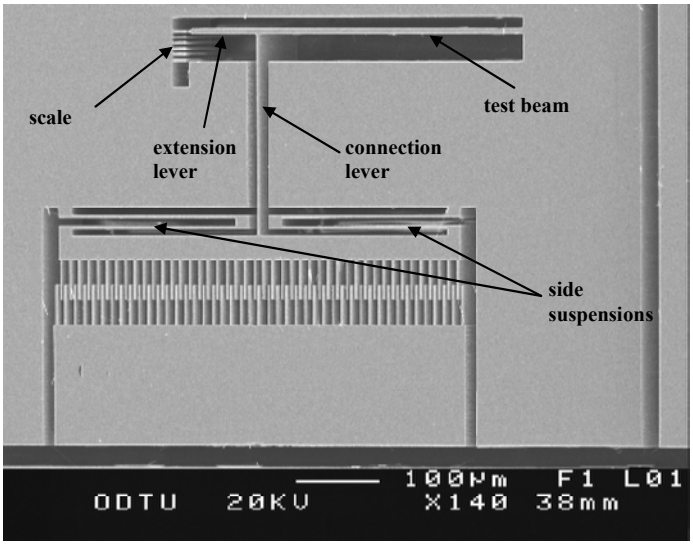

Figure 3. 13: Improved cantilever beam bending test structure on deep reactive ion etched (111) Si

The assumptions stated above results in the lumped model of the device in Figure 3.14. In the figure, k_s denotes the stiffness of the suspension springs, and k_c denotes the spring constant of the cantilever at point, where the concentrated load is applied.

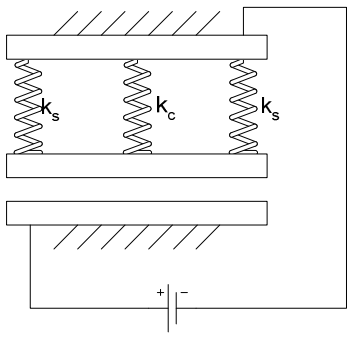

Figure 3. 14: Lumped model of the cantilever beam bending test device

Before deriving the mathematical model for the device, general equation of motion should be recalled (equation (3.6)).

$$F = m\delta'' + b\delta' + k\delta \tag{3.6}$$

where m is the mass of the moving body, b is the damping coefficient and k is the spring constant of the specimen for this case. For the quasi-static case, which holds true for static tests, inertial and damping effects can be ignored. Therefore, since the system is quasi-static, restoring force is the only force to meet the externally applied force. Thus, for the case, the equation of motion becomes

$$F_e = k\delta_{tip} \tag{3.7}$$

According to Figure 3.14, the stiffness of the structure is

$$k = k_c + 2k_s \tag{3.8}$$

Linear spring constant of the cantilever beam is given in equation (2.11). However, in this case the cantilever is not loaded at the tip, but at a point other than the tip, leaving an extension lever for amplifying the deflection. The case is illustrated below in Figure 3.15.

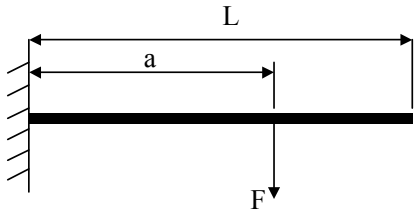

Figure 3. 15: Cantilever beam with concentrated load at any point

The equation relating the tip deflection to the point force for a cantilever beam is given in equation (3.7) [14].

$$\delta_{tip} = \frac{Fa^2}{6EI} \cdot (3L - a) \tag{3.9}$$

Examining the Figure 3.14, it can be seen that the electrostatic force applied through the lateral comb drive is shared between the cantilever and the suspensions. Defining the force on the cantilever as P_c and the forces on the suspensions as P_s (Forces on both suspension spring is assumed to be equal due to symmetry.), and defining the length of extension lever as l_e, and a in Figure 3.15 as l_c, the tip deflection becomes

$$\delta_{tip} = \frac{P_c l_c}{6EI} \cdot (3l_e + 2l_c) \tag{3.10}$$

According to Figure 3.14, the electrostatic force is shared between the suspension springs and the cantilever as

$$F_e = 2P_s + P_c \tag{3.11}$$

The deflections of the suspension springs and the cantilever at the point where the connection lever is engaged should be the same. Therefore the forces P_s and P_c are related such that

$$P_s = \frac{k_s}{k_c} \cdot P_c \tag{3.12}$$

Combining equations (3.9) and (3.10) results in

$$P_c = \left(\frac{k_c}{2k_s + k_c} \right) F_e \tag{3.13}$$

Defining the second area moment of inertia about the bending axis as

$$I = \frac{1}{12} t w_c^{\,3} \tag{3.14}$$

Therefore the stiffness for the cantilever of length l_c, width of w_c and thickness of t, at the point, where the concentrated force is applied, is found to be

$$k_c = \frac{E t w_c^{\,3}}{4 l_c^{\,3}} \tag{3.15}$$

Since whole structure is fabricated through the same fabrication processes the thickness of the suspension beams is the same with that of the cantilever. If the horizontal beams constructing the suspensions are of length l_s, and of width w_s the spring constant of a suspension at one side is found to be

$$k_s = \frac{Etw_s^3}{2l_s^3} \tag{3.16}$$

Derivation of the spring constant for the suspension is given in Appendix B. Recall that the electrostatic force generated in a lateral comb drive is found by equation (2.8) Combining equations (2.8), (3.8), (3.14), (3.15) and (3.16) results in the mathematical model formulating the tip deflection of the cantilever (equation (3.17)).

$$\delta_{tip} = \frac{2n\varepsilon_o V^2}{gE} \cdot \frac{(l_s^3 l_c^2)(3l_e + 2l_c)}{(w_c^3 l_s^3 + 4w_s^3 l_c^3)} \tag{3.17}$$

where n is the number of fingers meshing in the comb drive, ε_o is the free space permittivity, g is the gap between the meshing fingers and V is the applied voltage. Other parameters are defined for the structure above.

Design dimensions are shown in Figure 3.16. The main criterion for determination of the dimensions is to obtain similar deflections for each device at similar voltage values. Also keeping the number of dimension combinations is a good practice to guarantee the survival of minimum number of samples after the fabrication. Other than these criteria, widths are basically determined according to the fabrication methods. It is known for the electroplating that the widths increase in fabrication. On the contrary, widths decrease in deep reactive ion etching. Considering these, widths can not be too thin or too thick. Resulting combination of dimensions are tabulated in Table 3.2, and Table 3.3. Table 3.2 shows the dimensions of the DRIE (111) Si structures and Table 3.3 shows the dimensions for the electroplated Ni structures. The tables also describe the device designations. These designations are used to denote specific test devices throughout the thesis.

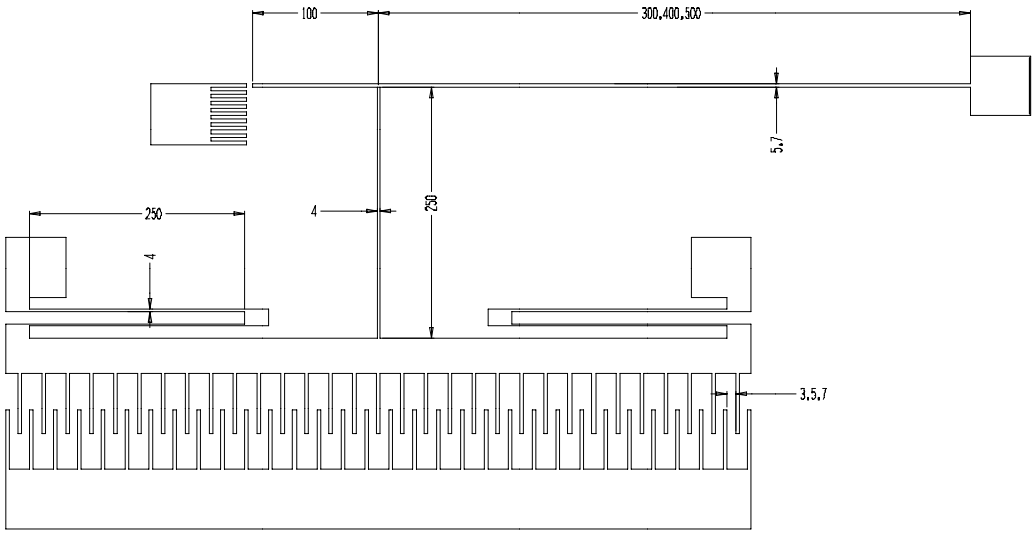

Figure 3. 16: Design dimensions of cantilever beam bending device

Table 3. 1: Cantilever beam bending test device designations for DRIE of (111) Si samples

designation	finger gap (µm)	cantilever beam width (µm)	cantilever beam length (µm)	number of finger couples in comb drive
DRIE_Cant_G3_W5_L300	3	5	300	44
DRIE_Cant_G3_W5_L400	3	5	400	44
DRIE_Cant_G3_W5_L500	3	5	500	44
DRIE_Cant_G5_W5_L300	5	5	300	34
DRIE_Cant_G5_W5_L400	5	5	400	34
DRIE_Cant_G5_W5_L500	5	5	500	34
DRIE_Cant_G7_W5_L300	7	5	300	28
DRIE_Cant_G7_W5_L400	7	5	400	28
DRIE_Cant_G7_W5_L500	7	5	500	28
DRIE_Cant_G3_W7_L300	3	7	300	44
DRIE_Cant_G3_W7_L400	3	7	400	44
DRIE_Cant_G3_W7_L500	3	7	500	44
DRIE_Cant_G5_W7_L300	5	7	300	34
DRIE_Cant_G5_W7_L400	5	7	400	34
DRIE_Cant_G5_W7_L500	5	7	500	34
DRIE_Cant_G7_W7_L300	7	7	300	28
DRIE_Cant_G7_W7_L400	7	7	400	28
DRIE_Cant_G7_W7_L500	7	7	500	28

Table 3. 3: Cantilever beam bending test device designations for electroplated Ni samples

designation	finger gap(µm)	cantilever beam width (µm)	cantilever beam length (µm)	number of finger couples in comb drive
Ni_Cant_W3_L300	6	3	300	39
Ni_Cant_W3_L400	6	3	400	39
Ni_Cant_W3_L500	6	3	500	39
Ni_Cant_W5_L300	6	5	300	39
Ni_Cant_W5_L400	6	5	400	39
Ni_Cant_W5_L500	6	5	500	39
Ni_Cant_W8_L300	6	8	300	39
Ni_Cant_W8_L400	6	8	400	39
Ni_Cant_W8_L500	6	8	500	39

According to these dimensions, expected displacement values can be computed assuming an elastic modulus value for the structural material. Figure 3.17 shows the expected voltage-displacement curves for electroplated nickel structures. The values are computed assuming elastic modulus of 200 GPa for nickel.

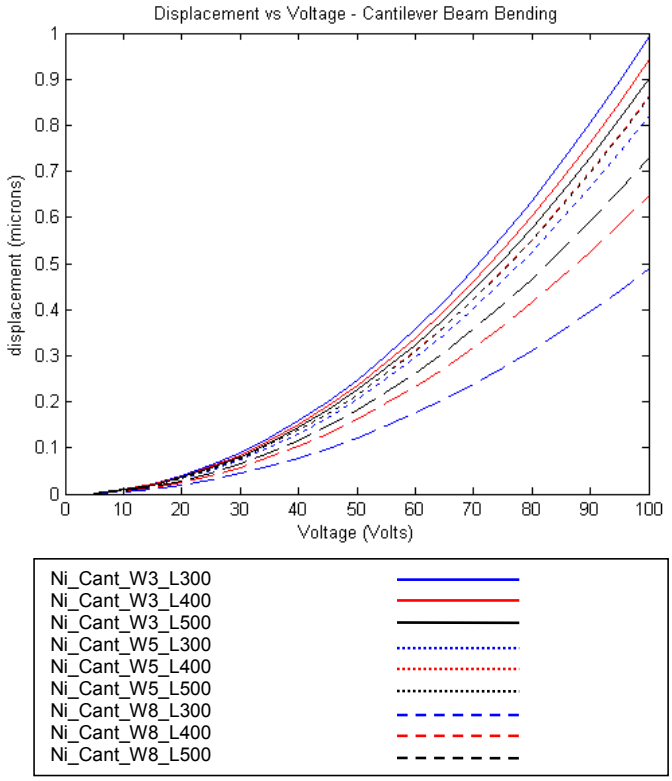

Figure 3. 17: Expected voltage-displacement curves for electroplated nickel samples

3.3.2 Double Clamped Beam Bending Test

The previous version of cantilever beam bending test device is improved with utilizing side suspensions and thinning the connection lever (Figure 3.13). However there is still an assumption of cantilever beam, which is in fact an approximation from one end fixed, one end guided beam. Moreover due to asymmetric structure, moveable comb still would tend to rotate at relatively high deflections. Making use of symmetry obviously eliminates these confusions. This is achieved by utilizing double clamped beam as test beam. Loading is again provided through a lever connecting the midpoint of the beam and the moveable comb (Figure 3.18).

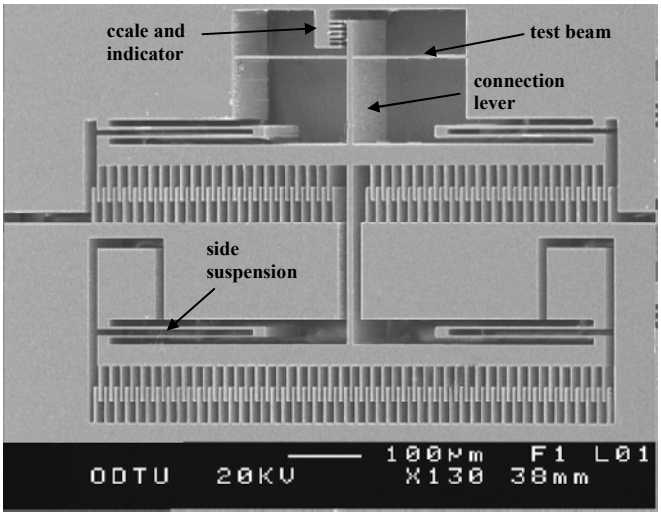

Figure 3. 18: Double clamped beam bending test device on deep reactive ion etched (111) Si

While solving major problems of the previous design, the new device introduces some new problems. The symmetry of the structure results in linear loading. However due to symmetry, non-fringing electric fields produce opposite in direction and equal in magnitude forces normal to the comb fingers, which results in unstable equilibrium in orthogonal direction. Therefore side stability of the device should be considered through the design. Another major problem caused by the structure is that the stiffness of the structure in the direction of motion considerably increases by utilizing a double clamped beam. Thus generation of

sufficient force becomes a problem. In order to solve the problem low stiffness beams (relatively long and thin) are to be tested. In addition to using low stiffness beams, generated electrostatic force should be increased. Thus the number of fingers should be considerably increased and the gap between adjacent combs should be decreased. Decrease in gap is constrained by fabrication processes. Minimum spacing between two fingers cannot be smaller than a value in order to ensure the satisfactory release of the structure through etching in case of electroplating. Increase in number of fingers on one moving electrode obviously increases the length of the comb drive, which in turn decreases stiffness of the moving comb. Thus, it is decided to use two sets of series connected lateral comb drives (Figure 3.18)

Opposite to the parallel plate actuators where the electrostatic force increases with the displacement of the moveable electrode, pull-in does not create a major problem in lateral comb drives in relatively small range of displacement. That is the displacements that can hardly be obtained using a parallel plate actuator, can easily be obtained by using a proper lateral comb drive. However in higher displacements pull-in may also create problems for lateral comb drives. As explained in Section 2.1, it is the fringing electric field that causes the lateral motion in lateral comb drive. The normal electric fields also contribute to electrostatic forces but they cancel out each other, remaining zero resultant force in normal direction. Although there is net zero force in orthogonal directions, this constitutes an unstable equilibrium. A compliant structure in orthogonal directions to the direction of motion may result in pull-in as displacement is increased. This is related to the side stability, which is characterized by the spring constant in transverse direction of the structure. That is the structure should have low stiffness in the direction of motion while being comparatively stiff in orthogonal directions [15]. Side suspensions in cantilever beam bending test are also used in double-clamped beam bending test device (Figure 3.18) not only to guide the moving electrodes, but also to increase the side stiffness of the structure.

Considering the stiffness of the side suspensions and the test beam itself, lumped model characterizing the device is shown in Figure 3.19.

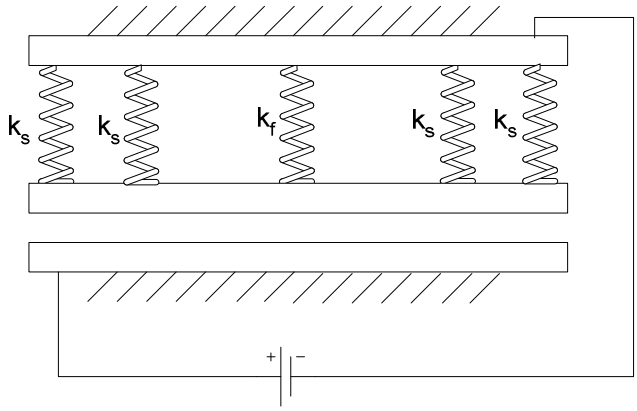

Figure 3. 19: Lumped model of double clamped beam bending test device

In Figure 3.19, k_f denotes spring constant of the specimen, k_s denotes the spring constant of the suspension springs. Since all four of the suspension springs are deflected at the same amount, they are modeled as parallel connected springs, which are also parallel connected to the specimen. Two series connected lateral comb actuators are modeled as a single actuator with finger number equal to the total finger number of both actuators. While it is illustrated as parallel plate actuator in Figure 3.19, the mathematical model is derived considering the actuator as lateral comb drive.

According to Figure 3.19, the spring constant of the structure in the direction of actuation is found to be

$$k = k_f + 4k_s \tag{3.18}$$

Spring constant for the midpoint of a double clamped beam loaded at midpoint with a concentrated force is given in equation (2.13). For a double clamped beam with thickness of t, width of w_f and length l_f, the spring constant is

$$k_f = \frac{16Etw_f^3}{l_f^3} \tag{3.19}$$

Spring constant for the side suspension spring is given in equation (3.16). Combining the equations (3.16), (3.18) and (3.19), the spring constant of the structure is found to be

$$k = \frac{Et(16w_f^3 l_s^3 + 2w_s^3 l_f^3)}{l_s^3 l_f^3} \tag{3.20}$$

Deflection of a spring is related to the linear spring constant through the equation

$$\delta = \frac{F}{k} \tag{3.21}$$

In the case of electrostatically actuated double clamped beam, F denotes the electrostatic force generated through a lateral comb drive, which is formulated as in equation (2.8). Combining equations (2.8), (3.20) and (3.21) results in the mathematical model for the double clamped beam, with concentrated electrostatic force acting at the midpoint.

$$\delta_{mid} = \frac{n\varepsilon_0 V^2}{gE} \cdot \frac{l_f^3 l_s^3}{(16w_f^3 l_s^3 + 2w_s^3 l_f^3)} \tag{3.22}$$

where n is the number of finger pairs in comb drive, g is the gap spacing between the adjacent comb, ε_0 is the free space permittivity, V is the applied voltage between the electrodes and E is the elastic modulus of the structural material.

Double clamped beam bending test devices are also fabricated in various dimensions. Similar criteria as in the design of the cantilever beam bending test devices are considered in designing the double clamped beam bending test devices. Figure 3.20 shows the design dimensions of the test device. The combinations of these dimensions are tabulated in Table 3.4 for DRIE (111) Si samples and in Table 3.5 for electroplated Ni samples. The tables also present the designations of the devices.

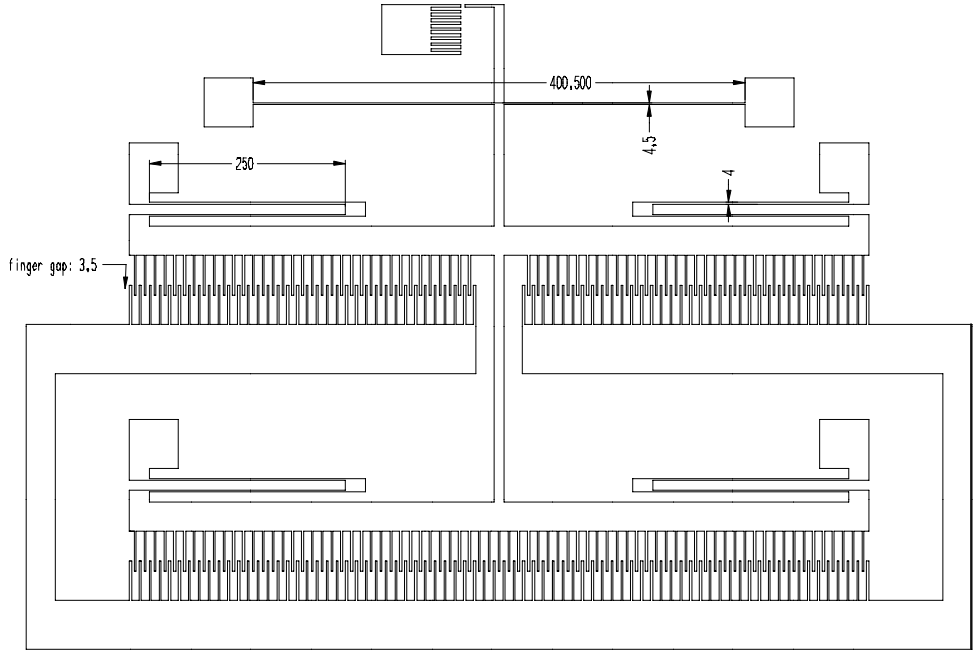

Figure 3. 20: Design dimensions of double clamped beam bending device

Table 3. 2: Double clamped beam bending test device designations for DRIE (111) Si samples

designation	finger gap (µm)	Double clamped beam width (µm)	Double clamped beam length (µm)	number of finger couples in comb drives
DRIE_FF_G3_W4_L400	3	4	400	123
DRIE_FF_G3_W4_L500	3	4	500	123
DRIE_FF_G3_W5_L400	3	5	400	123
DRIE_FF_G3_W5_L500	3	5	500	123
DRIE_FF_G5_W4_L400	5	4	400	95
DRIE_FF_G5_W4_L500	5	4	500	95
DRIE_FF_G5_W5_L400	5	5	400	95
DRIE_FF_G5_W5_L500	5	5	500	95

Table 3. 5: Double clamped beam bending test device designations for electroplated Ni samples

designation	finger gap(µm)	double clamped beam width (µm)	double clamped beam length (µm)	number of finger couples in comb drive
Ni_FF_W2_L400	4	2	400	143
Ni_FF_W2_L450	4	2	450	143
Ni_FF_W2_L500	4	2	500	143
Ni_FF_W3_L400	4	3	400	143
Ni_FF_W3_L450	4	3	450	143
Ni_FF_W3_L500	4	3	500	143

Figure 3.21 shows the expected voltage-displacement curves for electroplated nickel structures with the above dimensions. The values are computed assuming elastic modulus of 200 GPa for nickel.

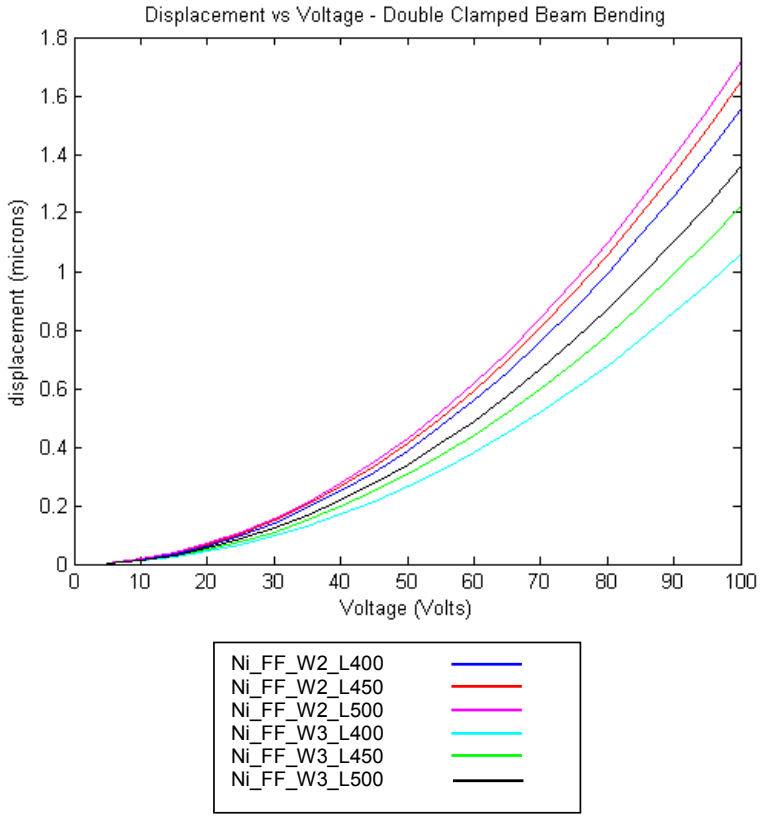

Figure 3. 21: Expected voltage-displacement curves for electroplated nickel samples

3.3.3 Cantilever Pull-in Test

Keeping that the pull-in is the instability of motion of an electrostatically actuated, spring suspended electrode in mind, principals defining the pull-in should be comprehended for further study. In order to investigate the pull-in, parallel plate capacitor with one electrode suspended is revisited (Figure 3.22).

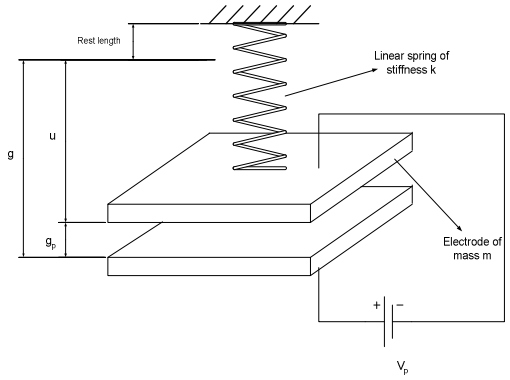

Figure 3. 22: Parallel plate capacitor

For the system above, considering the Newton's second law and defining the forces as damping force, restoring force due to linear spring and electrostatic force due to applied voltage; equation of motion is set to be

$$m\frac{d^2u}{dt^2} = F_e + F_d + F_s \tag{3.23}$$

Knowing that the damping force is related to the velocity and assuming quasi-static case for the testing purposes, inertial and damping effects can be neglected in the equation of motion. Thus the only forces that should provide static equilibrium are the spring force and the electrostatic force. Restoring force due to the linear spring can be written as

$$F_s = -ku \tag{3.24}$$

where u denotes the tension in the spring from the rest length of the spring. Electrostatic force for the parallel plate capacitor is given in equation (2.5) but restated here again for convenience.

$$F_e = \frac{\varepsilon A V^2}{2(g-u)^2} \tag{3.25}$$

where g is the initial gap and A is the area of the plate. Therefore the equation of motion becomes

$$ku = \frac{\varepsilon A V^2}{2(g-u)^2} \tag{3.26}$$

Non-dimensional parameters may be defined in order to investigate the behavior of the mass-spring system [1]. Defining

$$v = \frac{u}{g} \tag{3.27}$$

$$\lambda = \frac{\varepsilon A V^2}{2g^2} \cdot \frac{1}{kg} \tag{3.28}$$

where λ can be perceived as the ratio of electrostatic force to the restoring force and v as non-dimensional displacement of the moveable electrode [1], simplifies the solution. Inserting (3.27) and (3.28) into (3.26), equation relating λ to v can be found to be [1]

$$\lambda = v(1-v)^2 \tag{3.29}$$

Drawing the graph v versus λ clearly explains the pull-in phenomena (Figure 3.23).

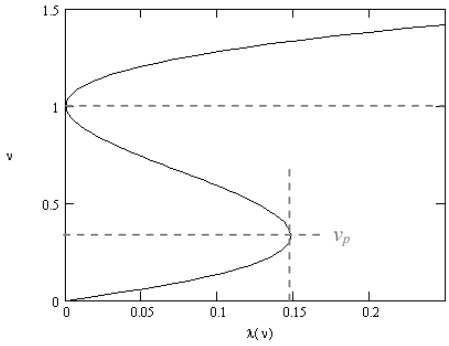

Figure 3. 23: v versus λ diagram

Figure 3.22 shows that the solutions above the horizontal dashed line are unphysical. Because any solution resulting in a v value of equal or greater than one means crashing of the suspended electrode into the fixed electrode. Also there is no meaningful solution for v at the right side of the vertical dashed line. Since λ is a non-dimensional parameter for the voltage applied, vertical dashed line determines the non-dimensional displacement up to pull-in v_p, which is equal to 1/3, and non dimensional pull-in voltage λ_p [1]. Therefore the pull-in gap for the spring-mass system is found to be [1]

$$g_p = \frac{2}{3} \cdot g \tag{3.30}$$

and the pull-in voltage is found to be [1]

$$V_p = \sqrt{\frac{8}{27} \cdot \frac{kg^3}{\varepsilon A}} \tag{3.31}$$

Cantilever pull-in test is based on the above explained phenomena. There are two types of cantilever pull-in tests. First type involves cantilevers at varying dimensions and fixed electrodes which behave like parallel plates (Figure 3.24).

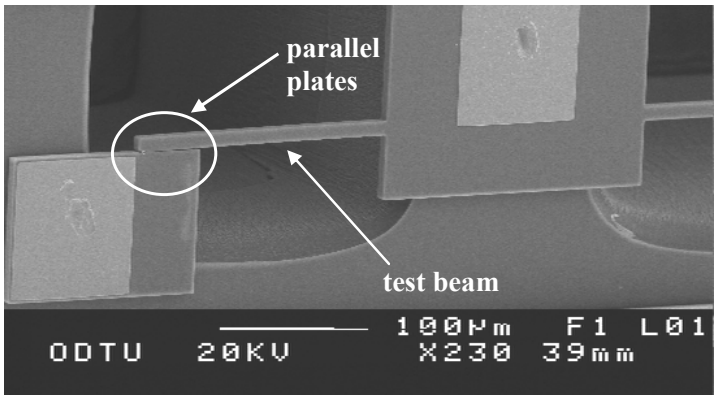

Figure 3. 24: Pull-in test structure on SOI. Note that the structure is in pull-in state

Loading state of the cantilever in Figure 2.24 up to pull-in can be defined as distributed load acting at the tip section of the cantilever (Figure 3.25a). If such a

distributed load is applied on the cantilever, the bending curve will be such as in Figure 3.25b. As the beam bends, gap between the electrodes vary along the tip section of the beam. Since the gap varies along the tip section, the distributed electrostatic force is no more uniform. This will create a neat deviation from the parallel plate assumption, especially at relatively large deflections.

(a) (b)

Figure 3. 25: (a) Loading state of the cantilever (b) Bending curve of the cantilever

While the test structures deviate from the parallel plate structure, still the voltage-stiffness relation derived for pull-in above is used in order to extract the mathematical model. Since the deflection is relatively small (around 1 μm up to pull-in) this approximation may hold true. Also derived model is then verified through the test results. For the test structure with the dimensions shown in Figure 3.26a, the lumped model is given in Figure 3.26b.

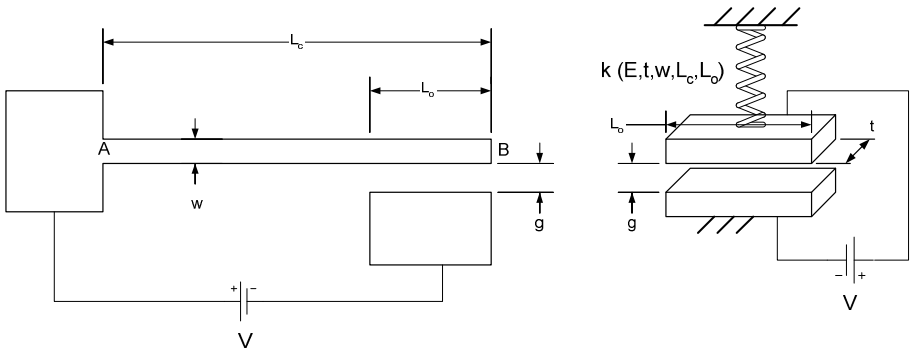

Structure thickness: t

(a) (b)

Figure 3. 26: Cantilever beam pull-in (a) device structure, (b) lumped model

While it is no more a parallel plate capacitor, spring constant at the tip point of the cantilever is used as the stiffness parameter in the model. Considering the bending curve; it is the first point that reaches the pull-in gap. Deflection and the spring constant at point B are computed using the moment-area method [16]. The derivation of the spring constant is given in Appendix B. As a result the linear spring constant is found to be

$$k_B = \frac{EI}{\frac{(L_c - L_o)^3}{6} + \frac{L_o(L_c - L_o)^2}{4} + \frac{L_o^2(4L_c - 3L_o)}{24}} \tag{3.32}$$

where I is the area moment of inertia of the beam about the axis of bending, which is equal to

$$I = \frac{tw^3}{12} \tag{3.33}$$

Setting the overlap area as

$$A = L_o t \tag{3.34}$$

and using the equation (3.31) and inserting (3.33) into (3.32), the expression for pull-in voltage is found to be

$$V_p = \sqrt{\frac{8}{27} \cdot \frac{Eg^3 w^3}{\varepsilon L_o \left(2(L_c - L_o)^3 + 3L_o(L_c - L_o)^2 + \frac{L_o^2(4L_c - 3L_o)}{2} \right)}} \tag{3.35}$$

Since the loading state of the above cantilever pull-in structure can not be clearly defined, it is improved in order to overcome the confusions. In the improved cantilever pull-in test device, the test beam is pulled in through a thin lever connecting the tip of the specimen to the moving electrode (Figure 3.27).

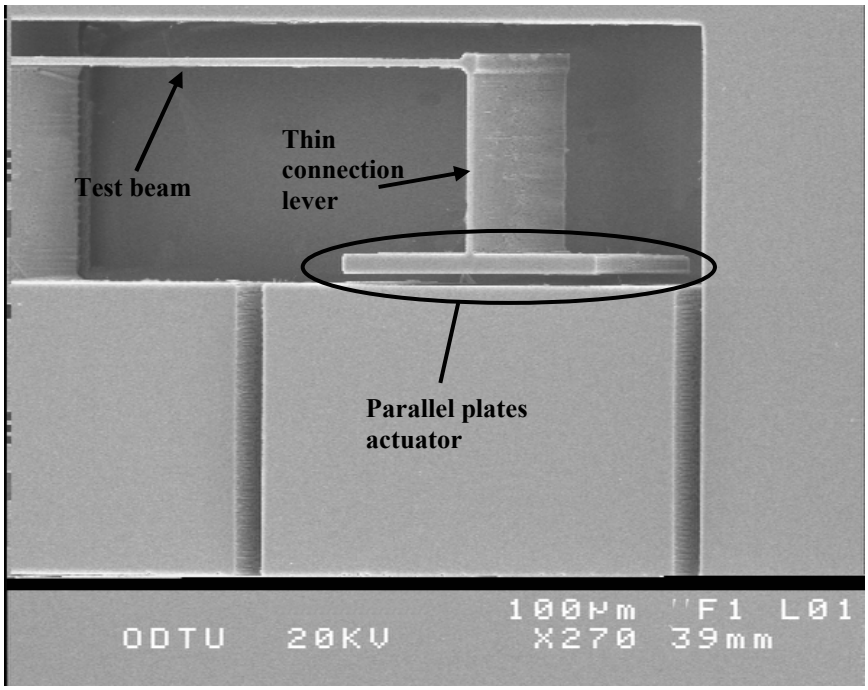

Figure 3. 27: Improved cantilever beam pull-in structure

This configuration clearly defines the linear spring constant that should be used in the mathematical model. The stiffness in the pull-in voltage relation is determined by the tip deflection of the cantilever loaded by a point force at the tip. For the cantilever with point load at the tip, the linear spring constant at the tip is given in equation (2.11). For a beam of width w, thickness of t, and length of L_c, the linear spring constant is found to be

$$k = \frac{Etw^3}{4L_c^{\ 3}} \tag{3.36}$$

Inserting the equations (4.34) and (4.36) into (3.31), the mathematical model for the improved pull-in structure is found to be

$$V_p = \sqrt{\frac{2}{27} \cdot \frac{Eg^3w^3}{\varepsilon L_c^{\ 3} L_o}} \tag{3.37}$$

It should be stated that the primitive version of the cantilever pull in device is fabricated on SOI, and the improved structures are fabricated using nickel

electroplating and deep reactive ion etching of (111) silicon. The primitive version of cantilever pull-in test device is designed prior to this study in METU. The device dimensions are shown in Figure 3.28. Dimension variations are tabulated in Table 3.6.

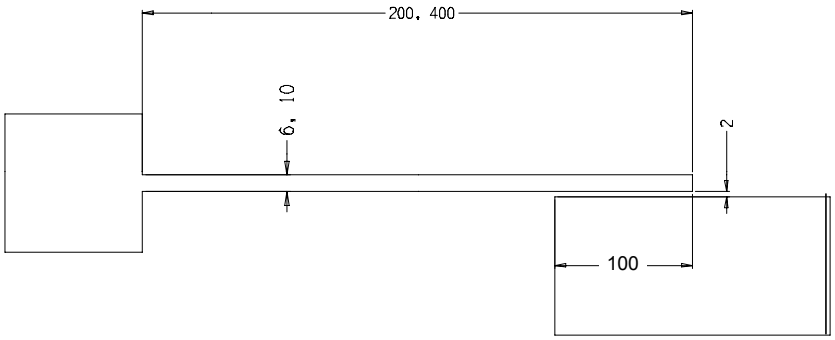

Figure 3. 28: Design dimensions of cantilever pull-in device

Table 3. 6: Cantilever pull-in test device designations

designation	cantilever beam width (µm)	cantilever beam length (µm)
SOI_PI_W6_L200	6	200
SOI_PI_W10_L200	10	200
SOI_PI_W6_L400	6	400
SOI_PI_W10_L400	10	400

The gap between the plates plays an important role in design of the cantilever beam pull-in test devices. Improved cantilever pull-in test devices are fabricated by nickel electroplating. Knowing that the electroplating results in slightly thicker structures, designed gap should be kept wide enough to allow the release of the structure. Additionally the width of the beam should not be kept too thick in order not to make the cantilever too stiff to actuate. Design dimensions of the improved cantilever pull-in test devices are shown in Figure3.29. Dimension variations for the DRIE (111) Si samples are tabulated in Table 3.7. Dimension variations for the electroplated Ni samples are tabulated in Table 3.8.

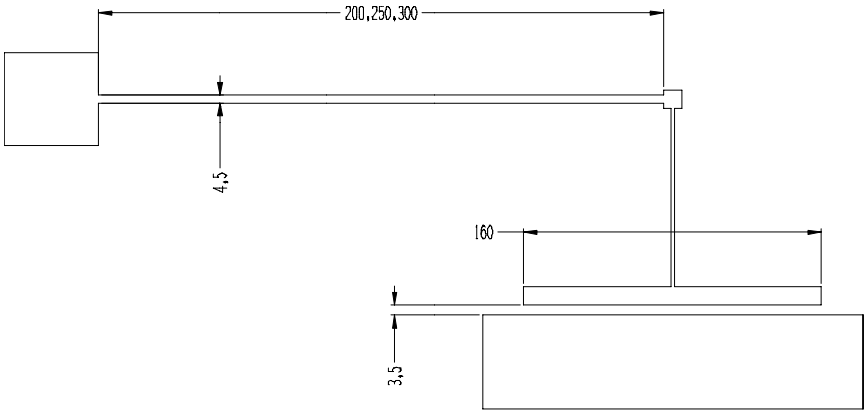

Figure 3. 29: Design dimensions of improved cantilever pull-in test device

Table 3. 7: Cantilever pull-in test device designations for DRIE (111) Si samples

designation	gap spacing between parallel plates (µm)	cantilever beam width (µm)	cantilever beam length (µm)	Expected pull-in voltage (V)
PullIn_G3_W4_L200	3	4	200	44
PullIn_G3_W4_L250	3	4	250	31
PullIn_G3_W4_L300	3	4	300	24
PullIn_G3_W5_L200	3	5	200	61
PullIn_G3_W5_L250	3	5	250	44
PullIn_G3_W5_L300	3	5	300	33
PullIn_G5_W4_L200	5	4	200	94
PullIn_G5_W4_L250	5	4	250	67
PullIn_G5_W4_L300	5	4	300	51
PullIn_G5_W5_L200	5	5	200	131
PullIn_G5_W5_L250	5	5	250	94
PullIn_G5_W5_L300	5	5	300	72

Table 3. 8: Cantilever pull-in test device designations for electroplated Ni samples

designation	gap spacing between parallel plates (µm)	cantilever beam width (µm)	cantilever beam length (µm)	Expected pull-in voltage (V)
Ni_PI_G4_W3_L200	4	3	200	48
Ni_PI_G4_W4_L200	4	4	200	73
Ni_PI_G6_W3_L200	6	3	200	87
Ni_PI_G6_W4_L200	6	4	200	134

Expected pull-in voltages for improved cantilever pull-in devices are computed assuming elastic modulus of 200 GPa for electroplated Ni and 169 GPa for (111) Si. The results are tabulated in Table 3.9.

3.4 Fabrication of Test Devices

At the beginning of this chapter it was mentioned that the devices are fabricated using three different methods: deep reactive ion etching of (111) silicon, electroplating nickel, and reactive ion etching of (100) silicon on insulator wafer. In Section 1.2, fabrication processes are briefly overviewed. In this section the details of the fabrication processes are described.

Basic processes are combined to derive combined processes that are commonly used in micro fabrication. One of these combined processes utilizes silicon on insulator (SOI) wafers. This approach utilizes silicon not only as a substrate material but also as the structural material. SOI wafers are composed of layers of device silicon at the top, oxide layer beneath and the handle silicon at the bottom. Device silicon layer can then be patterned through proper masking. The pattern is first replicated on photoresist spun on the uppermost layer. Using the photoresist as the mask, device silicon layer can be etched up to silicon oxide layer typically by reactive ion etching. In order to release the etched structure, silicon oxide layer is undercut by using wet etchants. Remaining is the overhanging single crystal silicon structure. The process is illustrated in Figure 3.30. One type of test devices in this study is fabricated on SOI wafers.

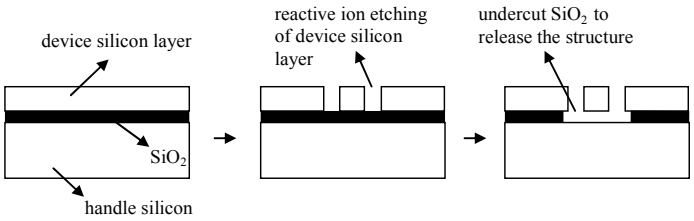

Figure 3. 30: Patterning silicon on insulator (SOI) wafer

Another common microfabrication process is metal electroplating, which is also used for fabrication of the test structures in this study. Metal electroplating is basically the process of electro-deposition of the desired metal through a mold of photoresist or any other sacrificial layer. In fabrication of the test structures used in this study, nickel is electroplated using a copper mold as sacrificial layer.

As a first step in fabrication of the structures by electroplating, a structured bi-layer of Ti/Au is deposited on silicon wafer, which will serve as an electrostatic shielding between the structure and the substrate. After then, a bi-layer of Cu/Ti is grown on the underlying layer. This layer is etched at the regions of Ti/Au layer up to Au layer (Figure 3.31a). The next step is the spinning of negative photoresist, and exposure using the anchor mask, leaving photoresist at anchor locations. Anchors are the regions, where the structures are fixed to the substrate. This process results in photoresist remaining at anchor locations, which in turn will serve as mold for copper electroplating (Figure 3.31b). After electroplating copper, photoresist is strip off. Remaining copper structure will now be the mold for nickel electroplating (Figure 3.31c). Same process of lithography and copper electroplating is repeated for producing the mold for the structure this time. The mold is filled with nickel by electroplating again. As the last step, the structure is released by etching copper layer completely (Figure 3.31d).

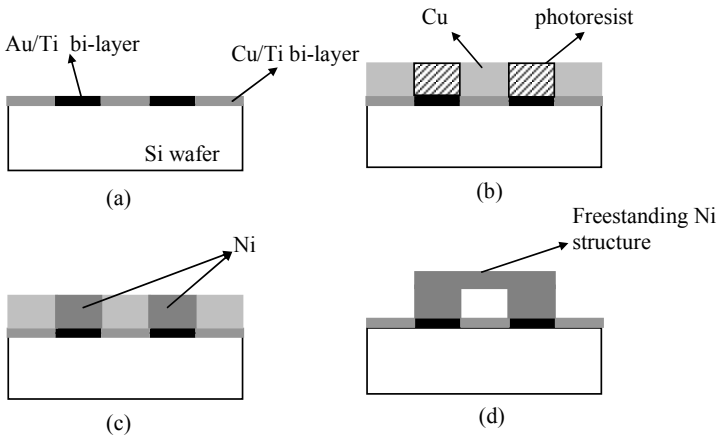

Figure 3. 31: Nickel electroplating

Third type of process used for fabrication of the devices is deep reactive ion etching (DRIE). Microfabrication processes generally limit the aspect ratio of the structures. That is the fabrication of thick and narrow structures is generally hindered by the processes. However DRIE enables production of high aspect ratio structures. The method is basically the reactive ion etching of the substrate step by step, by application of alternating cycles of reactive ion etching and polymer deposition (Figure 3.32).

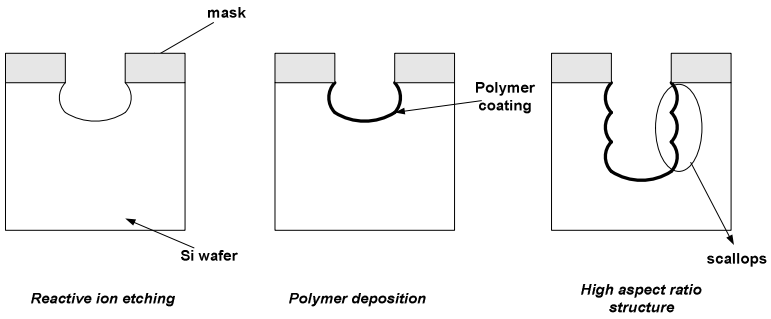

Figure 3. 32: Alternating cycle of reactive ion etching and polymer deposition

While the step by step etching results in scalloping (Figure 3.32), the polymer coating following the etching provides the near vertical side walls. The mask used in this process can be either photoresist or silicon oxide. However it should be noted that since reactive ion etching suffers selectivity, the mask may also be etched in advance. Using DRIE, through holes with high aspect ratios may be fabricated on wafers. In fabrication of high aspect ratio silicon structures on glass substrates, as the first step, the glass wafer is etched to form a cavity. Next, the glass wafer is fusion bonded to the silicon wafer. The silicon wafer is deep reactive ion etched up to the cavity, releasing the structure (Figure 3.33).

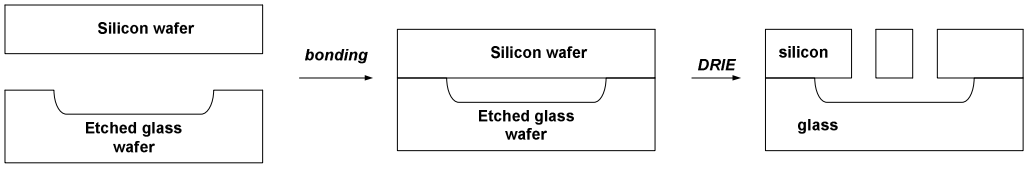

Figure 3. 33: Silicon-glass bonding and DRIE

CHAPTER 4

PASSIVE TESTS AND TEST RESULTS

This chapter includes the testing of the passive devices. Also the results are discussed in this chapter. These passive testing devices are explained in Section 3.1 in details.

Section 4.1 explains test setup and the testing procedure for the passive test devices. Test results for both of the devices are given in Section 4.2. Section 4.3 discusses the test results as a conclusion for the passive tests.

4.1 Test Setup and Testing Procedure

For the testing of passive test devices, namely the bent beam strain sensor and the cantilevers for stress gradient measurement, there is no need for actuation. This eliminates the need for a special test set up. Testing of the passive devices only require optical measurements of displacements.

It should be recalled from Section 3.1 that the deflection of the bent beam strain sensor is in-plane, whereas the deflection of the cantilevers for stress gradient measurement is out-of-plane. This necessitates the use two different optical inspection systems. Optical microscopy is used to inspect the bent beam strain sensors. Recall that the vernier scales attached at the apexes of the bent beams facilitate the reading of the displacements. On the other hand, optical profiler is used to inspect the cantilevers for stress gradient measurement. Optical profiler

allows the inspector to measure the out-of-plane deflections and detect the surface profile of the structure. By this way, the deflection curves of the cantilevers are obtained. In addition to these optical means, the results are supported with the SEM pictures of the devices.

After describing the testing procedure test results are presented in the following section.

4.2 Test Results

As mentioned before in previous chapters deep reactive ion etched (111) silicon samples and electroplated nickel samples are examined to determine the residual stress in structures. In micro systems, the residual stresses commonly occur after the release of thin film structures deposited on sacrificial layers. In accordance with that, deep reactive ion etching practically yields zero or negligible residual stresses. This is also verified by the passive test devices on the deep reactive ion etched (111) silicon structure. Thus the results for the deep reactive ion etched structures are not discussed here. Results of the electroplated nickel devices are presented in the following subsection.

4.2.1 Testing of Electroplated Nickel Samples

In this section the results of the inspection of the bent beam strain sensor and the cantilevers for stress gradient measurement of electroplated nickel are presented. It is observed that the bent beams do not deflect in-plane, but buckle out-of-plane. The reasons are discussed in the following subsection. Additionally the maximum residual stress is computed using the cantilevers for stress gradient measurement.

4.2.1.1 Bent Beam Strain Sensor

It is mentioned in Section 4.1 that the bent beam strain sensors are investigated by optical microscopy. Figure 4.1 shows the snapshot of the bent beam with 15^{o} bend angle and 6 μm thick beam. At first glance, it can be concluded that there is no

internal stress due to aligned vernier scales (Figure 4.1). However investigating the snapshots, it can be seen that the surface of the structure does not lie on the same focal plane, which indicates that buckling exists out-of-plane. This is possibly due to increased stiffness of the structure resulting from the thickening of the beam during electroplating. However it may also originate from the existence of stress gradient. This should be checked by inspecting the cantilevers for stress gradient measurement.

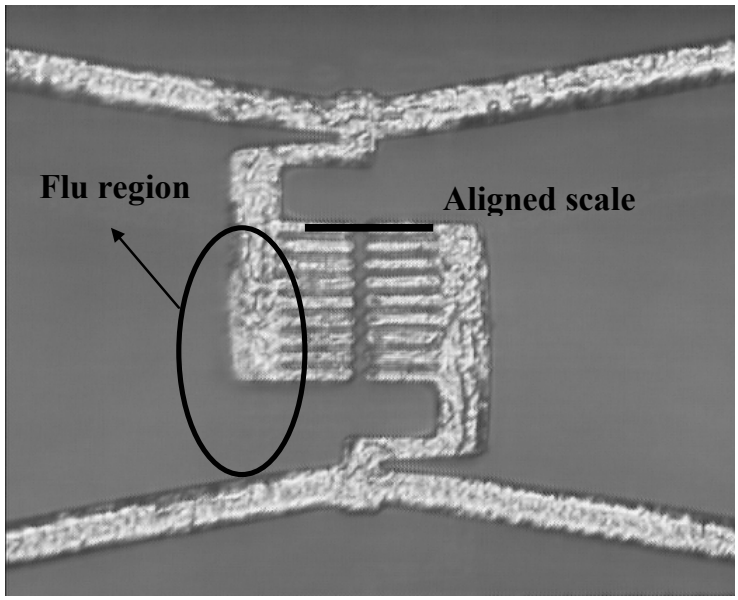

Figure 4. 1: Snapshot of the electroplated nickel sample

While only the snapshot of the sample with 15^{o} bend angle and 6 μm thick beam, is given, above is the case for each sample.

4.2.1.2 Cantilevers for Stress Gradient Measurement

In order to determine whether the bent beams buckle due to stress gradient or not, the cantilevers shown in Figure 4.2a are examined. Tips of the cantilevers at different lengths are deflected downwards (Figure 4.2b) due to the stress gradient effect. It should be recalled that the tip deflection of the cantilevers exposed to stress gradient, is related to the maximum stress across the beam with the equations (3.4) and (3.5). Tip deflection in that case, is the difference between the

focal distance of the tip and the root of the beam. This can be measured by using an optical profiler as mentioned in Section 4.1. The profiler detects the focal planes by scanning the structure from top to bottom. Thus deflection curves of the beams can be obtained.

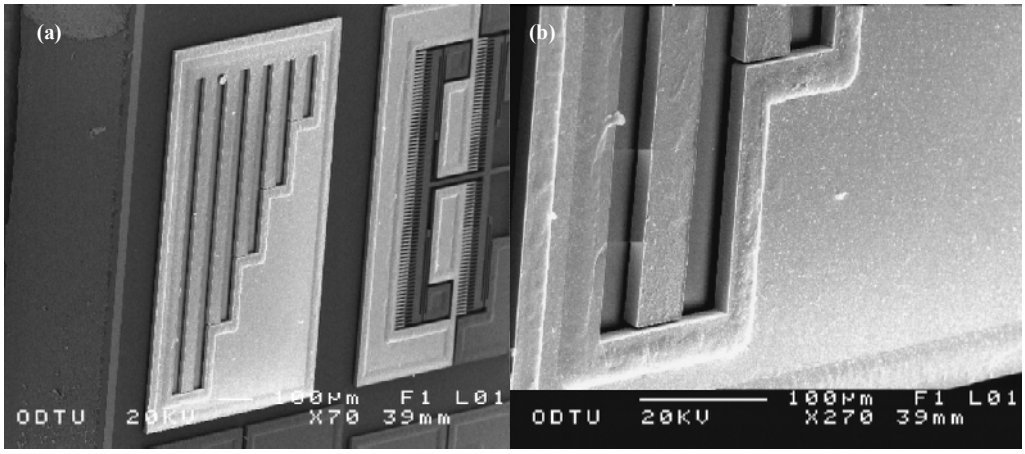

Figure 4. 2: (a) Cantilevers for evaluation of residual stress (b) Tip deflection of the 1000 µm beam

The lengths of the beams vary from 200 µm to 1000 µm. While the deflection curve of the 200 µm beam could not be detected successfully, the deflection curves for the other beams are obtained. The results are shown in Figure 4.3.

For the cantilever beams, whose deflection curves are given in Figure 4.3, maximum residual stress is calculated to be 8 MPa using the equations (3.4) and (3.5). Practically, this much of residual stress would not effect the functioning of the other test devices. Thus the testing of the electroplated nickel structures is validated.

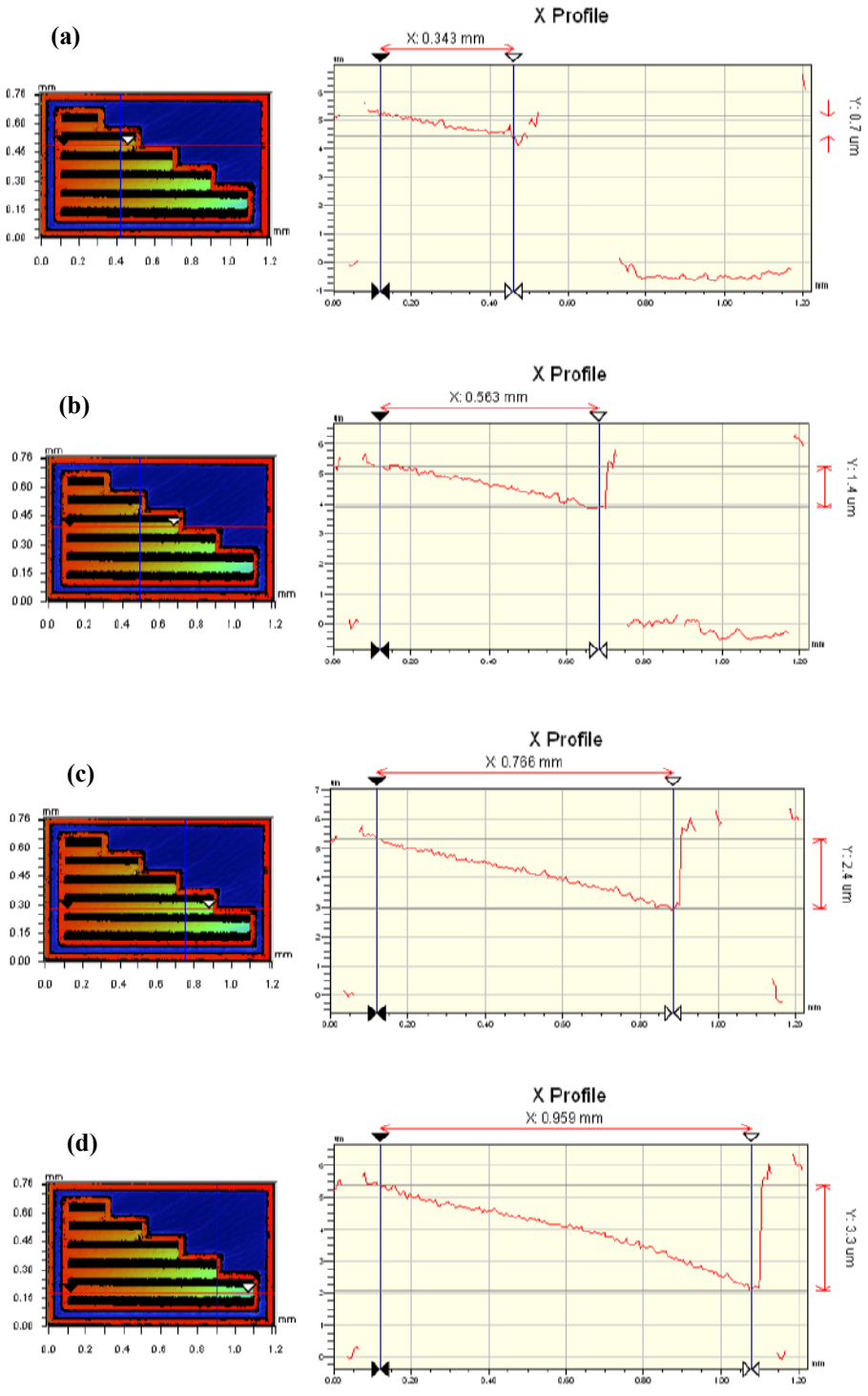

Figure 4. 3: Deflection curve of (a) 400 µm beam (b) 600 µm beam (c) 800 µm beam (d) 1000 µm beam of electroplated nickel

4.3 Conclusion of Passive Tests

As deep reactive ion etching does not involve high temperature deposition processes and release of sacrificial layers, it essentially yields zero residual strains. This is also verified by the bent beam residual strain sensors. However, bent beam residual strain sensors could not be used in order to determine the residual straining in the electroplated nickel samples. Because of the increased stiffness in direction of the apex movement, due to bulging of the specimen, every bent beam strain sensor buckled out of plane. However, it could be possible to extract information about the residual stresses in the structures using the cantilever beams for determination of residual stress. Tip deflections of the cantilever beams are related to the maximum residual stress in the structures. As a result residual stress of 8 MPa is computed for the structures, which can be ignored.

CHAPTER 5

DYNAMIC TESTS AND TEST RESULTS

Most of the MEMS devices are exposed to cyclic loadings during its lifetime. These cyclic loadings result in different levels of stresses at critical locations of the device of subject, which affects the endurance time of the device. Therefore the fatigue behavior of the materials, used in the fabrication of the MEMS structures, should be extracted in order to verify the designs. Test devices for dynamic characterization of the materials are explained in Section 3.2. This chapter includes the testing of cantilever beam bending devices for fatigue characterization explained in Section 3.2.

Section 5.1 describes the test set up and the testing procedure. Unfortunately no functioning device could be obtained after fabrication. The reasons are discussed in Section 5.2. Finally, Section 5.3 summarizes the conclusions for the dynamic tests.

5.1 Test Setup and Testing Procedure

The devices explained in Section 3.2 are the same in general. Thus the testing should be done in the same manner. Hence, the devices are examined together throughout the chapter.

Before starting the tests, voltage required to pull-in the structures should be determined. Note that since the stiffness of each sample is different, pull-in

voltage should be determined for each of the devices. This is to be done using a probe station. The setup for determining the pull-in voltage is shown in Figure 5.1.

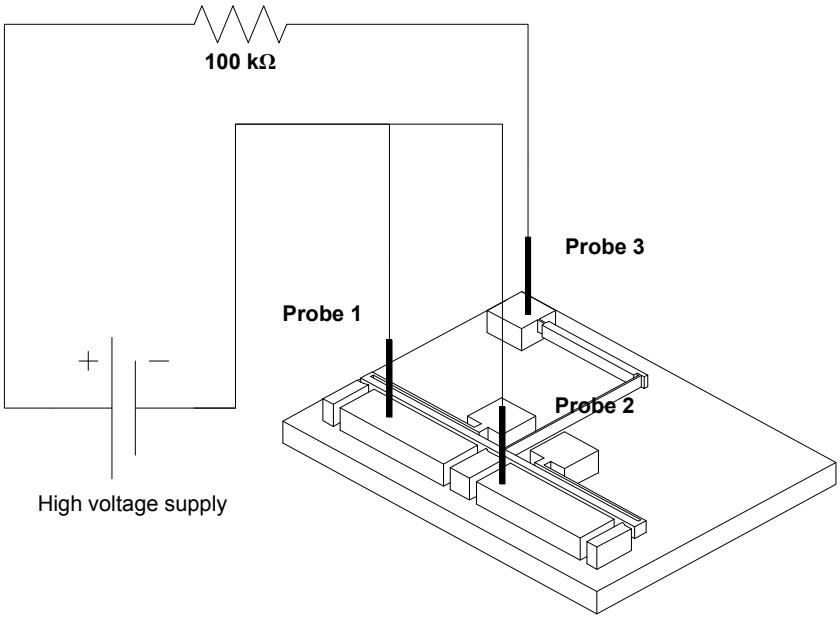

Figure 5. 1: Setup for determination pull-in voltage.

Note that 100 kΩ resistance is series connected to probe 3 in order to protect the elements in case of a brake down in pull-in. It should be recalled that there are bumpers located in front of the moveable electrode to prevent stiction, thus the current flow, in case of pull-in. However 100 kΩ is still used as a measure.

After determination of pull-in voltages the devices are ready for testing. Recall that the pull-in voltages determined beforehand are used for actuation of the structure in cyclic manner. The circuits proposed for testing both types of fatigue test devices (Figure 5.2) are the same with minor differences, and are the modified versions of the circuit used by Larsen [11]. Low voltage signal generator in the circuit generates a square wave altering between 0 voltage and maximum voltage for testing the previous version, and generates a square wave altering between

minimum and maximum voltage values yielding a zero mean. For the second set up, it is important to ground the anchor of the beam, not the fixed electrodes. The voltage amplitude generated and the ratio of the transformer should be determined after measuring the pull in voltage for the structure.

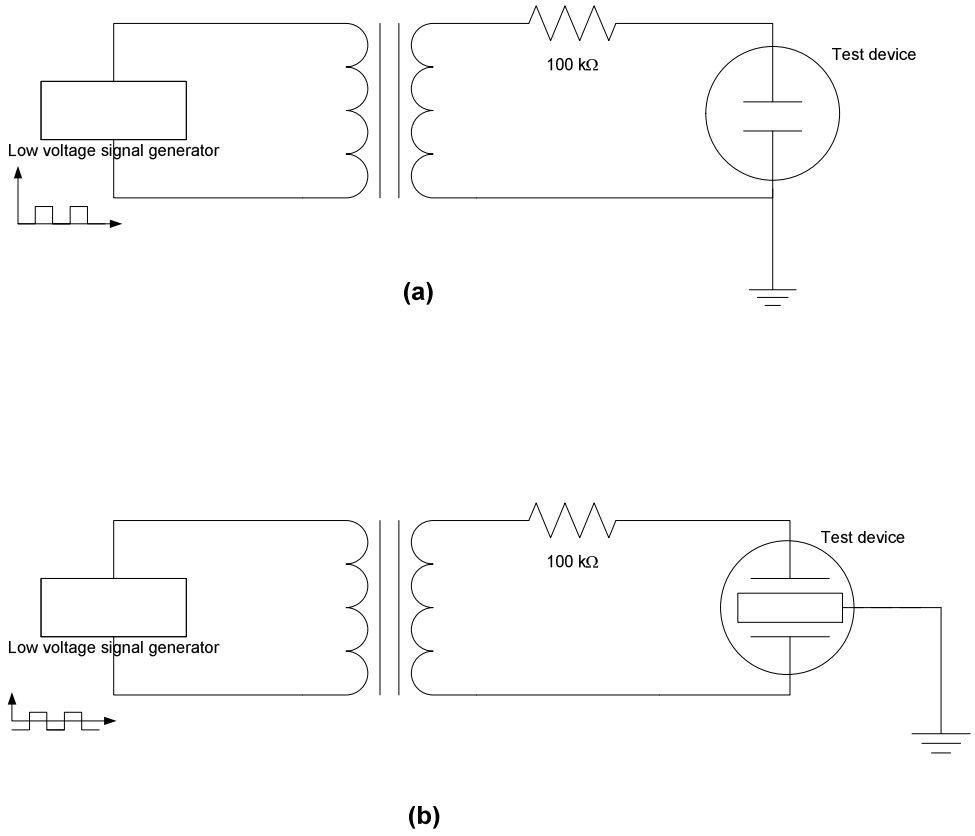

Figure 5. 2: Fatigue testing circuit (a) for previous version (b) for improved version of the device

5.2 Test Results

As mentioned before, the fatigue test devices are fabricated by nickel electroplating and deep reactive ion etching of (111) silicon. It was mentioned that none of the fabricated devices could be tested. The reasons and possible measures are discussed in this section.

5.2.1 Testing of DRIE (111) Silicon Samples

While the fatigue of single crystal silicon is a new subject [25], and there are not so much evidence explaining the failure mechanisms of single crystal silicon [26], it is aimed to conduct the fatigue test on silicon to observe the test setup. However it could not be possible to obtain any surviving sample from the DRIE run.

DRIE process flow is briefly described in Section 3.4 and illustrated in Figure 3.31. After the process, the polymer layer should be removed by wet etching in order to obtain bare silicon structures. However the etchant for the removal of the polymer layer is very active and the etch environment is very harsh. The anchors with small surface areas could not survive in this harsh environment (Figure 5.3). Hence the fatigue test devices are also wasted in DRIE.

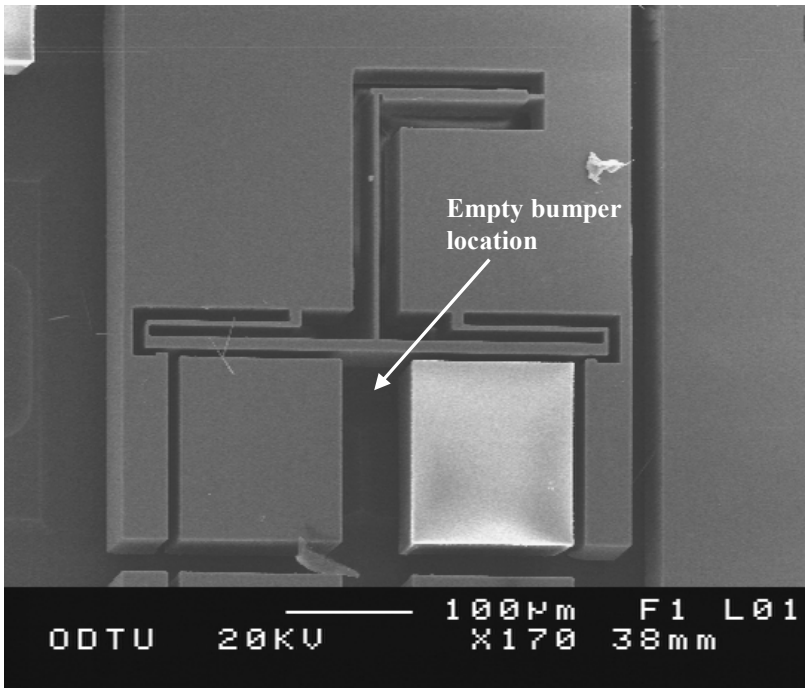

Figure 5. 3: Stripped away bumper of fatigue test device on deep reactive ion etched (111) Si

Modifying the structure by increasing the bumper areas may possibly solve the problem stated above.

5.2.2 Testing of Electroplated Nickel Samples

While the fatigue devices of electroplated nickel are successfully released, it is also not possible to test the nickel structures due to serious changes in design dimensions. Revisiting the photolithography explained in Section 1.2, it is mentioned that the photoresist mold is hardened after spinning on the silicon substrate. The photoresist used in photolithography shrinks non-uniformly during this baking operation, resulting in larger mold for electroplating. As a result the dimensions of the electroplated nickel devices expand considerably. While the expansion of the beam section does not hinder the operation of the device, the expansion at the actuation sites means the blocking of the gap between the electrodes.

Remember that the pull in gap is 2/3 of the initial gap, that is the pull in occurs after the moveable electrode displaces at an amount of 1/3 of the initial gap. Therefore the bumper should allow the electrode to move at the specified amount. The design dimension shown in Figure 5.4 satisfies this condition. Device dimensions are also given in Section 3.2

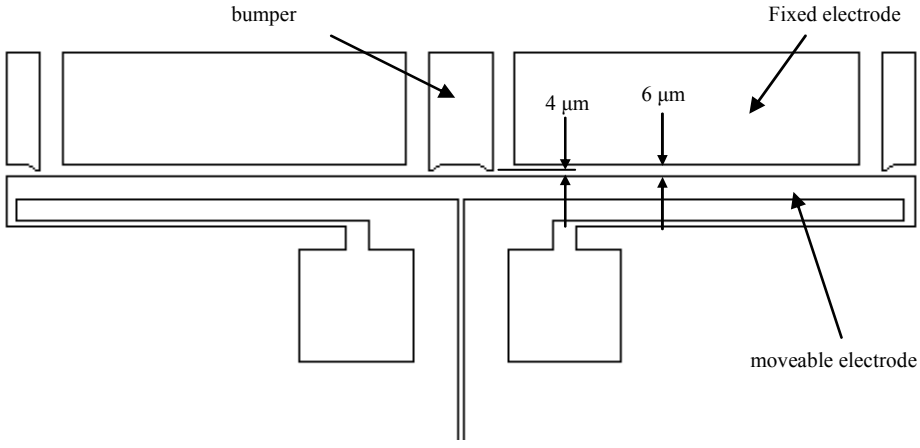

Figure 5. 4: Design dimensions of the bumper gap and the electrode gap

The non-uniform bulging of the structure dimensions results in the higher reduction of the gap spacing between the bumper and the moveable electrode than the reduction of the gap spacing between the fixed electrode and the moveable electrode, hindering the pull in of the moveable electrode. Resulting case is illustrated in Figure 5.5.

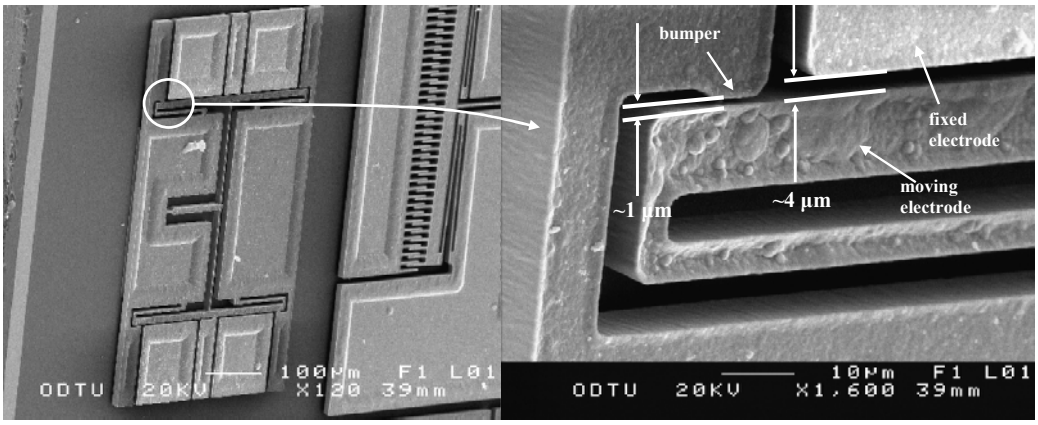

Figure 5. 5: Actual dimensions of the bumper gap and the electrode gap

Although the pull in of the moving electrode is not possible, it is still possible to deflect the structure up to the bumper by tuning the applied voltage. Maximum von Mises stresses calculated using finite element analysis are 120 MPa for 20 µm test beam, 150 MPa for 15 µm test beam and 200 MPa for 10 µm test beam, in this case. Knowing that no fatigue failure is observed for test beams with calculated maximum von Mises stress of 2.1 GPa [11] it becomes nonsense to conduct the tests on the electroplated nickel samples. Designed gap should be kept larger in order to work out this problem.

5.3 Conclusion of Dynamic Tests

Since it could not be possible to obtain a functioning device, dynamic testing of the samples could not be achieved. However the testing procedure and the test set up are defined in order to provide a background for future work on the subject.

Considering the electroplating, in order to obtain a functioning device, the bumper and the electrode gaps may be modified. Increasing the electrode gap, while keeping the bumper gap constant, obviously solves the problem. However increasing the electrode gap considerably increases the pull-in voltage, which may create problems during testing. On the other hand, if deep reactive ion etching is considered, it can be concluded that the bumpers should be redesigned to increase the anchor area of the bumper. Thus the bumpers can survive after etching.

Additionally, in order to extract the fatigue behavior of the material completely, the tests should be conducted for various stress levels. In order to achieve this, beam thickness, beam length, and the bumper gap should be properly adjusted.

CHAPTER 6

STATIC TESTS AND TEST RESULTS

This chapter includes the testing and of the static test devices and test results. Additionally, a novel method for measurement of micron level deflections and dimensions, utilizing image processing is presented in this chapter. Also finite element analyses of the devices are presented here in order to verify the test results.

Section 6.1 overviews the test setup and the testing procedure. Section 6.2 describes the method used for dimensional measurement and measurement of displacements. The computer script written for this purpose is explained in details. Section 6.3 includes the results of the tests conducted on cantilever beam bending devices, double clamped beam bending devices, and cantilever pull-in devices. Recalling that different fabrication methods are used for producing the test devices, test results are presented in different subsections for deep reactive ion etched (111) silicon samples, electroplated nickel samples and (100) silicon on insulator samples. Section 6.4 presents finite element analysis results for the devices. Also, finite element analysis results and the test results are compared in this section. General conclusions on the static tests are presented in Section 6.5.

6.1 Test Setup and Testing Procedure

The static tests are all conducted on KarlSuss PM5 probe station with a CCD camera mounted. Voltage required for electrostatic actuation is applied to the

devices through the probes penetrated into the electrode anchors on the devices (Figure 6.1). Voltage applied is limited with the pull-in for all devices. Considering the side pull-in in cantilever beam bending test devices, maximum voltage applied varies around 100 Volts. In this respect, high voltage power supply is used in order to apply the required voltage. The 100 kΩ resistance is required in order to prevent the failure of the elements in case of high current flow, which occurs at pull-in.

Although the setup for both bending and pull-in tests are the same, testing procedure quite differs. Cantilever beam bending and double clamped beam bending requires quasi-static loading. In order to satisfy the quasi-static loading the voltage is applied stepwise with small increments, quantitatively 5 volts for the bending tests. While application of voltage with increments lower than 5 volts results in loss of precision, application of voltage with increments higher than 5 volts generally results in oscillation around the equilibrium state. Application of voltage is continued up to side pull in of the structure. At each step snapshot of the displaced beam is captured. These snapshots are processed afterwards in order to determine the deflection at each voltage level. The data is then used to determine the voltage-displacement curve. Processing of the images is explained in details in the following section.

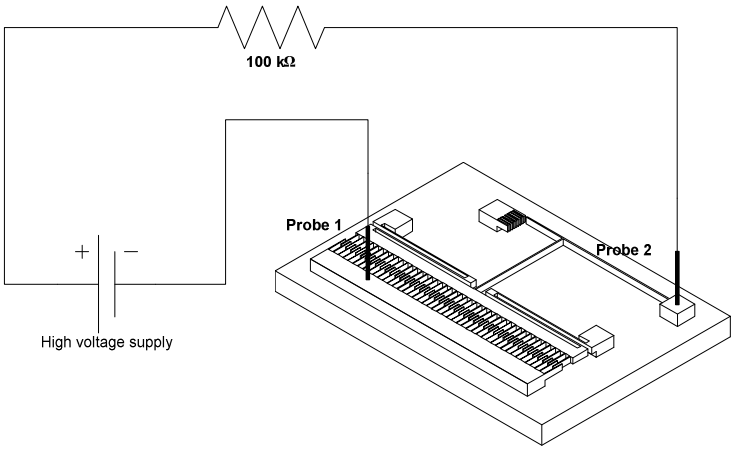

Figure 6. 1: Test set up

While it is required to gather displacement data at different voltage amplitudes in bending tests, only the pull in voltage is required to be determined in cantilever pull in tests. Pull in voltage for most of the samples are measured to be around 40-50 Volts. This necessitates the use of high voltage supply again. The voltage is finely increased up to pull in in order to precisely determine the pull in voltage. However the precision is limited by the high voltage supply since it provides resolution of 1 Volt.

6.2 MEMSURE: MATLAB Scripts for Micron Level Measurements

As mentioned in the previous chapters, the device dimensions considerably change during the fabrication processes involved, namely the nickel electroplating and deep reactive ion etching of (111) silicon. Device dimensions usually expand in nickel electroplating process. This is mainly due to shrink of the photoresist during hardening, yielding a larger mold, which results in bulging of structures. On the other hand DRIE may result in thinner structures. As explained in first chapter DRIE slightly suffers selectivity, which may result in the etching of the photoresist mask on sides. Hence the silicon lying beneath the photoresist layer is etched more. Also possible non-uniform etching of the photoresist layer yields non-uniform structure dimensions, which constitutes the major error source in evaluating the elastic modulus. Although the widths of the structures considerably change, the length of the structures can be assumed to remain the same without yielding a significant error. Besides, the thickness of the structures is generally well defined by the fabrication technique involved. Therefore, it is the width of the structures that deviates from the design dimension. This necessitates the dimensioning of the structures before testing. While having deficiencies, this is achieved through a computer script written on MATLAB 7.0 using the image processing toolbox of the software. The same algorithm, with small modifications, is also used for measurement of the displacements in static tests.

In order to measure the micron level dimensions visually, snapshots of the microstructures are captured under microscope with specified magnification. These snapshots should be processed in order to determine the micro displacements or dimensions. The scripts written specifically for achieving the thesis objectives mainly consist of three separate modules, one for calibration of the images, one for measuring displacements by processing successive images, and the other for dimensioning the microstructures. The latter two modules utilize the same algorithm.

The scripts are evolved in two versions. In the primitive version of the scripts, the colored bitmap image of the devices are captured and then processed with high level user interaction. As an example consider the image in Figure 6.2. The image is the snapshot of the vernier scale and the tip of cantilever beam of 5 μm width on the cantilever beam bending test device fabricated by DRIE, with resolution of 480 pixels by 640 pixels. Note that the structure is corrupted during the fabrication, yielding deviation from design dimensions. Thus it is critical to measure the dimensions after fabrication. Before going further, the pixel width in microns should be determined. This requires a calibration operation.

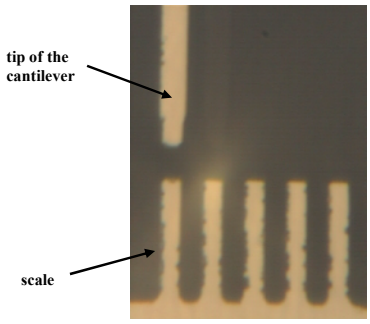

Figure 6. 2: Colored bitmap image of the vernier scale and the tip of the cantilever beam

While the dimensions are severely altered during fabrication, the distance between the central axes of the successive fingers of the scale remains the same. Otherwise results in complete shift of the structure on the wafer, which is not the case. Referring this distance, calibration can be done. For this purpose two points are

selected on the axis of one of the fingers (Figure 6.3a). As the next step, a third point is selected on the axis of the neighboring finger (Figure 6.3b). A line is fitted to the first two points and the nearest distance of the third point to this line is computed analytically (Figure 6.3c). The result is the pixel distance between the axes of the successive fingers. Knowing this distance in microns, the width of a single pixel is computed.

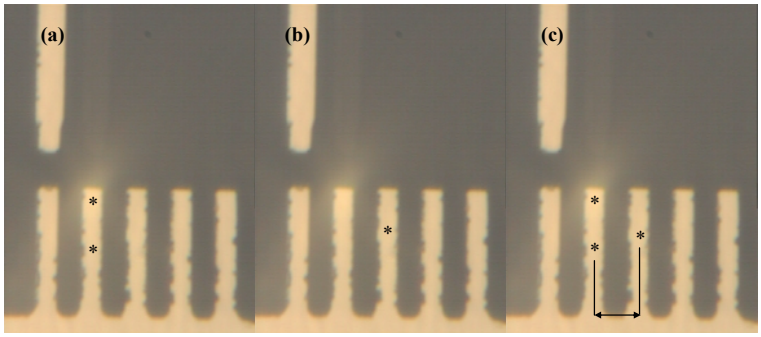

Figure 6. 3: Computation of pixel width in microns

The major error in this approach is that it is unknown that how accurate the selected points lay on the central axis of the finger. After calibrating the image, width of the cantilever beam is computed on the same image, again using the same method. However this time, selected points lay on the sides of the beam (Figure 6.4).

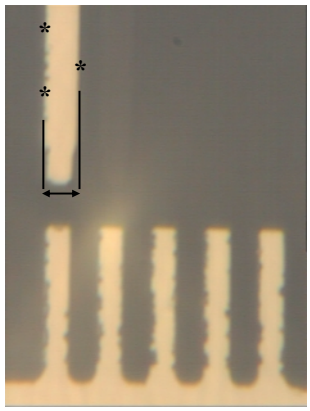

Figure 6. 4: Measuring the width of the beam

Again it is unknown that how accurate the selected points lay on the edge of the beam. While it is focused on the structure surface, there is still a gradient from the structure to the gradient. This "band" of edge is obviously an error source. The readings of 20 measurements are tabulated below.

Table 6. 3: Readings of 20 measurements of beam width

#	beam width	#	beam width
1	4.441	**11**	4.469
2	4.512	**12**	4.553
3	4.499	**13**	4.666
4	4.591	**14**	4.568
5	4.553	**15**	4.534
6	4.619	**16**	4.513
7	4.551	**17**	4.561
8	4.436	**18**	4.518
9	4.681	**19**	4.723
10	4.500	**20**	4.610

The frequency distribution and the percent cumulative frequency is shown in Figure 6.5. It can be concluded from Figure 6.5a that the distribution is normal. However, since the sample size is low (practically smaller than 30) Student's t distribution is fitted to data. Therefore the width of the beam is read to be 4.546 ± 0.160 μm with 0.95 confidence level. And the pixel width is computed to be 0.078 μm. While having deficiencies, the script still yields precise results. However it should be improved not only to compensate for its deficiencies, but also to decrease the high processing time due to high level user interaction.

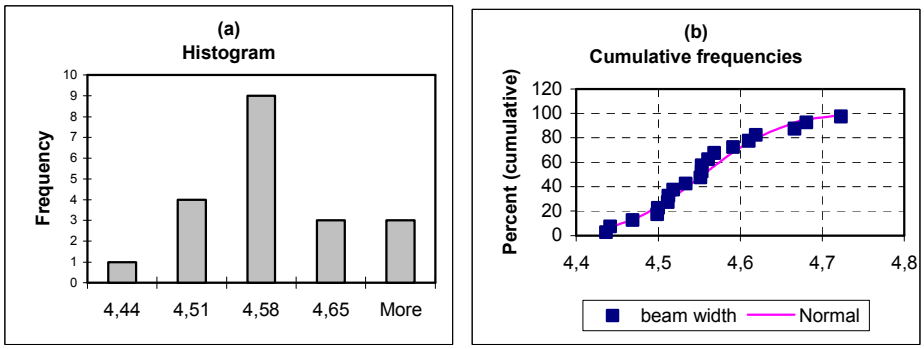

Figure 6. 5: (a) Histogram of readings (b) Percent cumulative frequencies of readings

In the improved version of the scripts, different from the primitive version, color bitmap images are converted to grayscale bitmap images that are to be processed. This intensity image is then used for determining the threshold value using Otsu's method [23] in order to convert the intensity image to binary image. This thresholding removes the confusion due to intensity gradient at the unsharp edges. But a post-processing may be required for justification of the threshold value. In order to calibrate the image, the binary image is thinned to convert the areas to lines. The resulting skeleton image is the approximation to the medial axes of the pattern. It should be recalled that the calibration is done on the basis that the distance between the central axes of the adjacent scale fingers remain the same after fabrication. After generating the skeleton of the base image, lines are fitted to axes of two adjacent fingers selected. This is achieved by defining a region of interest enclosing the finger axis (Figure 6.6d). Then the image is filtered using the region selected, setting the pixel values to zero out of the selected region of interest. The remaining image only contains the skeleton of the selected finger (Figure 6.6e). As the next step, the radon transform [24] of the filtered binary image is computed. Radon transform computes the projection of the intensities along specified directions. If the whole image is transformed by scanning along each direction (0 to 179 degrees), the peak obtained in the transform array absolutely indicates the occurrence of a line. Note that since the image is filtered with the region of interest there is only one line that can be detected using radon transform. The same is done for the adjacent finger, but this time radon transform

is computed only along the direction parallel to the line fitted for the neighboring finger, in order to ensure the parallelism of both lines. The resulting lines are shown in Figure 6.6f. The distance between two parallel lines in pixels is compared with its micron equivalent, yielding the pixel width in microns.

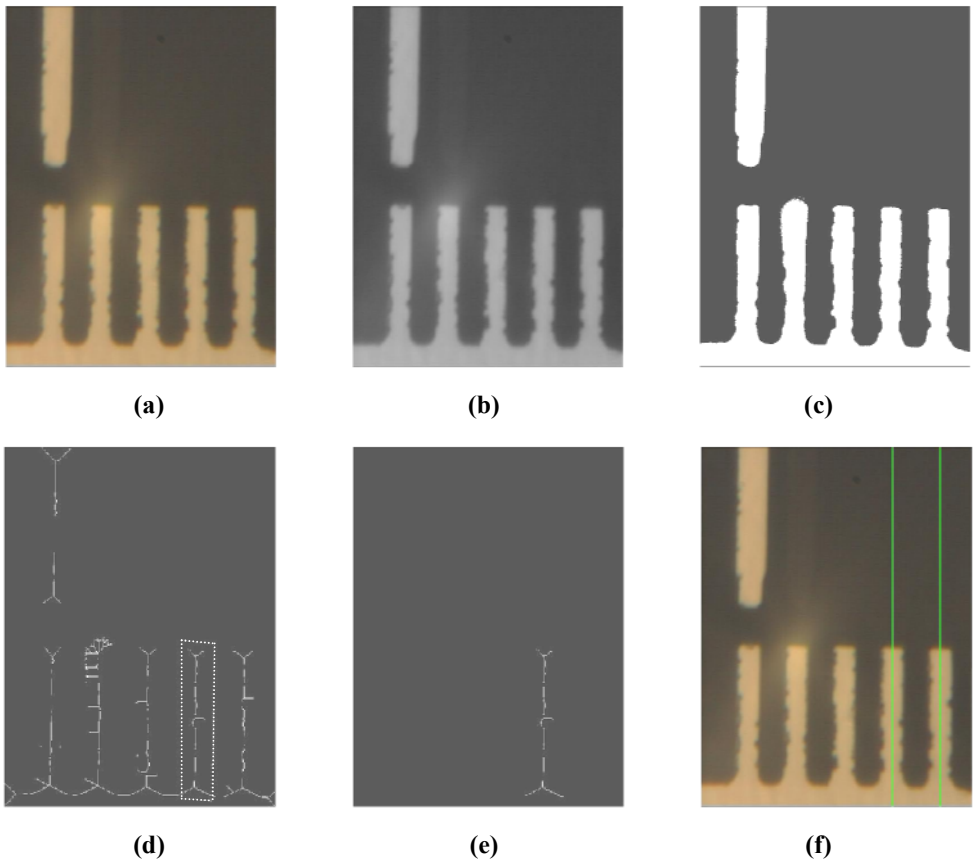

Figure 6. 6: Detection of central axes of scale fingers (a) Color bitmap of base image (b) Intensity bitmap of the image (c) Binary image (d) Skeleton of the image (e) Filtered image with the region of interest (f) Lines fitted to medial axes of adjacent fingers

After determining the pixel width in microns, dimensioning of the structures should be done. This includes basically the determination of the widths of beams, gap spacing and other critical sections. Similar to the calibration procedure the color bitmap of the image is first converted to intensity bitmap and then to binary image. However instead of skeletonization of the image, the perimeter of the

entities in the binary image is detected as the next step. Thus the edge of the structure is detected (Figure 6.7b). After generating the edge view, parallel lines are fitted to the opposing sides of the entity to be measured. In order to achieve this, similar to the calibration process, the image is filtered with a selected region enclosing the sides (Figure 6.7c). Parallel lines are fitted again by using the radon transform of the image.

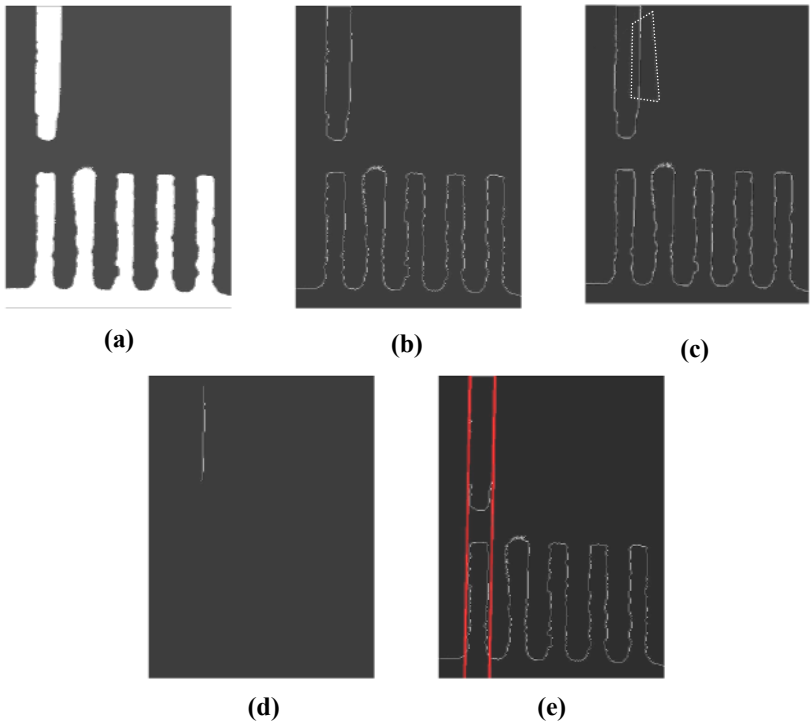

Figure 6. 7: Measurement of the beam width (a) Binary map of the base image (b) Detection of edges (c) Selecting the region of interest (d) Filtered image with the region of interest (e) Lines fitted to the sides of the beam

At this point, the pixel width is corrected along the normal direction to the lines detected. The procedure is illustrated in Figure 6.8, where a single pixel is shown. The distance between the parallel lines detected is multiplied with this corrected pixel width in order to determine the width of the beam in microns.

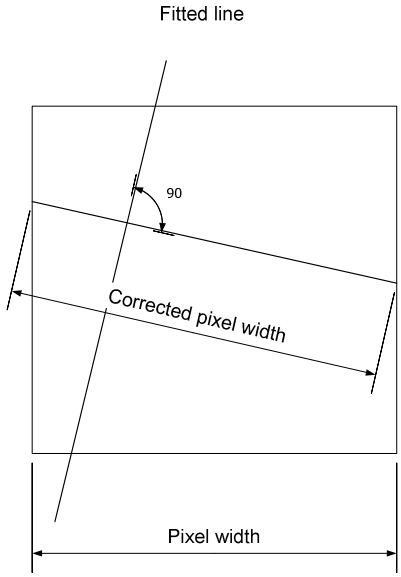

Figure 6. 8: Correction of pixel width (single pixel is shown)

Accordingly the beam width is read to be 4.037 μm, which is the result for 20 readings, which shows that the superior repeatability. The corrected pixel width is computed to be 0.082 μm. Thus the resulting beam width is 4.037 ± 0.041 μm, which is a much more precise result comparing to that obtained from the previous version. Unfortunately there is not enough data to extract any information about the accuracy of the results. Due to unsharp corners there is always a non uniform reflection of light from the surface, which creates a blank zone. Figure 6.9 shows the close up image of two electrodes in pull-in. The electrodes are necessarily mating, however due to non uniform reflection of light there is a dark zone between the electrodes. This means that the widths determined using the above script always underestimates the real dimension, and overestimates the gap spacing, which can not be overcome. But it can be concluded that the improved script should yield better results for properly focused snapshots of patterns with minor surface irregularities and relatively sharper corners.

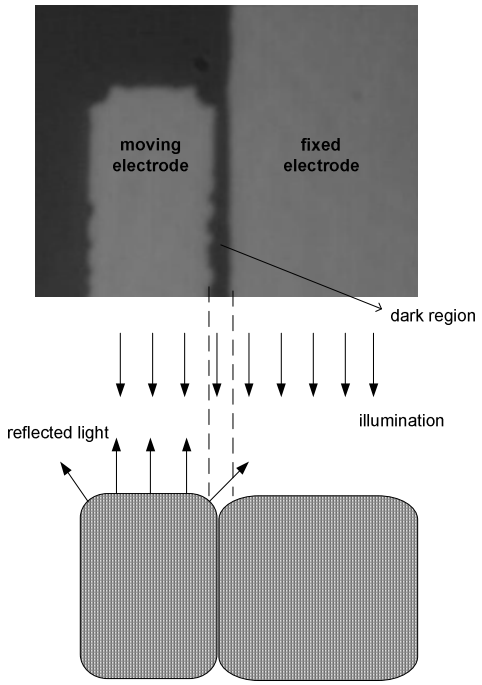

Figure 6. 9: Non uniform reflection of light from structure surface. Grayscale image shows the pull in of moving electrode

The only drawback of the improved script is that it becomes useless for the snapshots of the patterns with high surface irregularities, such as the structures fabricated by electroplating. Due to high irregularities it is almost impossible to detect the edges properly (Figure 6.10). In these cases the primitive version of the scripts can be the solution. However it should be noted that non uniform illumination naturally creates problem in either case.

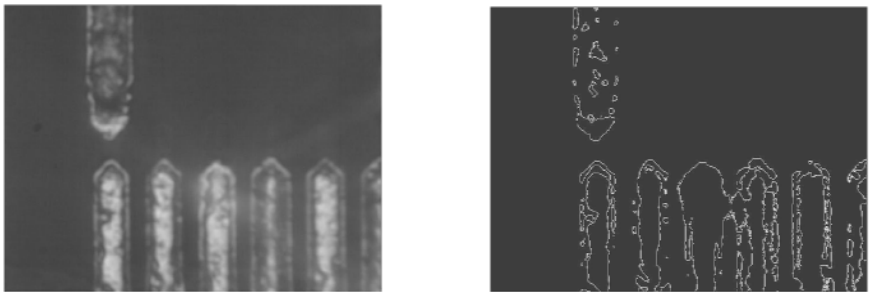

Figure 6. 10: Edges of a grayscale image of a pattern formed by Ni electroplating

Different from the other two modules, the module for measuring the relative displacements processes more than one image, which are captured at successive voltage increments. Similar to the case of dimensioning module, edge of the structure pattern is detected, and a reference line is selected on the image captured at zero voltage by again filtering the whole image with a selected region. For the successive snapshots, in order to determine the displacement of the reference line the regions are selected such that they enclose the same entity. By fitting lines, which are parallel to the reference line, to the entity lying inside the region of interest, relative displacement of the indicator – whether the tip of the cantilever beam or the indicator at the mid of the double clamped beam – is determined. Figure 6.11 illustrates the procedure. It should be stated that the module is used in only testing of cantilever beam bending and double clamped beam bending devices.

The lack of precision which is the major drawback of the dimensioning module is naturally overcome in this module since the displacement is measured relative to a reference line selected on the image. The script of each module is given in Appendix D.

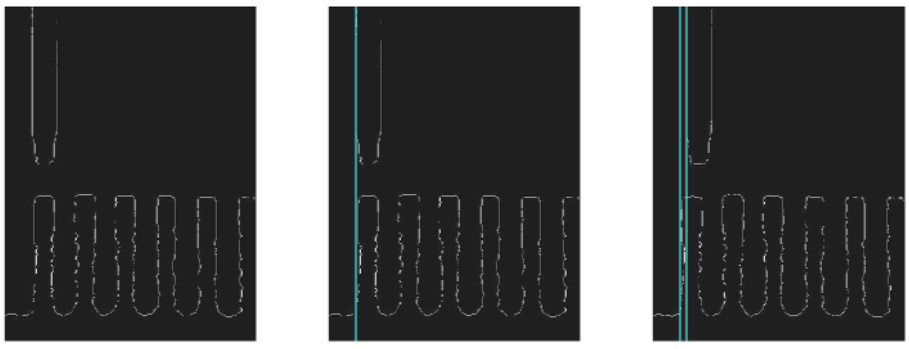

(a) **(b)** **(c)**

Figure 6. 11: Determining the relative displacement (a) Edge of the pattern (b) Reference line (c) Displaced line

6.3 Test Results

As stated in previous chapters the devices are fabricated by nickel electroplating and deep reactive ion etching of (111) oriented silicon. It should be recalled that two separate runs of DRIE are done for fabricating (111) silicon structures. Additionally cantilevers pull-in devices on (100) oriented silicon on insulator are tested.

With its single crystal structure, silicon is an elastically anisotropic material. However on (111) crystallographic plane the elastic modulus, Poisson's ratio and shear modulus are constant along each direction [21], which makes (111) silicon an outstanding material. Since the elastic modulus is well defined for (111) silicon, it is aimed to verify the devices according to the test results obtained from (111) silicon devices. Accordingly, results of the tests conducted on (111) silicon structures are first presented and then the results of the tests on electroplated nickel devices for characterization of nickel are given.

6.3.1 Testing of DRIE (111) Silicon Samples

Actually the (111) silicon devices are fabricated in two separate runs of DRIE. It was mentioned in Chapter 5 that photoresist is used as masking material in deep reactive etching. However the photoresist used in the first run of DRIE can not successfully withstand the reactive ions. Because of this the structures are thinned. Moreover in some regions the photoresist mask is completely etched resulting in the etching of the silicon from the surface. This yields highly irregular surface. Accordingly it is impossible to extract information from the test results obtained from these samples. As a result, although there are two different sets of silicon samples fabricated through two separate runs of DRIE, the results obtained from the first set of samples of cantilever beam bending device and improved cantilever pull-in device are not mentioned here.

In the second run of DRIE, a different photoresist is used in order to prevent the undesired etching. However, in this case due to excess wet etching of the underlying glass substrate, the anchors with small surface areas are stripped away from the substrate making some devices useless. Recall that it is the case for fatigue test devices, which is mentioned in the previous chapter. Same case is observed for double clamped beam bending devices also. Double clamped beam bending devices also failed as the anchors of the suspensions are all split. Therefore the only surviving samples of double clamped beam bending devices are from the first run of DRIE and thus the results of the tests conducted on these samples are presented here.

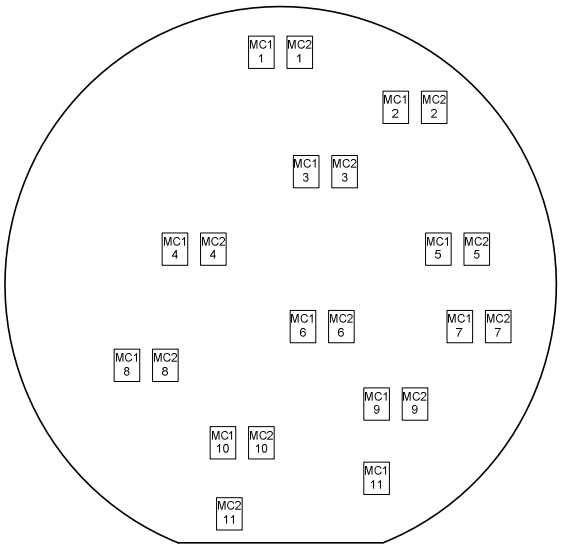

Figure 6. 12: Layout of mechanical characterization dies on (111) silicon wafer bonded to glass wafer

The tests on (111) silicon structures are done on wafer level in order to extract information about how the properties change according to the location on the wafer. This means that the wafer is placed on the probe station as a whole. The locations of the mechanical characterization dies are roughly shown in Figure 6.12. In the figure, MC1 denotes the mechanical characterization chip whose layout is given on Figure E.1 and MC2 denotes the mechanical characterization

chip whose layout is given on Figure E.2 in Appendix E. Wafer locations are identified by numbers written under chip designations. Due to faulty processing, not every device on the wafer could survive. Even it could not be possible to obtain any working device on locations 7 and 11. The results also show that the tests conducted on the dies which are close to wafer perimeter do not yield consistent results and may be treated as outliers. The numerical results and interpretation are presented in following subsections in details.

6.3.1.1 Results of Cantilever Beam Bending Tests

The devices are fabricated in varying dimensions. Design dimensions and device designations are presented in Section 3.3.

In order to interpret the test results displacement versus voltage data is extracted using the scripts explained in the previous chapter and plotted. It is known from the mathematical model derived in Section 3.3 that the displacement is related to the voltage with a quadratic of type $\delta = AV^2$, in which the coefficient A is related to the elastic modulus with the mathematical model. Thus quadratic curves are fitted to the voltage displacement data, minimizing the mean squared error. Figure 6.14 shows the quadratic curves fitted to the data obtained from testing of cantilever beam bending devices on wafer location 6.

The coefficient of the quadratic term (A) is a function of both elastic modulus and the device dimensions. Inserting the measured device dimensions and the coefficient of the quadratic term in the mathematical model elastic modulus can be extracted. Measured device dimensions, corresponding coefficient A and the elastic modulus calculated are tabulated in Table 6.2. Wafer locations are also given in order to compare the results obtained from different regions.

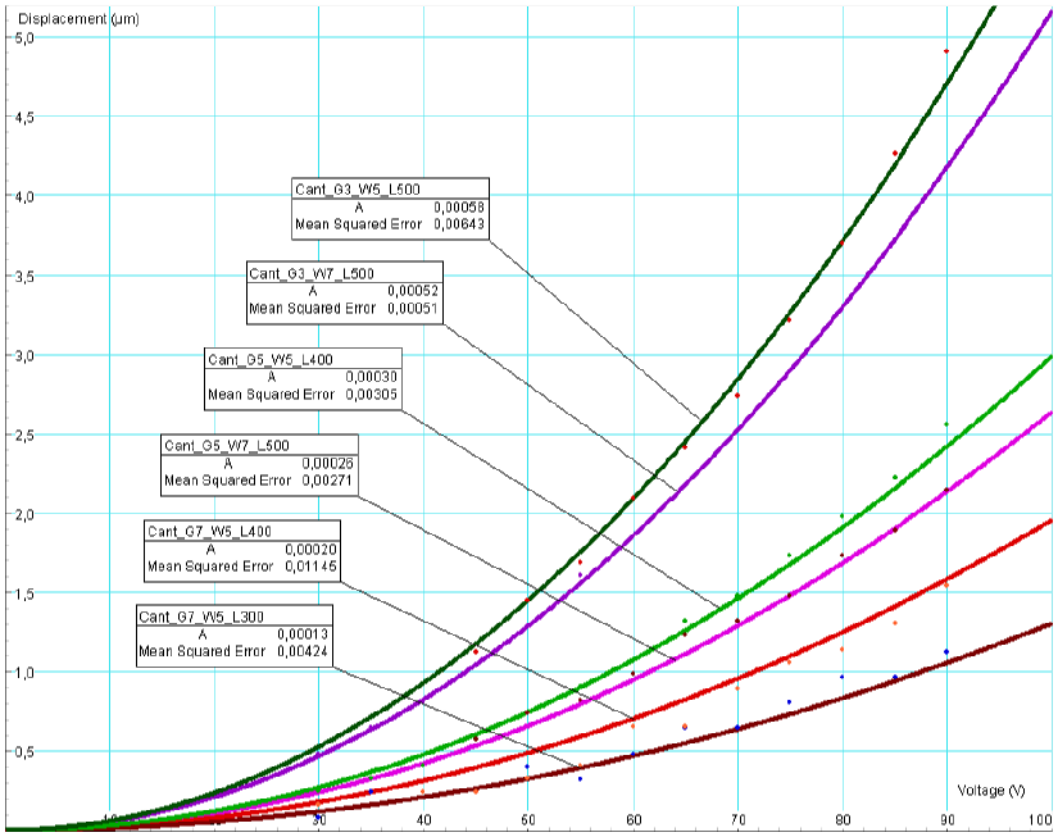

Figure 6. 13: Displacement versus voltage data and curves for MC1 at location 6

Note that only 15 samples could be tested according to Table 6.2. This is mainly due to fabrication faults. Especially during the polymer etching the weak parts of the devices on the wafer are broken and the small residues fill the cavities under the structures. These residues can cause contact during tests. This is why most of the structures could not be tested.

Note that the device dimensions greatly alter for the samples from the wafer location 1, which is close to the wafer edge. Also the elastic modulus computed for these samples are very low. Considering the inconsistency in the device dimensions, modulus values extracted from these samples can be treated as outliers. The remaining are unbiased estimates of elastic modulus values. These estimates of elastic modulus for (111) silicon averages to 141.2 GPa with standard deviation of 25.3 GPa. However since the sample size is pretty low and the

deviation is considerably high, it is not proper to evaluate the elastic modulus with a specified tolerance.

Table 6. 2: Results of the cantilever beam bending tests on (111) silicon

wafer location	designation	actual finger gap (µm)	actual cantilever beam width (µm)	actual suspension beam width (µm)	coefficient of the quadratic term (*A*) (µm/V^2)	E (elastic modulus) (GPa)
1	Cant_G5_W5_L400	6.78	3.42	1.86	0.00143	75.2
1	Cant_G5_W5_L500	6.1	3.35	1.93	0.00141	85.0
1	Cant_G5_W7_L500	5.67	5.9	3.02	0.000358	88.7
2	Cant_G3_W5_L500	3.77	4.31	3.05	0.000497	136.8
2	Cant_G5_W5_L400	5.67	4.16	3.01	0.000228	158.0
2	Cant_G3_W7_L500	3.68	6.1	3.14	0.000369	153.1
3	Cant_G3_W5_L300	3.59	4.04	3.05	0.000505	156.4
3	Cant_G5_W5_L500	5.67	4.08	3.01	0.000188	195.2
3	Cant_G7_W5_L500	7.49	3.91	3.09	0.000167	128.3
6	Cant_G3_W5_L500	4.31	3.99	3.01	0.00058	108.2
6	Cant_G5_W5_L400	5.87	4.02	2.74	0.000298	150.7
6	Cant_G7_W5_L300	7.74	4.28	3.05	0.00013	145.4
6	Cant_G7_W5_L400	7.49	4.23	2.77	0.000195	140.9
6	Cant_G3_W7_L500	4.04	6.18	3.13	0.000515	100.0
6	Cant_G5_W7_L500	5.94	6.11	2.93	0.000263	121.3

6.3.1.2 Results of Double-Clamped Beam Bending Tests

As stated in Section 6.3.1, the results of double clamped beam bending test are collected from testing of the samples fabricated in the first run of DRIE. The tests are conducted on chip level using two dies of whose layout is shown on Figure E.2 in Appendix E. Design dimensions and device designation are given in Section 3.3 for the double clamped beam bending test device.

However, due to same reason stated in previous section, only 4 of the samples over 16 devices could be tested. The devices mostly fail because of broken test beams or suspension beams. The results are extracted following the same

procedure explained in the previous section. Displacement versus voltage curves are shown on the graph in Figure 6.14, and the results are tabulated in Table 6.3.

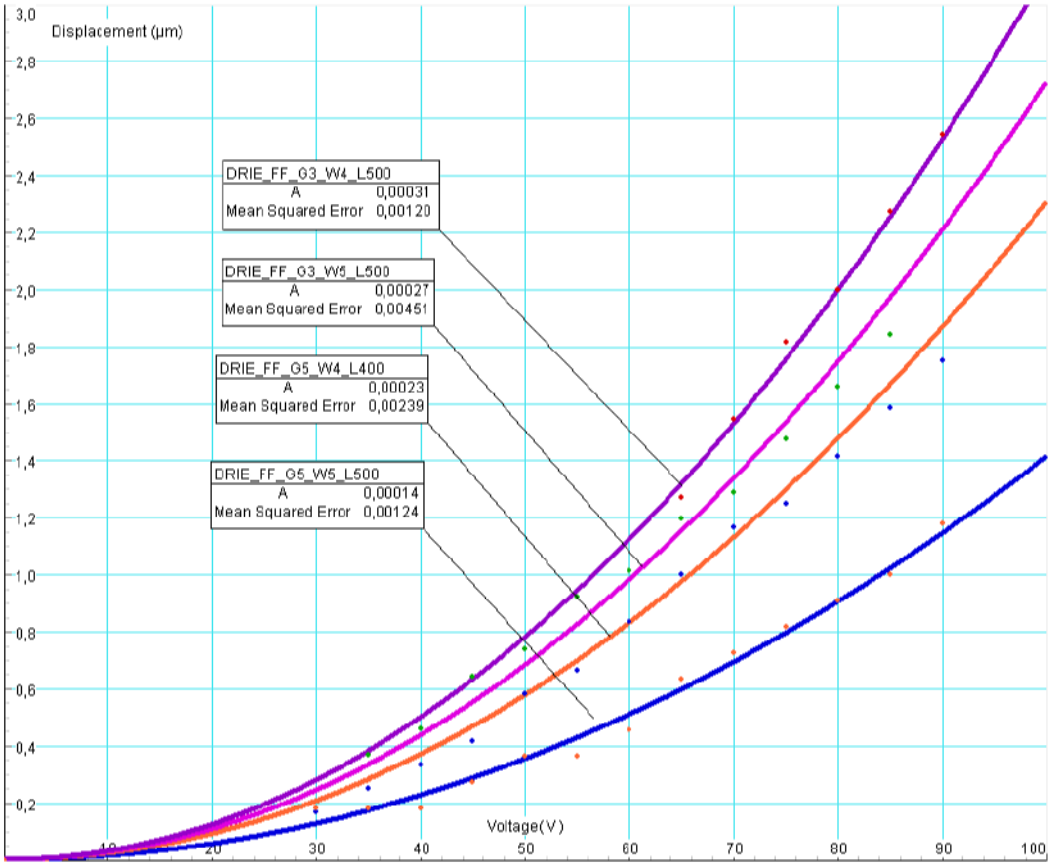

Figure 6. 14: Displacement versus voltage data and curves for double clamped beam bending

Table 6. 3: Results of the double clamped beam bending tests on (111) silicon

designation	actual gap between fingers of comb drive (µm)	actual width of double clamped beam (µm)	actual width of the suspension beam (µm)	coefficient of the quadratic term (A) (µm/V^2)	E (elastic modulus) (GPa)
DRIE_FF_G3_W4_L500	5.73	3.01	1.64	0.000311	150.7
DRIE_FF_G3_W5_L500	5.43	3.68	1.66	0.000272	105.9
DRIE_FF_G5_W4_L400	5.42	3.12	1.67	0.000230	82.4
DRIE_FF_G5_W5_L500	5.31	3.90	1.82	0.000141	134.3

Investigating Table 6.3, measured device dimensions seems to be consistent, however the structures have high surface irregularities, and thus the accuracy of the results can not be validated. As a result, elastic modulus estimates are widely scattered. Moreover since the sample size is very low; it does not make sense to calculate the expected value of the elastic modulus of (111) silicon using the results of the double clamped beam bending tests.

6.3.1.3 Results of Improved Cantilever Pull-in Tests

The cantilever pull-in test results are obtained from testing of the (111) silicon samples fabricated in the second run of DRIE. Similar to the other test devices, cantilever pull-in devices are fabricated in various dimensions. Design dimensions and device designations are presented in Section 3.3.

On the contrary to the cantilever beam and double clamped beam bending test devices, many of the cantilever pull-in devices survived. Measured pull-in voltages, device dimensions, and the elastic modulus computed using the mathematical model is given below in Table 6.4. Note that the wafer locations are also given.

The dimension readings are generally consistent within the dies. However the elastic modulus values computed are totally meaningless. This result arises from the possible erroneous measurement of the device dimensions. Since the elastic modulus is very sensitive to the variables measured, a small variation in dimension yields a high error. The dependence of the elastic modulus value to the variables is discussed in details in Chapter 7.

Table 6. 4: Results of the cantilever pull-in tests on (111) silicon

wafer location	designation	actual gap between parallel plates (µm)	actual width of the cantilever beam (µm)	pull-in voltage (V)	E (elastic modulus) (GPa)
1	PullIn_G3_W4_L250	4.96	2.84	20	13.4
1	PullIn_G3_W5_L250	4.96	3.54	38	24.9
1	PullIn_G5_W5_L200	6.38	4.08	97	25.5
4	PullIn_G3_W4_L250	4.53	3.38	32	26.6
4	PullIn_G3_W5_L250	4.53	4.12	49	34.5
4	PullIn_G5_W5_L250	6.18	4.28	84	35.6
4	PullIn_G3_W5_L300	4.61	4.28	38	30.3
6	PullIn_G3_W4_L200	4.48	3.26	40	24.6
6	PullIn_G3_W5_L250	4.48	4.15	46	30.1
6	PullIn_G5_W4_L250	6.35	3.01	50	33.4
6	PullIn_G5_W5_L250	6.19	4.15	81	36.1
6	PullIn_G3_W4_L300	4.56	3.42	23	22.5
6	PullIn_G3_W5_L300	4.48	4.23	38	34.2
6	PullIn_G5_W4_L300	6.43	3.17	42	33.6
7	PullIn_G5_W4_L250	6.44	3.14	53	31.7
7	PullIn_G3_W5_L300	5.07	4.02	50	47.6
7	PullIn_G5_W4_L300	6.36	3.22	41	31.6
8	PullIn_G3_W4_L250	4.23	3.58	32	27.5
8	PullIn_G3_W5_L250	4.23	4.88	43	19.6
8	PullIn_G5_W4_L300	5.86	3.74	49	36.8
9	PullIn_G3_W4_L250	5.37	3.17	31	18.2
9	PullIn_G5_W4_L250	7.24	3.17	50	19.3
9	PullIn_G3_W4_L300	5.37	3.09	23	18.7
9	PullIn_G5_W4_L300	7.33	3.09	38	20.1
9	PullIn_G5_W5_L300	7.33	4.15	60	20.6
10	PullIn_G3_W4_L250	4.75	3.3	32	24.8
10	PullIn_G3_W5_L250	4.83	4.26	50	26.8
10	PullIn_G3_W4_L300	4.67	3.38	26	27.7

6.3.2 Testing of Electroplated Nickel Samples

As explained in previous chapters, the dimensions, basically the width, of electroplated nickel structures are considerably larger than the designed dimensions. Even it is not possible to release some structures as the material fills in the gaps. This is especially a problem in releasing of comb fingers. Because of this fact, most of the cantilever pull-in devices and some of the double clamped beam bending devices could not be tested.

The tests are conducted on chip level. There are three mechanical characterization chips whose layouts are given in Appendix E. The first chip contains cantilever beam bending devices (Figure E.3), the second chip includes two of the double clamped beam bending devices (Figure E.4) and the last chip (Figure E.5) contains the remaining double clamped beam bending devices, cantilever pull-in devices and the stress gradient beams, which are mentioned in Section 3.1. Note that the second chip also contains the primitive version of the cantilever beam bending test devices. These samples are also tested, but since they get into pull-in in very first voltage levels, it could not be possible to obtain any data.

The results of the tests conducted on electroplated nickel samples are presented in following subsections in details.

6.3.2.1 Results of Cantilever Beam Bending Tests

Dimensions of cantilever beam bending test devices of electroplated nickel slightly differs from those of its counterparts on (111) silicon substrate. Also the width of the suspension beam is designed to be 2 μm, which is thinner than that of samples on (111) silicon, in order to compensate for the bulging of the beam. The device dimensions are given in Section 3.3.1.

Primitive version of the MATLAB scripts are used in order to determine the device dimensions. The results obtained are tabulated below (Table 6.5).

Comparing the measured dimensions and design dimensions, the effect of bulging of the structures can be seen. This condition yields some devices, especially the cantilever pull-in devices and fatigue test devices, as explained in previous chapter, to loose their functions.

Table 6.5: Results of the cantilever beam bending tests on electroplated nickel

designation	actual gap between fingers of comb drive (µm)	actual width of cantilever beam (µm)	actual width of the suspension beam (µm)	coefficient of the quadratic term (A) (µm/V^2)	E (elastic modulus) (GPa)
Ni_Cant_W3_L300	2.93	5.84	4.75	0.000081	250.8
Ni_Cant_W3_L400	2.71	5.97	4.92	0.000099	209.4
Ni_Cant_W5_L300	3.22	7.94	4.75	0.000086	162.8
Ni_Cant_W5_L400	2.94	7.86	4.92	0.000108	157.1
Ni_Cant_W8_L300	2.89	11.06	4.79	0.000066	138.8
Ni_Cant_W8_L400	3.19	11.20	4.84	0.000100	116.8
Ni_Cant_W8_L500	2.99	11.21	5.11	0.000107	123.6
Ni_Cant_W3_L500	3.00	5.80	4.82	0.000161	123.0
Ni_Cant_W5_L500	2.85	8.07	5.03	0.000153	112.0

The average of the elastic modulus values is calculated to be 154.9 GPa with standard deviation of 47.1 GPa. Similar to the results of the other tests, computed elastic modulus values disperse in a wide range. This makes it again impossible to conclude on an acceptable tolerance range.

6.3.2.2 Results of Double Clamped Beam Bending Tests

Similar to the cantilever beam bending test devices, design dimensions of double clamped beam bending test devices of electroplated nickel differ from those of (111) silicon. Design dimensions and device designations given in Section 3.3.2.

Since the stiffness of double clamped beams are naturally higher than the stiffness of a cantilever of same dimensions, the design dimensions for the device are arranged in order to lower the stiffness of the structures and enable the test beams to actuate. Also, the width of the suspension beam is set to 2 µm. The results of the tests and the measured dimensions are tabulated in Table 6.6.

Due to contact between the comb fingers, the device with 3 µm wide, 500 µm long test beam could not be tested. It can be seen from Table 6.6 that the elastic modulus values evaluated testing the other samples yield relatively lower values compared to that obtained from testing of cantilever beam bending devices. The

average is 101.1 GPa with standard deviation of 24.4 GPa. While the dispersion is relatively lower, the average is also lower considerably lower than the value reported, which is about 200 GPa for nickel films [22].

Table 6. 6: Results of the double clamped beam bending tests on electroplated nickel

designation	actual gap between fingers of comb drive (µm)	actual width of double clamped beam (µm)	actual width of the suspension beam (µm)	coefficient of the quadratic term (A) (µm/V^2)	E (elastic modulus) (GPa)
Ni_FF_W2_L500	1.74	4.48	4.37	0.000442	74.2
Ni_FF_W3_L400	1.54	5.10	4.59	0.000146	123.7
Ni_FF_W3_L450	1.70	5.17	4.36	0.000278	76.8
Ni_FF_W2_L400	1.49	4.40	4.45	0.000210	124.2
Ni_FF_W2_L450	1.55	4.47	4.41	0.000288	106.4

6.3.2.3 Results of Improved Cantilever Pull-in Tests

There are only four cantilever pull-in devices located on the mechanical characterization chip (Figure E.5). The dimension variations of these devices are given in Section 3.3.3.

Among these four test devices, only the ones with 6 µm gap could survive. The electrodes of the devices with 4 µm gap are already in contact after the release of the structure. The results are tabulated below (Table 6.7).

Table 6. 7: Results of the cantilever pull-in tests on electroplated nickel

designation	actual gap between parallel plates (µm)	actual width of the cantilever beam (µm)	pull-in voltage (V)	E (elastic modulus) (GPa)
Ni_PI_G6_W4_L200	2.97	6.42	86	163.2
Ni_PI_G6_W3_L200	2.98	5.62	69	155.1

While the results are very consistent, it is not proper to estimate the exact elastic modulus value using results of only two samples.

6.3.3 Testing of Cantilever Pull-in Devices on (100) Silicon on Insulator

The pull-in devices on (100) silicon on insulator substrate are the primitive version of cantilever pull-in devices explained in Section 3.3.3. Device dimensions are given in Section 3.3.3.

As mentioned before single crystal silicon is elastically anisotropic. However on (111) crystallographic plane the elastic modulus and Poisson's ratio are constant along each direction, that is (111) silicon is an outstanding material from this point of view. Silicon also shows similar behavior on (100) plane also. However elastic modulus and Poisson's ratio are only equal and constant along <100> and <010> directions [21], which are respectively normal and parallel to the flats on (100) SOI wafer (Figure6.15). Since the devices are oriented along these directions, the elastic modulus values, which are computed using the mathematical model, should be the estimates of the exact value, which is 130.2 GPa [21].

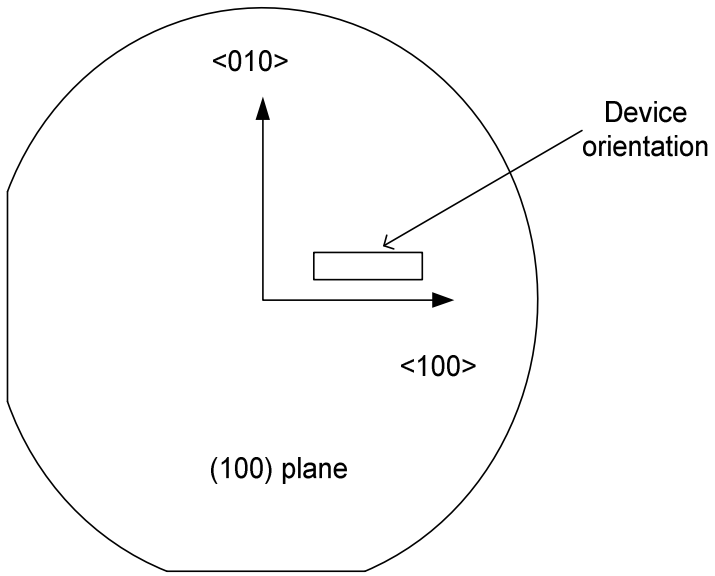

Figure 6. 15: Device orientations on (100) SOI wafer

5 sets of above specified samples are tested. Considering the fabrication of the (100) SOI structures mentioned in Section 3.4, dimensional accuracy is even better than that provided by deep reactive ion etching. Hence, actual dimensions are assumed to be the same as the design dimensions. The pull-in voltages measured and the elastic modulus values calculated are tabulated in Table 6.8. Only 2 samples over 20 failed, and the remaining 18 samples yield consistent results. The average of the elastic modulus values is computed to be 151.7 GPa with standard deviation of 14.7 GPa. Assuming the measurements are unbiased, student's t distribution is fitted. Thus, for 95% confidence level, the elastic modulus for (100) silicon along the axes shown on Figure 6.15, is found to be 151.7±32.3 GPa.

Table 6. 8: Results of cantilever pull-in devices on (100) SOI

designation	Pull-in Voltage (V)	E (elastic modulus) (GPa)
SOI_PI_W6_200	117	132.3
SOI_PI_W10_200	258	139.3
SOI_PI_W6_400	38	164.8
SOI_PI_W10_200	252	133.1
SOI_PI_W6_400	37	154.9
SOI_PI_W10_400	85	174.2
SOI_PI_W6_200	125	151.3
SOI_PI_W10_200	271	153.4
SOI_PI_W6_400	38	164.8
SOI_PI_W10_400	84	174.2
SOI_PI_W6_200	119	137.6
SOI_PI_W10_200	265	146.9
SOI_PI_W6_400	37	154.9
SOI_PI_W10_400	82	164.8
SOI_PI_W6_200	115	127.1
SOI_PI_W10_200	256	136.8
SOI_PI_W6_400	37	154.9
SOI_PI_W10_400	82	164.8

Obviously, this is the least dispersed data obtained among all tests conducted. However the range of data is still not satisfactory. Since the dimensional accuracy is superior compared to the devices fabricated on (111) silicon and nickel, the

effect of change in dimension can not be the reason. Note that the accuracy in measuring the voltage is 1 Volt. The reason for the wide dispersion is probably due to the reading error in voltage measurement. Considering the mathematical model derived in Section 3.3.3 (equation (3.35)), it can be seen that calculated elastic modulus changes with the square of the measured pull-in voltage. Thus any error involved in reading of the pull-in voltage yields a higher error in elastic modulus.

6.4 Finite Element Analysis of Devices

Static analyses of cantilever beam and double clamped beam bending test devices are done using ANSYS 7.0 using the data obtained from the tests in order to verify the models. The analysis for the devices requires electromechanical coupling of the capacitive and elastic domains. There are mainly two approaches in order to achieve a solution in such a coupling problem using ANSYS. These are the direct coupling of the domains or sequential solution, which successively solve the problem in capacitive and elastic domains. Direct coupling utilizes electromechanical transducer elements, which convert energy from electrostatic domain to structural domain [17]. On the other hand sequential solution utilizes a macro, which provides the successive solution in electrostatic and structural domains. It is reported that direct coupling method provides more robust and faster convergence than the sequential method [17], however it could not be possible to converge a solution using direct coupling in analyses of the structures. Hence sequential solution method is utilized in finite element analysis of the structures.

Two dimensional models of the structures are created using separate CAD software (KEYCREATOR 3.0). These models are then imported in ANSYS 7.0 environment in initial graphics exchange specification (*.iges) file format for processing. Sample batch file used for analysis is given in Appendix C. Devices

are modeled using actual dimensions according to the measurements. Also the elastic modulus values computed for each device are used in the solver in order to compare the displacement values obtained from finite element analysis and the experiment. For the meshing, the model is divided into four areas (Figure 6.16); fixed electrode of the comb drive, test beam and the moveable electrode, surrounding air and the air gap between the fingers of the comb drive. In the analysis, it is critical that the gap between the fingers is finely meshed in order to successfully couple the domains. The surrounding air is coarsely meshed and relatively finer elements are used to mesh the test beam. The fixed electrode is not meshed since it does not move. For the converge analysis, number of elements used for meshing the air gap between the comb fingers is increased.

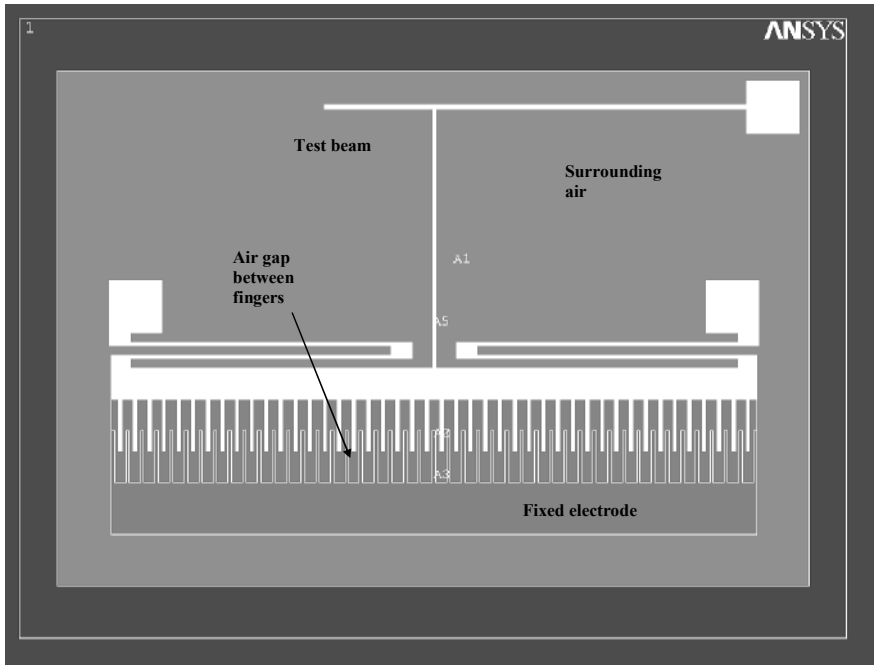

Figure 6. 16: Areas defined for meshing on 2D model of the cantilever beam bending test device

The convergence behaviors for the same geometry of devices are observed to be the same. That is the analysis of each cantilever beam bending test device or

double clamped beam bending test device converge similarly to the result. Hence only the convergence of DRIE_Cant_G3_W5_L300 and DRIE_FF_G3_W4_L500 are shown in Figure 6.17 as samples.

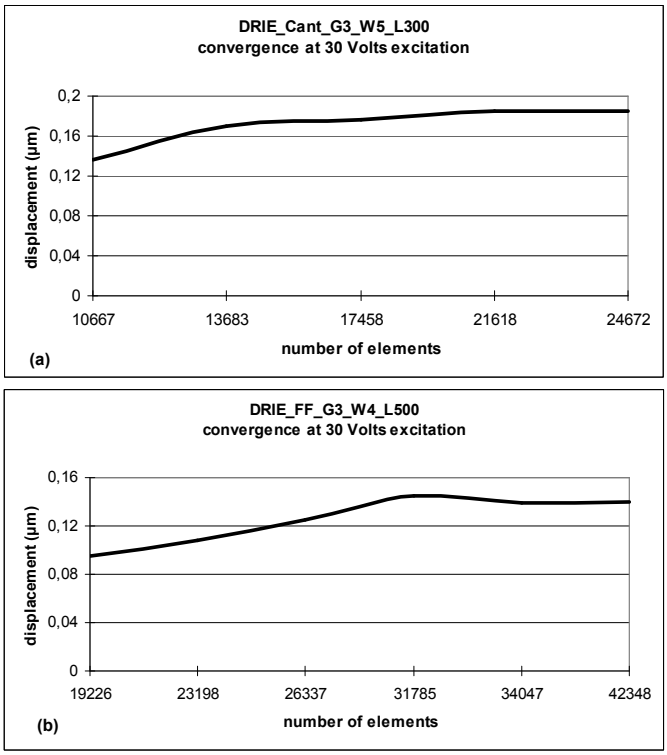

Figure 6. 17: (a) Convergence of DRIE_Cant_G3_W5_L300 (b) Convergence of DRIE_FF_G3_W3_L500

Displaced structures are shown in Figure 6.18 below. Note that the moveable electrode in cantilever beam bending test device is not exactly horizontal as seen from the contours (Figure 6.18a). This is because of the asymmetry of the structure. As the voltage is increased, this inclination becomes more obvious and eventually results in side pull-in of the structure. Because of this, data gathered at relatively lower voltages is used for the curve fitting explained in the previous section. While it is not so obvious in case of double clamped beam bending (Figure 6.18b) due to its symmetric nature, as the device approaches the onset of

pull-in, inclination of the moveable electrode with smaller magnitude is also observed.

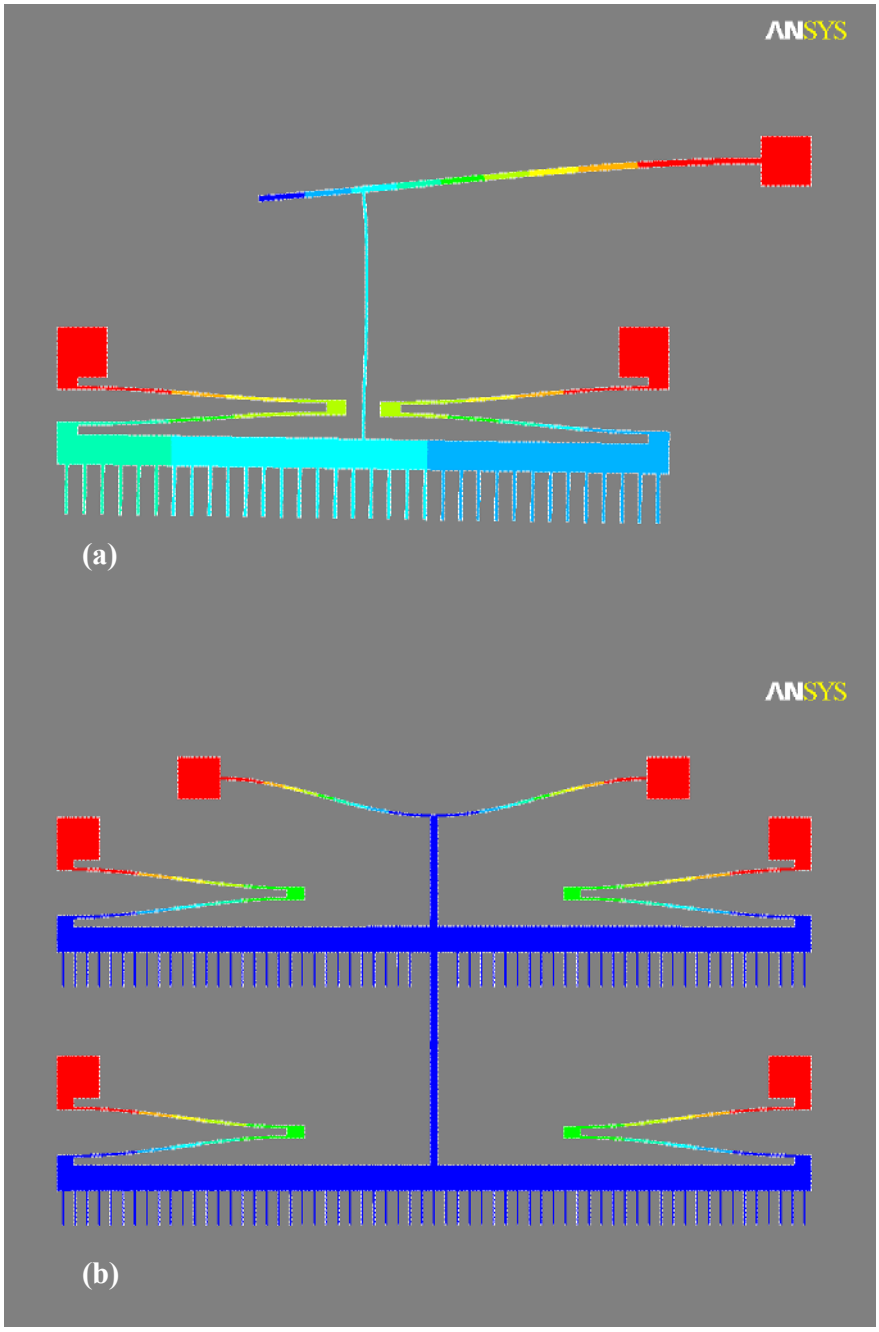

Figure 6. 18: Displaced (a) cantilever beam bending test structure (b) double clamped beam bending test structure

Recalling that a quadratic curve is fitted to the data points obtained through tests in order to extract elastic modulus, similar approach is applied in finite element analysis. The analyses are done for 30 Volts, 45 Volts and 60 Volts excitations for each device to fit a quadratic curve of type $\delta = AV^2$. This practice also justifies the correctness of the finite element solution of displacement which should be proportional to the square of the voltage. Then, the A values obtained from the tests and the finite element analyses are compared in order to comment on the validity of the mathematical model. The values of the coefficient of the quadratic term obtained from the tests and the analyses, and the ratio between them are tabulated below (Table 6.9, Table 6.10).

Table 6. 9: Comparison of experimental and finite element analysis solutions for cantilever beam bending test devices on (111) silicon.

wafer location	designation	A_{exp} (experimental) ($\mu m/V^2$)	A_{FEA} (FEA) ($\mu m/V^2$)	A_{exp}/A_{FEA}
3	DRIE_Cant_G3_W5_L300	0.000505	0.000210	2.40
2	DRIE_Cant_G3_W5_L500	0.000497	0.000290	1.71
6	DRIE_Cant_G3_W5_L500	0.000580	0.000369	1.57
2	DRIE_Cant_G3_W7_L500	0.000369	0.000234	1.58
6	DRIE_Cant_G3_W7_L500	0.000515	0.000356	1.45
2	DRIE_Cant_G5_W5_L400	0.000228	0.000105	2.17
6	DRIE_Cant_G5_W5_L500	0.000298	0.000110	2.71
3	DRIE_Cant_G5_W5_L500	0.000188	0.000099	1.90
6	DRIE_Cant_G5_W7_L500	0.000263	0.000133	1.98
6	DRIE_Cant_G7_W5_L300	0.000130	0.000058	2.24
6	DRIE_Cant_G7_W5_L400	0.000195	0.000060	3.25
3	DRIE_Cant_G7_W5_L500	0.000167	0.000109	1.53

Table 6. 10: Comparison of experimental and finite element analysis solutions for double clamped beam bending test devices on (111) silicon.

designation	A_{exp} (experimental) ($\mu m/V2$)	A_{FEA} (FEA) ($\mu m/V2$)	A_{exp}/A_{FEA}
DRIE_FF_G3_W4_L500	0.000311	0.000156	2.00
DRIE_FF_G3_W5_L500	0.000272	0.000102	2.66
DRIE_FF_G5_W4_L400	0.000230	0.000089	2.60
DRIE_FF_G5_W5_L500	0.000141	0.000046	3.06

Table 6. 11: Comparison of experimental and finite element analysis solutions for cantilever beam bending test devices on electroplated nickel.

designation	A_{exp} (experimental) (µm/V2)	A_{FEA} (FEA) (µm/V2)	A_{exp}/A_{FEA}
Ni_Cant_W3_L300	0.000081	0.000036	2.25
Ni_Cant_W3_L400	0.000099	0.000048	2.06
Ni_Cant_W3_L500	0.000086	0.000045	1.91
Ni_Cant_W5_L300	0.000108	0.000058	1.86
Ni_Cant_W5_L400	0.000066	0.000035	1.89
Ni_Cant_W5_L500	0.000100	0.000060	1.67
Ni_Cant_W8_L300	0.000107	0.000070	1.53
Ni_Cant_W8_L400	0.000161	0.000087	1.85
Ni_Cant_W8_L500	0.000153	0.000090	1.70

Table 6. 12: Comparison of experimental and finite element analysis solutions for double clamped beam bending test devices on electroplated nickel.

designation	A_{exp} (experimental) (µm/V2)	A_{FEA} (FEA) (µm/V2)	A_{exp}/A_{FEA}
Ni_FF_W2_L500	0.000442	0.000284	1.55
Ni_FF_W3_L400	0.000146	0.000074	1.97
Ni_FF_W3_L450	0.000278	0.000152	1.82
Ni_FF_W2_L400	0.000210	0.000106	1.98
Ni_FF_W2_L450	0.000288	0.000110	1.91

It is seen from the tables that the finite element analysis always underestimates the displacements, which is the common case in solving coupled electromechanical problems. This mainly comes out from the out of plane fringing electric fields. It is stated in Section 2.1 that the fringing fields are involved in actuation, however since the model is planar, out of plane fringes are not involved in the solution. As a result finite element analysis yields displacement values lower than the measured values. Accordingly, magnitude of the ratio of the experimental result to finite element analysis result around 1.5 can be acceptable. However FEA results for the test devices yield generally higher ratios which vary around 1.9, ignoring the few much higher ratios. Recalling that two dimensional models of the devices are done using the measured dimensions, this difference in ratio probably arises from erroneous measurement of the structure dimensions, which is explained in details in Section 6.2.

6.5 Conclusion of Static Tests

While it is aimed to compare the performance of the characterization devices through the results of the conducted tests, it could not be possible to evaluate the devices clearly due to widely scattered test results. Possible reasons are analyzed in Chapter 7 in details. However it can be concluded that the fabrication of the structures should be optimized and metrology involved should be accurate in order to well define the device geometry. Otherwise, the mathematical models derived for the devices could not be verified. Accordingly, it is not so feasible to compare the finite element results with the test results as the models could not be verified.

CHAPTER 7

CONCLUSION

It is stated in the first chapter that it is aimed to compare the validity of the mathematical models of different test devices fabricated using a relatively repeatable technique, through results of number of tests. However it could not be possible to completely evaluate the devices since the data gathered disperse in a very wide range for most of the tests or yield completely nonsense results. Although this is the case it is still possible to comment on the results.

Actually the problems in testing arise from the fact that the methods involved are indirect. That is the results are extracted through mathematical models which include many measured variables. The error in measuring these variables are then accumulated yielding seriously erroneous results, as seen in improved cantilever pull in testing. While keeping the structures, thus the models, simple particularly solves the problem, measurement error is still an important subject to deal with. In order to examine the problem in details the mathematical models for the cantilever beam bending test (equation (7.1)), double clamped beam bending test (equation (7.2)) and improved cantilever pull-in test (equation (7.3)) are recalled here.

$$\delta_{tip} = \frac{2n\varepsilon_o V^2}{gE} \cdot \frac{(l_s{}^3 l_c{}^2)(3l_e + 2l_c)}{(w_c{}^3 l_s{}^3 + 4w_s{}^3 l_c{}^3)} \tag{7.1}$$

$$\delta_{mid} = \frac{n\varepsilon_0 V^2}{gE} \cdot \frac{l_f^3 l_s^3}{(16w_f^3 l_s^3 + 2w_s^3 l_f^3)} \tag{7.2}$$

$$V_p = \sqrt{\frac{2}{27} \cdot \frac{Eg^3 w_c^{\,3}}{\varepsilon l_c^{\,3} l_o}} \tag{7.3}$$

where n is the number of finger couples in comb drive, g is the gap between electrodes (finger gap for comb drive, plate gap for pull-in device), w_s is the suspension beam width, w_c is the cantilever beam width, w_f is the double clamped beam width, l_c and l_f are the cantilever and double clamped beam lengths respectively, l_e is the length of the extension lever, l_o is the overlap distance for pull-in device, l_s is the length of the suspension beam and ε_0 is the free space permittivity. Therefore the elastic modulus can be interpreted as functions of the variables set in the above models. That is

$$E = f_{cant}(\varepsilon_0, n, V, \delta, g, l_e, l_s, l_c, w_c, w_s) \tag{7.4}$$

for cantilever beam bending device,

$$E = f_{ff}(\varepsilon_0, n, V, \delta, g, l_s, l_f, w_f, w_s) \tag{7.5}$$

double clamped beam bending device, and

$$E = f_{pi}(\varepsilon_0, V_p, g, l_o, l_c, w_c) \tag{7.6}$$

In case of testing single crystal structures, such as (111) silicon structures fabricated by DRIE, elastic modulus value is well defined and can be treated as constant. Moreover ε_0 is constant, n is defined specifically for the devices and lengths can also be treated as constants for each device. Therefore the only variables to be measured are widths, displacements and voltage. As the displacement can be accurately measured, as explained in Section 6.2, the coefficient of the quadratic term, A, defined in Section 6.3 for bending tests can be set as the variable equivalent to pull-in voltage variable in pull-in tests. At this point it should be stated that the variables A and V_p are also functions of the structure dimensions. Since the elastic modulus is constant for the case, it can be written that

$$A_{cant} = h_{cant}(g, w_c, w_s) \tag{7.6}$$

$$A_{ff} = h_{ff}(g, w_f, w_s) \tag{7.7}$$

$$V_p = h_{pi}(g, w_c) \tag{7.8}$$

The widths and the gaps are also defined through the design; however these dimensions change during fabrication. It is known for DRIE that the widths decrease and gaps increase after fabrication. If the magnitude of the decrease or increase of the dimension is assumed to be the same, it can be written that

$$A_{cant} = g_{cant}(R) \tag{7.9}$$

$$A_{ff} = g_{ff}(R) \tag{7.10}$$

$$V_p = g_{pi}(R) \tag{7.11}$$

where R is the magnitude of the change in dimension. The functions g_{cant}, g_{ff} and g_{pi} can be found by rephrasing the models. Resulting functions are given in the equations below.

$$A_{cant}(R) = \frac{2n\varepsilon_0(l_c^2 l_s^3)(3l_e + 2l_c)}{E(g+R)\left[(w_c - R)^3 l_s^3 + 4(w_s - R)^3 l_c^3\right]} \tag{7.12}$$

$$A_{cant}(R) = \frac{n\varepsilon_0(l_f^3 l_s^3)}{E(g+R)\left[16(w_f - R)^3 l_s^3 + 2(w_s - R)^3 l_f^3\right]} \tag{7.13}$$

$$V_p(R) = \sqrt{\frac{2E(w_c - R)^3 (g+R)^3}{27\varepsilon_0 l_c^3 l_o}} \tag{7.14}$$

Note that while R is added to gap, and subtracted from width. This means that the gaps are widened and widths are thinned during fabrication. The functions set above are graphically represented below. Figure 7.1a shows the variation of the coefficient with respect to the change in dimension in cantilever beam bending. Figure 7.1b also shows the variation of the coefficient, but in double clamped beam bending. Figure 7.1c shows the variation of pull-in voltage for one of the improved cantilever pull-in structure. Note that the measured values are also plotted on the graphs.

(a)

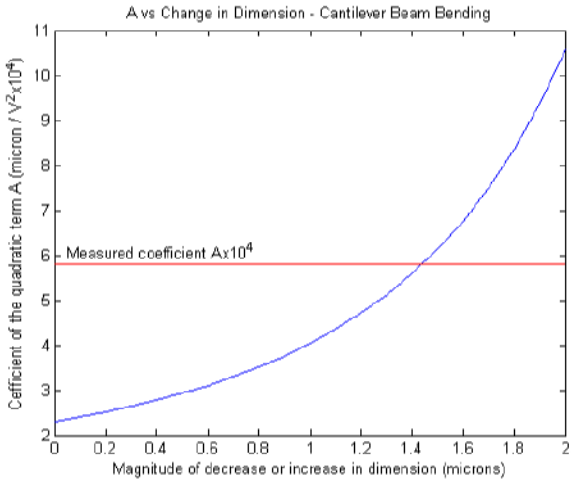

(b)

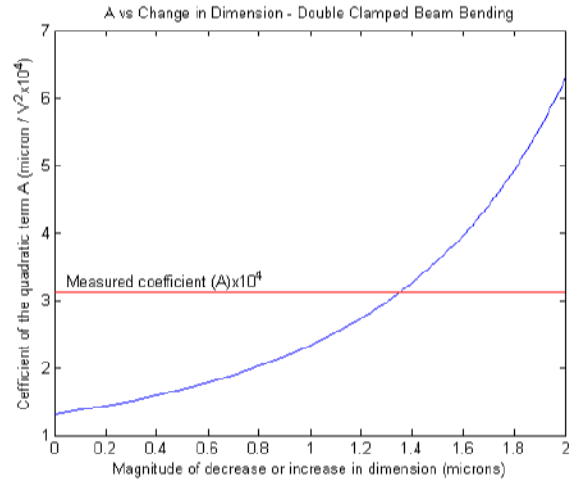

(c)

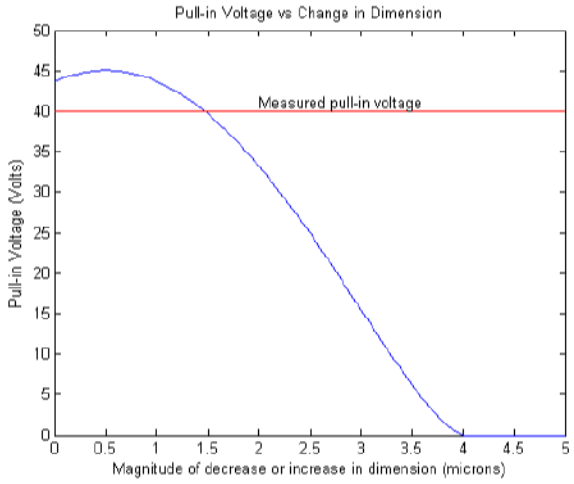

Figure 7. 1: (a) Variation of coefficient with the change in dimension for DRIE_Cant_G3_W5_L500 at wafer location 6, (b) Variation of coefficient with the change in dimension for DRIE_FF_G3_W4_L500 (c) Variation of pull-in voltage with change in dimension for DRIE_PullIn_G3_W4_L200 at wafer location 6

The intersection of the two curves in the figures above, indicate the change in dimension for that device. For instance the change in dimensions is about 1.45 μm for DRIE_Cant_G3_W5_L500 at wafer location 6, about 1.4 μm for DRIE_FF_G3_W4_L500 and about 1.5 μm for DRIE_PullIn_G3_W4_L200 at wafer location 6. These values are computed for each device tested and the results come out to be very consistent. Accordingly the change in dimension for the second run of DRIE of (111) silicon at wafer location 2 is found to be at average1.2 μm, 1.2 μm at wafer location 3, 1.1 μm at wafer location 4, 1.4 μm at wafer location 6, 1.3 μm at wafer location 7, 1.1 μm at wafer location 8 and 1.4 μmat wafer location 9. As a result, assuming that the change in dimensions of the gaps and the widths are the same within the device, the measured dimensions of the devices include considerably high errors. However this is not the case since the cross-section of the devices are not uniform throughout the length. Figure 7.2 shows the fingers of the comb drive of one of the cantilever beam bending tests. It is seen that the fingers are somewhat jagged at one side. This is the case for every member of the devices, which results in non-uniform gage sections and hinders the validity of the coupling equations in deriving the mathematical models. This is certainly a reason of why the test results are so scattered.

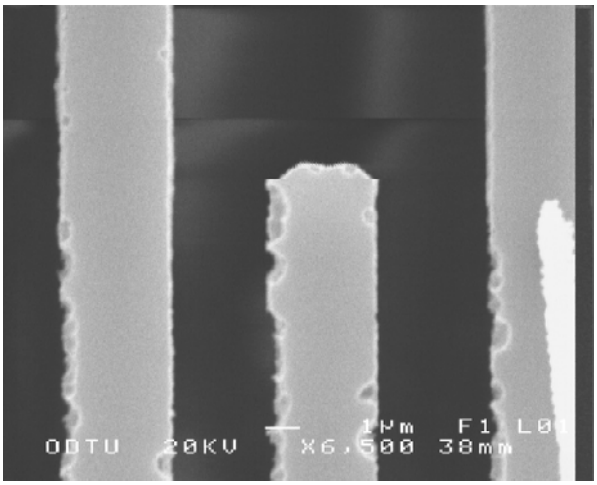

Figure 7. 2: Fingers of the comb drive of cantilever beam bending test device of deep reactive ion etched (111) Si.

Considering the test results obtained from testing of electroplated nickel samples, it is recalled that the results are also dispersed in a wide range. Figure 7.3 shows the SEM picture of the close up view of the moveable electrode on the fatigue test device. It can be seen that the surface roughness is very high. As a result, similar to the case of DRIE samples, electroplated samples also do not satisfy uniform gage sections. This also explains why the results of the tests conducted on nickel samples widely disperse. To conclude, it should be stated that the effects of surface quality should be deeply investigated before further study on the subject.

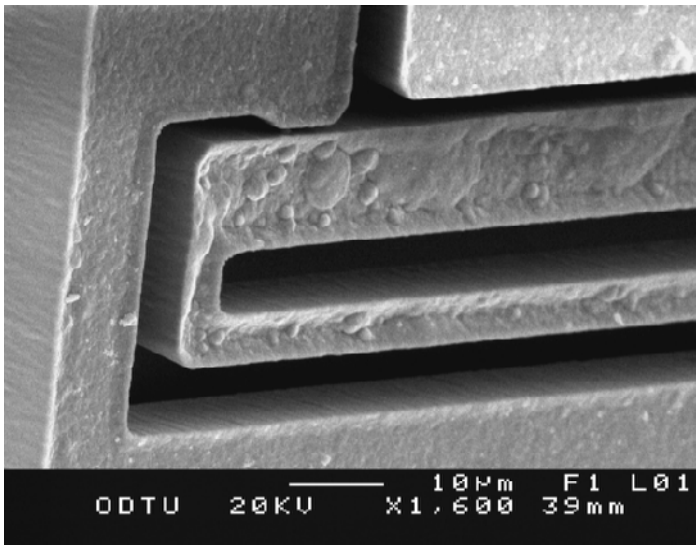

Figure 7. 3: Close up view of the moveable electrode of the fatigue test device of electroplated nickel.

Returning to the graphs in Figure 7.1, they are also measures of sensitivity of the test results to dimensional changes. Comparing the cantilever beam bending and double clamped beam bending, the ratio of displacement to voltage squared, which is the coefficient of the quadratic term, double clamped beam is less sensitive to changes in dimensions. That is, if the test devices are fabricated using a technique with high dimensional accuracy, double clamped beam bending test devices would yield more accurate results. Comparing the three test methods, namely the cantilever beam bending, double clamped beam bending and the cantilever pull-in, the results obtained from cantilever pull-in tests seems to be the

most sensitive to dimensional variations, as the measured pull-in voltage considerably alters with the change in dimension in order of even tenths of microns. As a result, if the dimensional accuracy for the test devices can not be guaranteed, it is nonsense to use pull-in technique to characterize the material. The results of the improved cantilever beam bending test robustly supports this conclusion. While such an analysis could not be done for electroplated nickel samples, since there is not a well defined elastic modulus value for the nickel at micron scale, the general outcomes derived from the analysis of the (111) silicon structures are still valid.

The dimensional sensitivity of the test device is not the only criteria. For instance double clamped beam bending test seems to be the best as the dimensional sensitivity is concerned; however it could be possible to test only 4 samples among deep reactive ion etched (111) silicon devices, since the anchors could not survive. That is the devices should also be designed or modified with respect to the fabrication method involved.

Apart from the dimensional or structural problems related to the test devices, the actuation method, namely the electrostatic actuation, greatly simplifies the tests. The test set-up is provided by a simple circuit described in Section 6.1. No significant problem related to actuation is enrolled through the tests.

Considering the scripts written for the micron level measurements, it can be concluded that the module for measuring the device dimensions failed. While the module provides a foresight about the device dimension, the data is not appropriate to use in the mathematical models since the models require a higher accuracy than that provided by the script. While this is the case for the module for measuring dimensions, the module for measuring the displacements successfully worked. As the module deals with relative positions, the accuracy of the dimensions does not affect the results of the module. This is also supported by the

relatively accurate calibration method involved. Thus cheap and easy to implement method is developed for micron level displacement measurements.

As a final conclusion it should be stated that the prerequisite for a proper mechanical characterization practice in micron level is to provide an optimized fabrication method. Otherwise it can not be possible to derive conclusions from the tests conducted.

REFERENCES

[1] J. A. Palesko, D. H. Bernstein, *Modeling MEMS and NEMS*, Chapman & Hall/CRC, 2002.

[2] N. Maluf, *An Introduction to Microelectromechanical Systems Engineering*, Artech House, 2000.

[3] S. Santra, P. Holloway, and C. D. Batich, "Fabrication and Testing of a Magnetically Actuated Micropump," Sensors and Actuators B 87, pp. 358–364, 2002.

[4] S. D. Senturia, *Microsystem Design*, Kluwer Academic Publishers, 2001.

[5] W. N. Sharpe, "Mechanical Properties of Materials," The MEMS Handbook, CRC Press, 2002.

[6] D. Halliday, R. Resnick, and J. Walker, *Fundamentals of Physics, Extended*, John Wiley & Sons, 1997

[7] S. H. Lee, J. W. Evans, Y. E. Pak, J. U. Jeon, and D. Kwon, "Evaluation of Elastic Modulus and Yield Strength of Al Film Using an Electrostatically Actuated Test Device," Thin Solid Films, Vol. 408, pp. 223-229, 2002.

[8] M. A. Haque, M. T. A. Saif, "Mechanical Behavior of 30-50 nm Thick Aluminum Films Under Uniaxial Tension," Scripta Materialia, 47, pp. 863-867, 2002.

[9] H. D. Espinosa, B. C. Prorok, and M. Fischer, "A Methodology for Determining Mechanical Properties of Freestanding Thin Films and MEMS Materials," Journal of the Mechanics and Physics of Solid, Vol. 51, pp. 47-67, 2003.

[10] L. L. Chu, L. Que, and Y. B. Gianchandani, "Measurement of Material Properties Using Differential Capacitive Strain Sensors," Journal of Microelectromechanical Systems, Vol. 11, No. 5, pp. 489-498, October 2002.

[11] K. P. Larsen, A. A. Rasmussen, J. T. Ravnkilde, M. Ginnerup, and Ole Hansen, "MEMS Device for Bending Test: Measurement of Fatigue and Creep of Electroplated Nickel," Sensors and Actuators A, 103, pp. 156-164, 2003.

[12] C. S. Pan, and W. Hsu, "A Microstructure for in situ Determination of Residual Strain, " Journal of Microelectromechanical Systems, Vol. 8, No: 2, pp. 200-207, June 1999.

[13] L. Que, *Micromachined Sensors and Actuators Based on Bent-Beam Suspensions*, Ph. D. dissertation, University of Wisconsin-Madison, 2000.

[14] L. Spiegel, P.E., G. F. Limbrunner, P.E., *Applied Statics and Strength of Materials, Second Edition*, Macmillan Publishing Company, 1994.

[15] R. Legtenberg, A. W. Groeneveld, and M. Elwenspoek, "Comb-drive Actuators for Large Displacements," Vol. 6, pp. 320-329, September 1996.

[16] F. P. Beer, E. R. Johnston, Jr., *Mechanics of Materials, Second Edition in SI units*, McGraw Hill, 1992.

[17] ANSYS 7.0 Documentation, Coupled Field Analysis Guide

[18] Y. B. Gianchandani, K. Najafi, "Bent-beam Strain Sensors," Journal of Microelectromechanical Systems, Vol. 5, No. 1, pp.52-58, March 1996.

[19] K. P. Larsen, J. T. Ravnkilde, M. Ginnerup, and O. Hansen, "Devices for Fatigue Testing of Electroplated Nickel (MEMS)," Proceedings of MEMS 2002, pp. 443-446, January 2002.

[20] J. E. Shigley, C. R. Mischke, *Mechanical Engineering Design*, McGraw Hill, 1989.

[21] J. Kim, D. Cho, and R. S. Muller, "Why is (111) Silicon a Better Mechanical Material For MEMS?," in Proc. International Conference on Solid-State Sensors and Actuators, 2001.

[22] D. Schneider, M. D. Tucker, “Non-destructive characterization and evaluation of thin films by laser-induced ultrasonic surface waves,” Thin Solid Films, Vol 290-291, pp 305-311, December 1996.

[23] N. Otsu, "A Threshold Selection Method from Gray-Level Histograms," IEEE Transactions on Systems, Man, and Cybernetics, Vol. 9, No. 1, pp. 62-66, 1979.

[24] A. Kingston, I. Svalbe, “Adaptive Discrete Radon Transforms for Grayscale Images,” Electronic Notes in Discrete Mathematics Volume 12, p. 12, March 2003.

[25] H. Kahn, R. Ballarini, and A. H. Heuer, “Dynamic Fatigue of Silicon,” Current Opinion in Solid State & Materials Science, Volume 8, pp 71-76, 2004.

[26] M. Legros, A. Jacques, and A. George, “Fatigue Testing of Single Crystalline Silicon,” Materials Science and Engineering A, 309-310, pp 233-236, 2001.

[27] A. K. Jamting, J. M. Bell, M. V. Swain, and N. Schwarzer, “Investigation of the Elastic Modulus of Thin Films Using Simple Biaxial Bending Techniques,” Thin Solid Films, 308-309, pp. 304-309, 1997.

[28] W. G. Knauss, I. Chasiotis, and Y. Huang, ”Mechanical Measurements an Micron and Nanometer Scales,” Mechanics of Materials, 35, pp. 217-231, 2003.

[29] T. Tsuchiya, O. Tabata, J. Sakata, and Y. Taga, "Specimen size Effect on Tensile Strength of Surface-Micromachined Polycrystalline Silicon Thin Films," Journal of Microelectromechsnical Systems, Vol. 7, No. 1, pp. 106-113, March 1998.

[30] Z. Xue, M. Taher A. Saif, and Y. Huang, "The Strain Gradient Effect in Microelectromechanical Systems (MEMS)," Journal of Microelectromechanical Systems, Vol. 11, No. 1, pp. 27-35, February 2002.

[31] S. Chen, T. V. Baughn, Z. J. Yao, and C. L. Goldsmith, "A New in situ Residual Stress Measurement Method for a MEMS Thin Fixed-Fixed Beam Structure," Journal of Microelectromechanical Systems, Vol. 11, No. 4, pp. 309-416, August 2002.

[32] K. J. Hemker, H. Last, "Microsample Tensile Testing of LIGA Nickel for MEMS Applications," Materials Science and Engineering A 319-321, pp. 882-886, 2001.

[33] E. S. Kolesar, S. Y. Ko, J. T. Howard, P. B. Allen, J. M. Wilken, N. C. Boydston, M. D. Ruff, and R. J. Wilks, "In-plane Tip Deflection and Force Achieved with Asymetrical Polysilicon Electrothermal Microactuators," Thin Solid Films, 377-378, pp. 719-726, 2000.

[34] X. Li, B. Bhushan, "Fatigue Studies of Nanoscale Structures for MEMS/NEMS Applications Using Nanoindentation Techniques," Surface and Coatings Technology, 163-164, pp. 521-526, 2003.

[35] V. T. Stikar, S. M. Spearing, "Materials Selection for Microfabricated Electrostatic Actuators," Sensors and Actuators A 102, pp. 279-285, 2003.

[36] H. S. Cho, K. J. Hemker, K. Lian, J. Goettert, and G. Dirras, "Measured Mechanical Properties of LIGA Ni Structures," Sensors and Actuators A 103, pp. 59-63, 2003.

[37] X. Y. Ye, Z. Y. Zhou, Y. Yang, J. H. Zhang, and J. Yao, "Determination of the mechanical properties of microstructures," Sensors and Actuators A: Physical, Vol. 54, pp. 750-754, June 1996.

[38] L. Alting, F. Kimura, H. N. Hansen, and G. Bissaco, "Micro Engineering," Annals of the CIRP, Vol. 52, 2003.

[39] P. M. Osterberg, S. D. Senturia, "M-Test: A Test Chip for MEMS Material Property Measurement Using Electrostatically Actuated Test Structures," Journal of Microelectromechanical Systems, Vol. 6, No: 2, pp. 107-118, June 1997.

[40] M. A. Haque, M. T. A. Saif, "Microscale Materials Testing Using MEMS Actuators," Journal of Microelectromechanical Systems, Vol. 10, No: 1, pp. 146-152, March 2001.

[41] F. Ericson, S. Greek, J. Söderkvist, and J. Schweitz, "High-sensitivity Surface Micromachined Structures for Internal Stress and Stress Gradient Evaluation," Journal of Micromechanics and Microengineering, Vol. 7, pp. 30-36, 1997.

[42] W. Huang, G. Lu, "Analysis of Lateral Instability of In-plane Comb Drive MEMS Actuators Based on a Two-dimensional Model," Sensors and Actuators A: Physical, Vol. 113, pp. 78-85, 2004.

[43] M. J. Kobrinsky, E. R. Deutsch, and S. D. Senturia, "Effect of Support Compliance and Residual Stress on the Shape of doubly Supported Surface

Micromachined Beams," Journal of Microelectromechanical Systems, Vol. 9, No: 3, pp. 361-369, September 2000.

[44] B. D. Jensen, M. P. de Boer, N. D. Masters, F. Bitsie, and D. A. LaVan, "Interferometry of Actuated Microcantilevers to Determine Material Properties and Test Structure Nonidealities in MEMS," Jpurnal of Microelectromechanical Systems, Vol. 10, No:3, pp. 336-346, September 2001.

[45] W. A. Johnson, L. K. Warne, "Electrophysics of Micromechanical Comb Actuators," Journal of Microelectromechanical Systems, Vol. 4, No: 1, pp. 49-59, March 1995.

[46] T. Hirano, T. Furuhata, K. K. Gabriel, and H. Fujita, "Design, Fabrication, and Operation of Submicron Gap Comb-Drive Microactuators," Journal of Microelectromechanical Systems, Vol. 1, No: 1, pp. 52-59, March 1992.

APPENDIX A

EVALUATION TABLE OF SOME EXISTING MEMS TESTING METHODS

Considerations are equally weighted (3 credits for each criterion).

Table A. 1: Evaluation table of some existing MEMS testing methods

		Structure	Measurement	Actuation	total
static	**Differential Capacitive Sensing**	3	3	3	9
	Cantilever LIGA Ni Microposts	1	1	2	4
	Electrostatically Actuated Cantilever Beam Bending	1	2	3	6
	Electrostatically Actuated Double Clamped Beam Bending	3	2	3	8
	Membrane Deflection Experiment (MDE)	3	3	2	8
	Uniaxial tension	3	2	3	8
	Tensile testing	1	2	2	5
dynamic	**Fatigue (one sided)**	1	3	2	6
	Fatigue (double sided)	1	3	3	7
passive	**Residual Stress and Stress Gradient Evaluation**	1	2	-	3
	Determination of Residual Strain	1	2	-	3
	Bent Beam for Residual Stress Evaluation	3	2	-	5

APPENDIX B

STIFFNESS CALCULATIONS

1. Stiffness Calculation for Cantilever Pull-in Structures

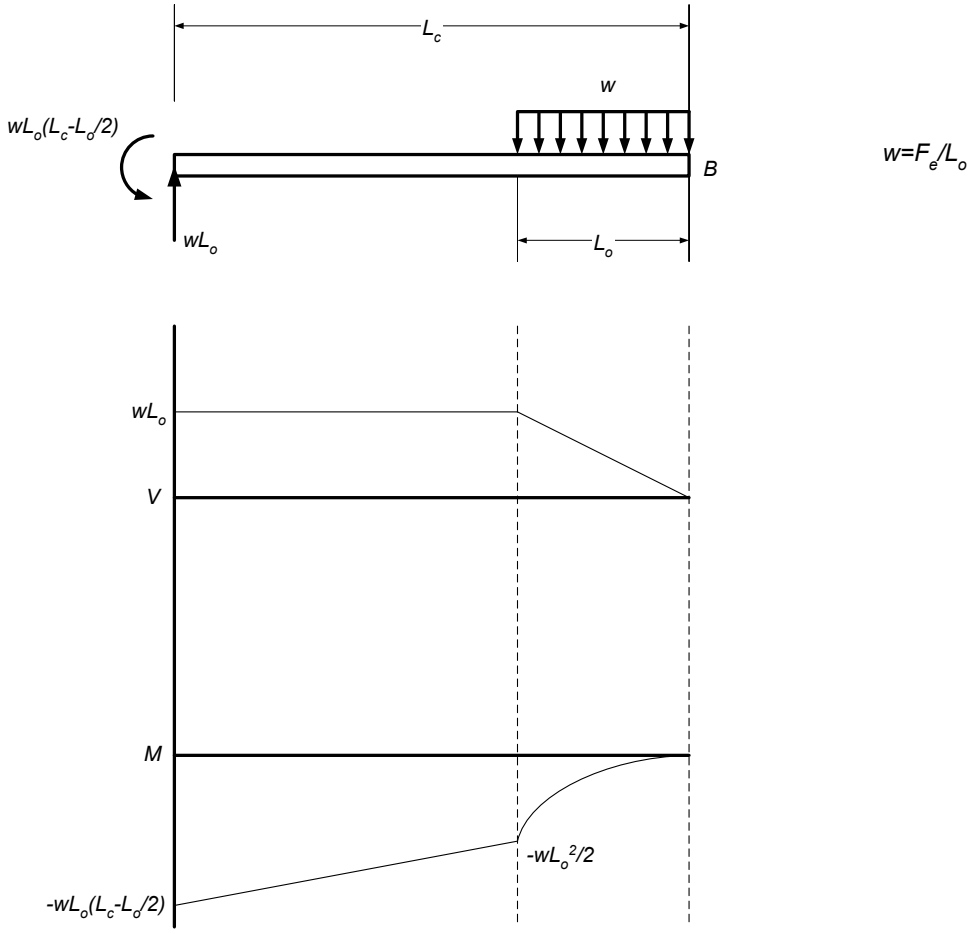

Figure B. 1: Free body diagram and shear force and bending moment diagrams of the beam

According to FigureB.1;

F_e : electrostatic force created

L_o : overlap distance

L_c : Length of cantilever beam

Method of area of moments [16] is used for determining the deflection at point *B* of the cantilever. According to the method of area of moments

$$EI\delta_B = wL_o\left(\frac{L_c - L_o}{2}\right)^2\left(\frac{L_c - L_o}{3}\right) + \frac{wL_o^{\,2}}{2}\left(L_c - L_o\right)\left(\frac{L_c - L_o}{2}\right) + \frac{wL_o^{\,3}}{6}\left(L_c - L_o + \frac{L_o}{4}\right)$$

$$= wL_o\frac{\left(L_c - L_o\right)^3}{6} + wL_o^{\,2}\frac{\left(L_c - L_o\right)^2}{4} + wL_o^{\,3}\frac{\left(4L_c - 3L_o\right)}{24}$$

where *E* is the elastic modulus and *I* is the second area moment of inertia of the cross-section of the beam about the bending axis.

Since

$$F_e = wL_o \quad \text{and} \quad k_B = \frac{F_e}{\delta_B}$$

Therefore the spring constant at point *B* is found to be

$$k_B = \frac{EI}{\frac{\left(L_c - L_o\right)^3}{6} + \frac{L_o\left(L_c - L_o\right)^2}{4} + \frac{L_o^{\,3}\left(4L_c - 3L_o\right)}{24}}$$

2. Stiffness Calculation for Suspension Springs in Cantilever Bending and Double Clamped Beam Bending Test Devices

One of the side suspension springs and lateral comb drive are shown on Figure B.2 below. Note that the spring is anchored at one end, and pulled through the comb drive at the other end.

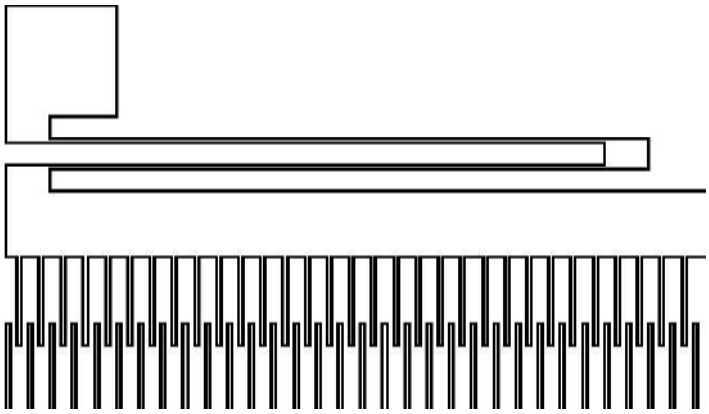

Figure B. 2: One of the side suspension springs and part of the lateral comb drive

Assuming the connections of the suspension as rigid, that is (1), (3) and (5) are rigid, the deflection curve of the spring will be as shown below. Note that (1) is anchored and (5) is pulled through the comb drive.

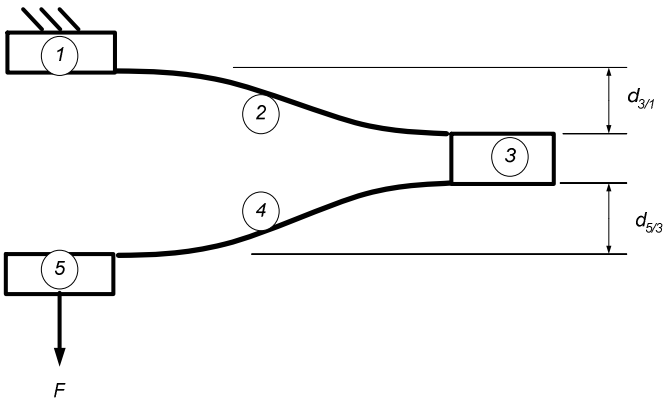

Figure B. 3: Suspension model of the spring

Using the displacement formula for the one end fixed, one end guided beam [16]

$$d_{5/3} = d_{3/1} = \frac{Fl_s^{\,3}}{12EI}$$

where l_s is the length of the suspension beam, E is the elastic modulus and I is the second area moment of inertia of the beam cross-section about the bending axis.

Total deflection is then

$$\delta = d_{3/1} + d_{5/3} = \frac{Fl_s^{\ 3}}{6EI}$$

Since

$$k_s = \frac{F}{\delta} \text{ and } I = \frac{1}{12} t w_s^{\ 3}$$

for the beam with thickness of w_s and thickness t, then the stiffness for the suspension spring is

$$k_s = \frac{Etw_s^3}{2l_s^3}$$

APPENDIX C

FEA SCRIPTS

1. Sample ANSYS 7.0 Batch for Electromechanical Coupling

```
/clear,start
/aux15
ioptn,iges,nodefeat
ioptn,merge,yes
ioptn,solid,yes
ioptn,small,yes
ioptn,gtoler,defa
igesin,'cantilever','igs'          ! import the model in iges
/PREP7                  ! open the preprocessor of ANSYS
vltg=30                 ! applied voltage is set
et,1,121,,,,,,,1        ! PLANE121 electrostatic element with quadratic shape function for air
et,2,121                ! temporaray element for beam region
emunit,epzro,8.854e-6          ! Free-space permittivity, µMKSV units
mp,perx,2,1             ! Relative permittivity for air
asel,s,area,,6          ! select area for beam
aatt,1,,1
asel,s,area,,2          ! select area for air elements
cm,air,area             ! group air area into component
```

```
aatt,2,,2
asel,s,area,,7          ! select area for finger gap elements, air mesh is refined at
!finger gap
cm,gap,area             ! group gap area into component
aatt,2,,2
allsel,all
mshape,0
esize,1         ! element size is set, finer elements are used for meshing the gap
amesh,2         ! mesh finger gap with quadirlaterals
esize,5
amesh,1         ! mesh beam
mshape,0
esize,10
amesh,5                 ! mesh air with quadirlaterals
asel,s,area,,1
lsla,s
dl,all,,volt,vltg       ! apply voltage to beam
asel,s,area,,3
lsla,s
dl,all,,volt,0          ! ground the fixed electrode (not meshed)
allsel,all
et,1,0                  ! set structure to null element type
physics,write,ELECTROS  ! write electrostatic physics file
physics,clear           ! clear physics
et,1,82,,,              ! PLANE82, structural element with quadratic shape
!function for beam
et,2,0                  ! set air to null element type
mp,ex,1,160e3           ! set elastic modulus for the structural material, μN/(μm)2
mp,nuxy,1,0.3                   ! set Poisson's ratio for the structural material
dl,345,,ux,0            ! anchor the structure
dl,345,,uy,0
```

```
dl,344,,ux,0
dl,344,,uy,0
dl,343,,ux,0
dl,343,,uy,0
dl,353,,ux,0
dl,353,,uy,0
dl,352,,ux,0
dl,352,,uy,0
dl,3,,ux,0
dl,3,,uy,0
dl,2,,ux,0
dl,2,,uy,0
allsel,all
finish
physics,write,STRUCTURE
ESSOLV,'ELECTROS','STRUCTURE',2,0,'gap',,5e-3,5e-3,50
! set convergence criteria
finish
physics,read,STRUCTURE
```

APPENDIX D

MATLAB SCRIPTS FOR DEVICE DIMENSIONING

The scripts are composed of three independent modules, first one “CALIBRATE” is for calibration of the images, second one “MEMSDIST” is for dimensioning of the structures and the third one “MEMSDISP” is for measuring the displacements of moving members. It should be noted that the routine CALIBRATE should be run before MEMSDIST or MEMSDISP. Scripts also involve a function “hintersect”. This function is used to compute the intersection points of the detected lines and the horizontal axis of the images. The function “hintersect” is also given at the end.

```
% ------------------------------------------------------
% CALIBRATE
% ------------------------------------------------------
global pixelwidth
filename=input('Enter the filename of the image to be calibrated:  ','s');
width=input('Enter the width of the image in pixels:  ');
height=input('Enter the height of the image in pixels:  ');
finger=input('Enter the scale distance in microns:  ');
im=imread(filename,'BMP');
calib=rgb2gray(im); %color image is converted to grayscale image
calib=imadjust(calib);
levelcalib=graythresh(calib);
```

```
calib=im2bw(calib,levelcalib); % grayscale image is converted to binary image
Image1=bwmorph(calib,'skel',Inf); % skeleton of the pattern is determined
roi1=roipoly(Image1);
roi2=roipoly(Image1);
% regions enclosing the medial axes of the adjacent fingers are selected
Im1=imadd(roi1,Image1); Im2=imadd(roi2,Image1);
for j=1:width
   for i=1:height
      if Im1(i,j)==2
        Im1(i,j)=1;
      else
        Im1(i,j)=0;
      end
      if Im2(i,j)==2
        Im2(i,j)=1;
      else
        Im2(i,j)=0;
      end
   end
end     % image is filtered using the regions selected
theta = 0:179; %line detection for the first region of interest
[R1,xp1] = radon(Im1,theta);
s1=size(xp1); %search for the position of the max of the transform matrix
max1=0;
for j=1:180
   for i=1:s1(1)
      if R1(i,j)>max1
         max1=R1(i,j);
         pos1=xp1(i);
         angle1=j-1;
      end
```

```
    end
end
%line detection for the second region of interest
%note that a parallel line is searched
theta = angle1;
[R2,xp2] = radon(Im2,theta);
%search for the position of the max of the transform vector
s2=size(xp2);
max2=0;
for i=1:s2(1)
    if R2(i,1)>max2
        max2=R2(i,1);
        pos2=xp2(i);
    end
end
pixalong=7/abs(pos2-pos1); %pixel width along the direction normal to "angle1"
pixelwidth=pixalong*cos(pi*angle1/180); %actual pixel width
fig=imshow(im);
y=[0 height];
[x1]=hintersect(pos1,angle1,width,height);
[x2]=hintersect(pos2,angle1,width,height);
hold on
plot(x1,y,'r-','LineWidth',2);
plot(x2,y,'r-','LineWidth',2);
imview close all
pause(2);
close all

% ------------------------------------------------------------
% routine CALIBRATION complete
% ------------------------------------------------------------
```

```
% ------------------------------------------------------------
% MEMSDIST
% ------------------------------------------------------------

global pixelwidth
iptsetpref('TruesizeWarning','off');

filename=input('Enter the filename of the image to be measured:  ','s');
width=input('Enter the width of the image in pixels:  ');
height=input('Enter the height of the image in pixels:  ');
        %prompt user to input the filename, width and height


Imbeam=imread(filename,'BMP');
Imbeam=rgb2gray(Imbeam); %convert the rgb image to grayscale image

Imbeam=imadjust(Imbeam);

%threshold determined in order to create the binary image
levelbeam=graythresh(Imbeam);

binbeam=im2bw(Imbeam,levelbeam);

edgebeam=edge(binbeam); %edge detection

roi1=roipoly(edgebeam);
roi2=roipoly(edgebeam);

Im1=imadd(roi1,edgebeam);
Im2=imadd(roi2,edgebeam);
```

```
for j=1:width
   for i=1:height
      if Im1(i,j)==2
        Im1(i,j)=1;
      else
        Im1(i,j)=0;
      end
      if Im2(i,j)==2
        Im2(i,j)=1;
      else
        Im2(i,j)=0;
      end
   end
end
%line detection for the first region of interest
theta = 0:179;
[R1,xp1] = radon(Im1,theta);
%search for the position of the max of the transform matrix
s1=size(xp1);
max1=0;
for j=1:180
   for i=1:s1(1)
      if R1(i,j)>max1
         max1=R1(i,j);
         pos1=xp1(i);
         angle1=j-1;
      end
   end
end
%line detection for the second region of interest
%note that a parallel line is searched
```

```
theta = angle1;
[R2,xp2] = radon(Im2,theta);
%search for the position of the max of the transform vector
s2=size(xp2);
max2=0;
for i=1:s2(1)
   if R2(i,1)>max2
      max2=R2(i,1);
      pos2=xp2(i);
   end
end
pixcorr=(pixelwidth)/(abs(cos(angle1*pi/180)));
         %correct pixel width along the direction normal to "angle1"
fig=imshow(edgebeam);
y=[0 height];
[x1]=hintersect(pos1,angle1,width,height);
[x2]=hintersect(pos2,angle1,width,height);
hold on
plot(x1,y,'g-','LineWidth',2);
plot(x2,y,'g-','LineWidth',2);
pixdist=abs(pos1-pos2);
distance=pixdist*pixcorr
imview close all
pause(2);
close all

% ------------------------------------------------------------
% routine MEMSDIST complete
% ------------------------------------------------------------
```

```
% ------------------------------------------------------------
% MEMSDISP
% ------------------------------------------------------------
global pixelwidth

iptsetpref('TruesizeWarning','off');
nooffigure=input('Enter the number of figures:  ');
width=input('Enter the width of the image in pixels:  ');
height=input('Enter the height of the image in pixels:  ');
        %prompt user to input the number of successive figures, width and height
Im=imread('1.bmp','BMP'); %read first image to detect reference line
Im=rgb2gray(Im); %convert the rgb image to grayscale image
Im=imadjust(Im);
level=graythresh(Im); %threshold determined in order to create the binary image
bin=im2bw(Im,level);
Imedge=edge(bin); %edge detection
imshow(Imedge);
xlabel('Select the region enclosing the reference line.')
roi1=roipoly;
Im1=imadd(roi1,Imedge);

for j=1:width
   for i=1:height
      if Im1(i,j)==2
        Im1(i,j)=1;
      else
        Im1(i,j)=0;
      end
   end
end
%line detection for the reference image
```

```
theta = 0:179;
[R,xp] = radon(Im1,theta);

%search for the position of the max of the radon matrix
s=size(xp);
max=0;
for j=1:180
   for i=1:s(1)
      if R(i,j)>max
         max=R(i,j);
         po=xp(i);
         ang=j-1;
      end
   end
end

y=[0 height];
[x1]=hintersect(po,ang,width,height);
pixcorr=(pixelwidth)/(abs(cos(ang*pi/180))); %correct pixel width along the
direction normal to "ang"

for k=1:nooffigure %process all snapshots captured at each voltage level
   clear Im level bin Imedge;
   filename=[num2str(k),'.bmp'];
   Im=imread(filename,'BMP');
   Im=rgb2gray(Im); %convert the rgb image to grayscale image
   Im=imadjust(Im);
   level=graythresh(Im);
        %threshold determined in order to create the binary images
   bin=im2bw(Im,level);
   Imedge=edge(bin); %edge detection
```

```
figure
 fig=imshow(Imedge);
 xlabel('Select the region enclosing the displaced line.')
 roi=roipoly(Imedge);
 Im1=imadd(roi,Imedge);
 for j=1:width
    for i=1:height
       if Im1(i,j)==2
          Im1(i,j)=1;
       else
          Im1(i,j)=0;
       end
    end
 end
 % line detection (note that the line is searched along the reference direction)
 theta = ang;
 [R1,xp1] = radon(Im1,theta);
 s1=size(xp1);
 max(k)=0;
 for i=1:s1(1)
    if R1(i,1)>max(k)
       max(k)=R1(i,1);
       pos(k)=xp1(i);
    end
 end

 hold on;
 [x2]=hintersect(pos(k),ang,width,height);
 plot(x1,y,'c-','LineWidth',2);
 plot(x2,y,'c-','LineWidth',2);
 distance(k)=abs(po-pos(k));
```

```
   pause(1);
   close all;
end

microndisp=pixelwidth*distance;
% ---------------------------------------------------------------
% routine MEMSDISP complete
% ---------------------------------------------------------------

% ---------------------------------------------------------------
% hintersect
%---------------------------------------------------------------
function [x]=hintersect(pos,angle,width,height);
p=abs(pos);
sina=abs(sin(angle*pi/180));
cosa=abs(cos(angle*pi/180));

if angle~0
   if angle<90 & pos>0
      a=(sina/cosa)*(p/sina-height/2)+width/2;
      b=(sina/cosa)*(p/sina+height/2)+width/2;
   end
   if angle<90 & pos<0
      a=-(sina/cosa)*(p/sina+height/2)+width/2;
      b=-(sina/cosa)*(p/sina-height/2)+width/2;
   end
   if angle>90 & pos>0
      a=-(sina/cosa)*(p/sina-height/2)+width/2;
      b=-(sina/cosa)*(p/sina+height/2)+width/2;
   end
```

```
    if angle>90 & pos<0
       a=(sina/cosa)*(p/sina+height/2)+width/2;
       b=(sina/cosa)*(p/sina-height/2)+width/2;
   end
else
   a=width/2+pos;
   b=a;
end
x=[a b];

% ------------------------------------------------------------
% function hintersect complete
%------------------------------------------------------------
```

APPENDIX E

CHIP LAYOUTS OF THE TEST DEVICES

1. Chip Layout of (111) Oriented DRIE Si Devices

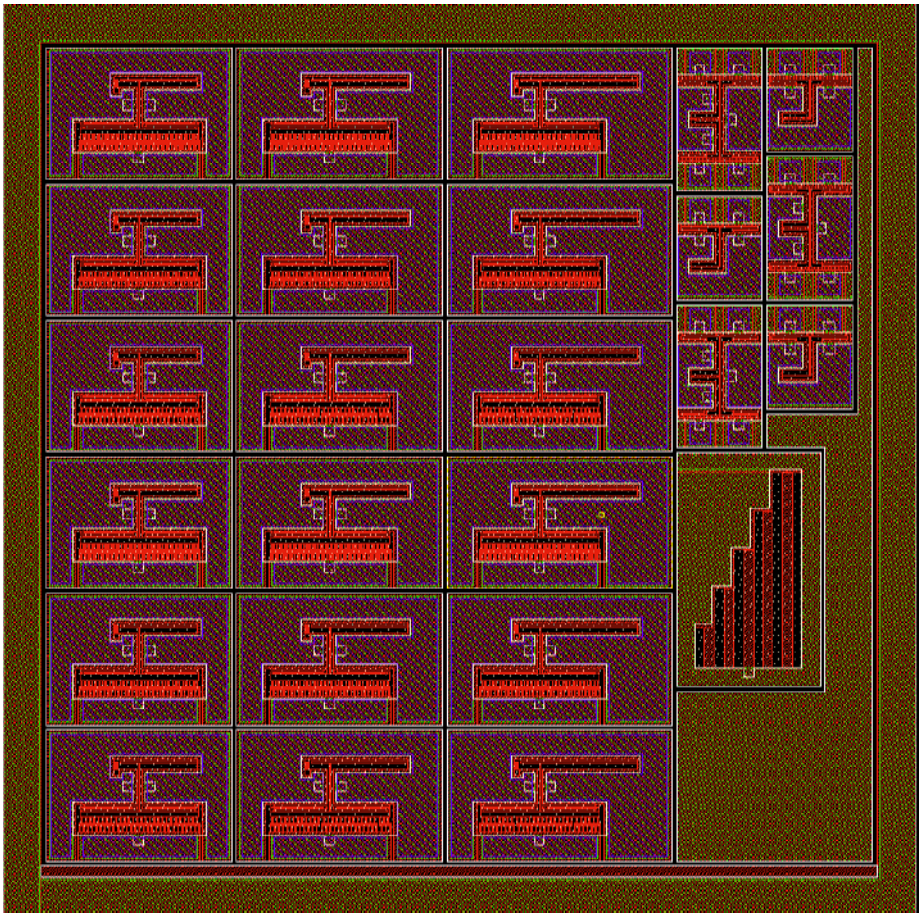

Figure E. 1: Mechanical characterization chip of (111) oriented DRIE Si, containing cantilever beam bending test devices, fatigue test devices and cantilevers for residual stress gradient measurement

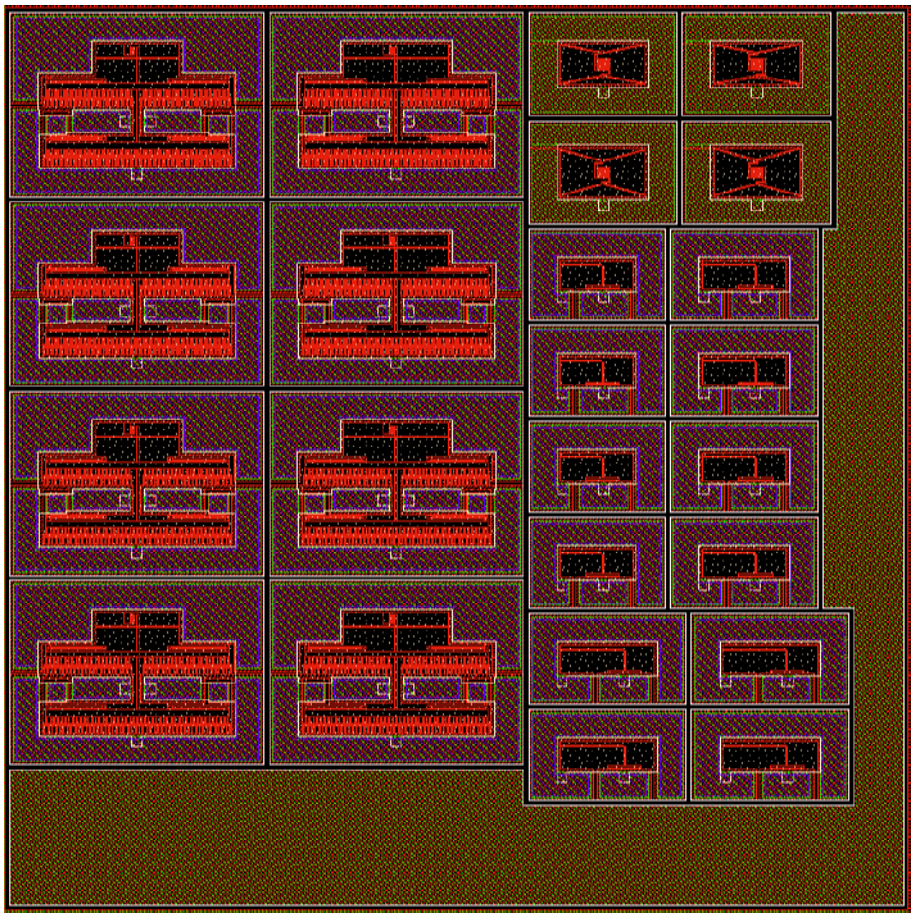

Figure E. 2: Mechanical characterization chip of (111) oriented DRIE Si, containing double clamped beam bending test devices, pull-in test devices and bent beam residual strain sensors

2. Chip Layout of Electroplated Nickel Devices

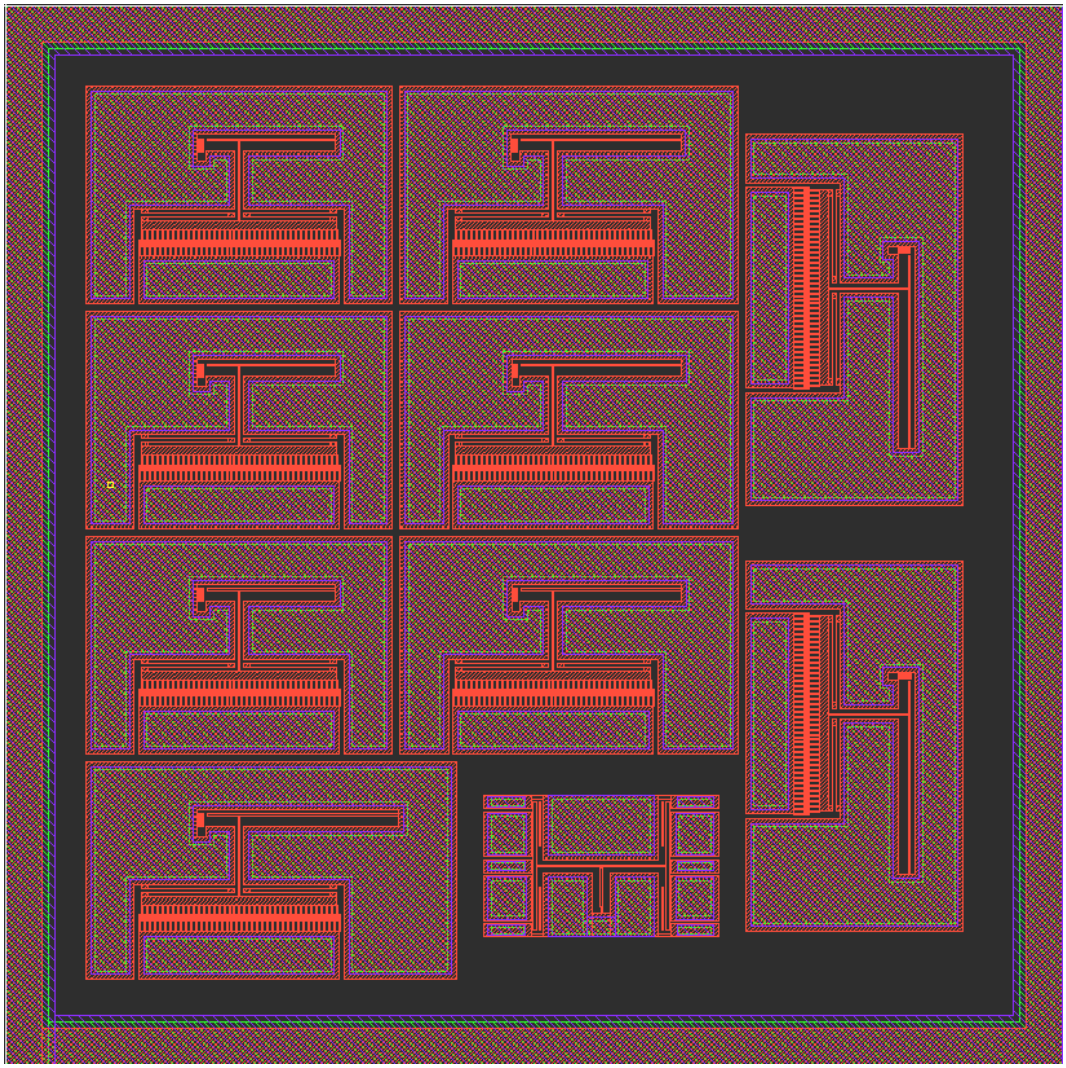

Figure E. 3: Mechanical characterization chip of electroplated nickel, containing cantilever beam bending test devices and a fatigue test device

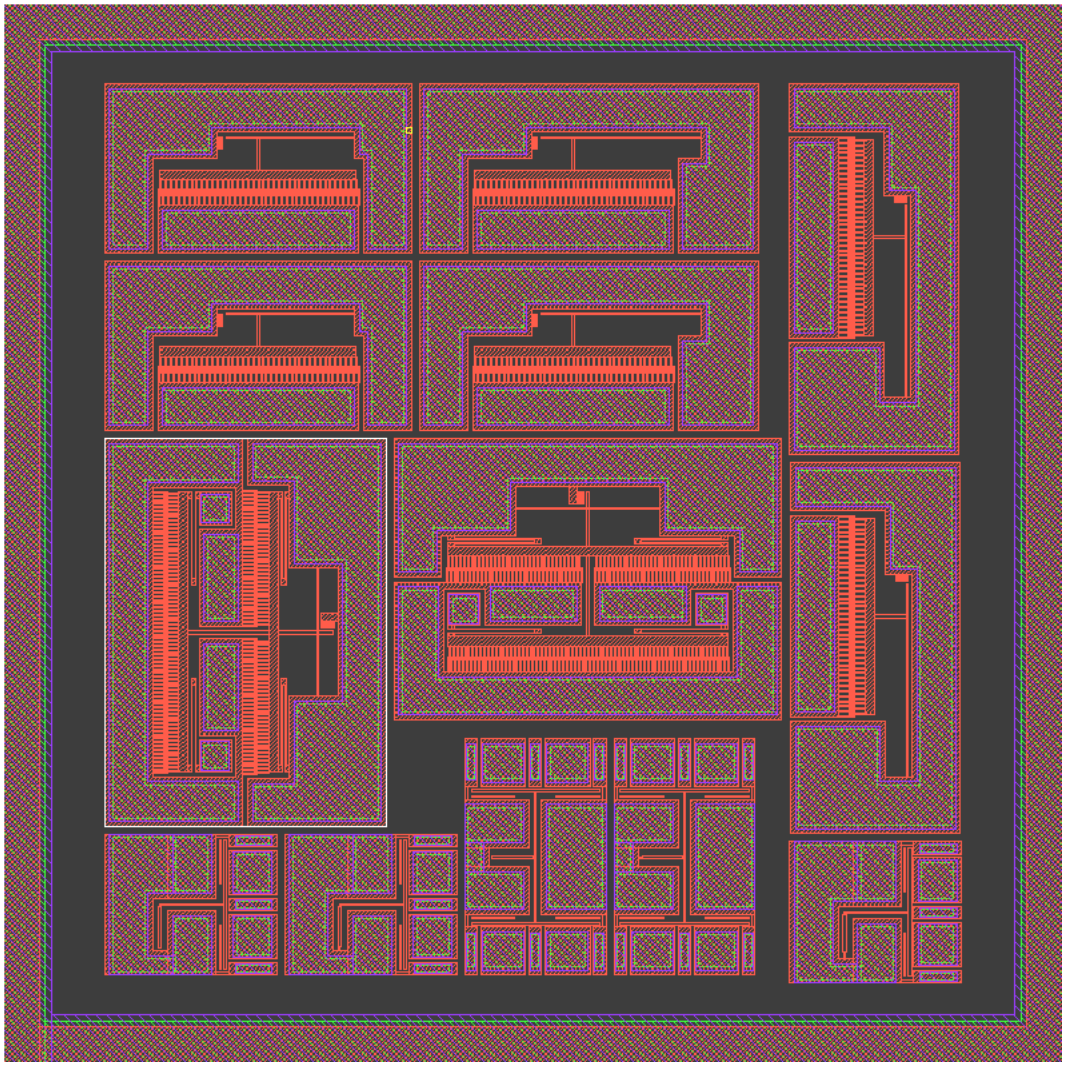

Figure E. 4: Mechanical characterization chip of electroplated Ni, containing double clamped beam bending test devices and fatigue test devices

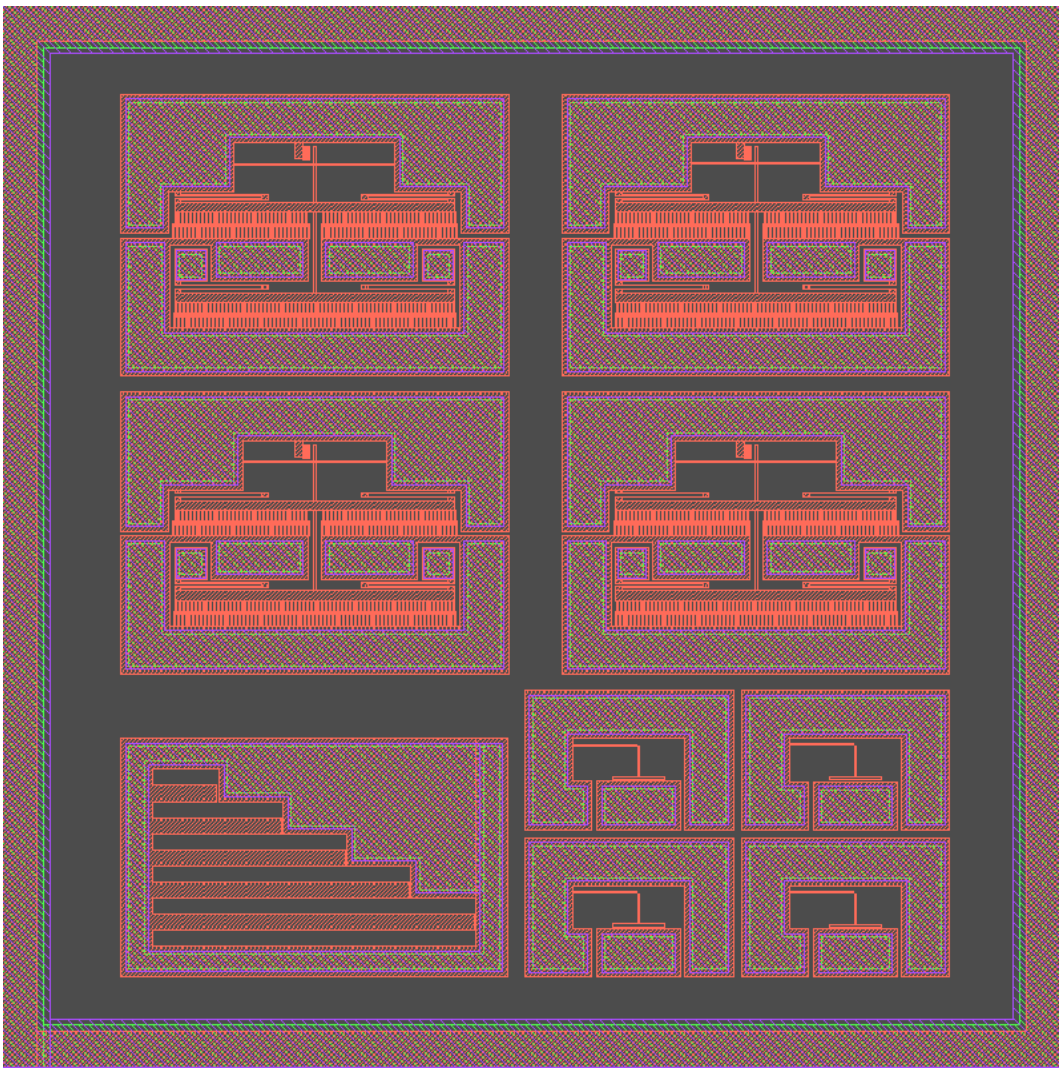

Figure E. 5: Mechanical characterization chip of electroplated Ni, containing double clamped beam bending test devices, pull-in test devices and cantilevers for residual stress gradient measurement